machines

MDPI

Article

BLUE SABINO: Development of a BiLateral Upper-Limb Exoskeleton for Simultaneous Assessment of Biomechanical and Neuromuscular Output

Christopher K. Bitikofer [1], Sebastian Rueda Parra [1,2], Rene Maura [1], Eric T. Wolbrecht [1] and Joel C. Perry [1,*]

[1] Mechanical Engineering Department, University of Idaho, 875 Perimeter Dr., Moscow, ID 83844, USA; bitikofer@uidaho.edu (C.K.B.); rued7682@vandals.uidaho.edu (S.R.P.); maur9504@vandals.uidaho.edu (R.M.); ewolbrec@uidaho.edu (E.T.W.)

[2] National Center for Adaptive Neurotechnologies (NCAN), Stratton VA Medical Center, 113 Holland Ave., Albany, NY 12208, USA; sebastian@neurotechcenter.org

* Correspondence: jperry@uidaho.edu; Tel.: +1-208-885-2144

Abstract: Arm and hand function play a critical role in the successful completion of everyday tasks. Lost function due to neurological impairment impacts millions of lives worldwide. Despite improvements in the ability to assess and rehabilitate arm deficits, knowledge about underlying sources of impairment and related sequela remains limited. The comprehensive assessment of function requires the measurement of both biomechanics and neuromuscular contributors to performance during the completion of tasks that often use multiple joints and span three-dimensional workspaces. To our knowledge, the complexity of movement and diversity of measures required are beyond the capabilities of existing assessment systems. To bridge current gaps in assessment capability, a new exoskeleton instrument is developed with comprehensive bilateral assessment in mind. The development of the BiLateral Upper-limb Exoskeleton for Simultaneous Assessment of Biomechanical and Neuromuscular Output (BLUE SABINO) expands on prior iterations toward full-arm assessment during reach-and-grasp tasks through the development of a dual-arm and dual-hand system, with 9 active degrees of freedom per arm and 12 degrees of freedom (six active, six passive) per hand. Joints are powered by electric motors driven by a real-time control system with input from force and force/torque sensors located at all attachment points between the user and exoskeleton. Biosignals from electromyography and electroencephalography can be simultaneously measured to provide insight into neurological performance during unimanual or bimanual tasks involving arm reach and grasp. Design trade-offs achieve near-human performance in exoskeleton speed and strength, with positional measurement at the wrist having an error of less than 2 mm and supporting a range of motion approximately equivalent to the 50th-percentile human. The system adjustability in seat height, shoulder width, arm length, and orthosis width accommodate subjects from approximately the 5th-percentile female to the 95th-percentile male. Integration between precision actuation, human–robot-interaction force-torque sensing, and biosignal acquisition systems successfully provide the simultaneous measurement of human movement and neurological function. The bilateral design enables use with left- or right-side impairments as well as intra-subject performance comparisons. With the resulting instrument, the authors plan to investigate underlying neural and physiological correlates of arm function, impairment, learning, and recovery.

Keywords: arm exoskeleton; bilateral; functional assessment; neurological impairment; rehabilitation; human–robot attachment

Citation: Bitikofer, C.K.; Rueda Parra, S.; Maura, R.; Wolbrecht, E.T.; Perry, J.C. BLUE SABINO: Development of a BiLateral Upper-Limb Exoskeleton for Simultaneous Assessment of Biomechanical and Neuromuscular Output. *Machines* **2024**, *12*, 617. https://doi.org/10.3390/machines12090617

Academic Editor: Alejandro Ramirez

Received: 21 June 2024
Revised: 12 August 2024
Accepted: 19 August 2024
Published: 3 September 2024

1. Introduction

The human arm is one of the most complex manipulators in existence, and its level of function vs. impairment has not been fully quantified using modern measurement instruments. The dexterity of the hand and its opposable thumb, combined with the large

workspace of the shoulder, make the arm an extremely versatile and efficient tool for interaction with a diversity of objects and environmental conditions. The world around us has largely been created for interactions with arms and hands, shaping the objects of our daily lives (i.e., touchscreens, steering wheels, handles, doorknobs, push buttons, keyboards, etc.). As a result, impairment to arm function impairs not just our mobility but also our ability to interact with our surroundings, affecting aspects of health, safety, independence, and socialization. Understanding and addressing arm impairment, therefore, is vitally important to millions of individuals living with functional deficits from both traumatic and non-traumatic injuries.

1.1. Impairment Prevalence and Societal Impact

The largest contributor to motor impairment globally is cerebrovascular accident (CVA), of which there are approximately 10 million cases per year having survived an ischemic or hemorrhagic stroke. In more than 85 percent of cases, functional deficits of motor control occur [1]. Range of motion (ROM) is often impaired, particularly in the execution of reach extension movements of the arm involving support against gravity [2,3]. Losses in arm function and mobility from stroke alone affect millions of survivors, and the number is projected to continue to rise due to increases in (1) life expectancies, (2) the prevalence of stroke with age, (3) the number of baby boomers reaching the age of higher prevalence, and (4) post-stroke survival rates. Addressing the deficits caused by stroke and other CVAs has been a major motivating factor behind the recent proliferation of robotic solutions for clinical assessment and training in the arm and hand.

Deficits in arm mobility are linked to reduced quality of life, affecting aspects of physical and mental health, hygiene, safety, and independence. Unimpaired movement requires an intact musculoskeletal system and bilateral communication between nervous and muscular systems. Jointly referred to as the neuromusculoskeletal system, an injury to any one of its subsystems can significantly impair mobility. As a result, the correct identification of underlying sources of impairment is important for optimal treatment and recovery. Factors in CVA patients that have historically been cited as contributors to functional deficits include muscle weakness, increased or decreased tone, spasticity, co-contraction, or abnormal muscle synergies [2,4–7]. However, neither the relative contributions of these factors, nor their underlying sources, have been determined. Illustrating the difficulty of identifying sources of impairment, muscle weakness can be masked by co-contraction or abnormal synergies; both weakness and low muscle tone may lead to a lack of control, but so too might changes in muscle activation such as temporal and spatial changes in amplitude, frequency, or resolution. As a result, the complex and multi-disciplinary nature of neuromotor function has presented a significant barrier to its comprehensive study and understanding.

1.2. The Assessment Gap

Despite improvements in our ability to assess and rehabilitate arm deficits, our knowledge about underlying sources of impairment and related sequela has remained limited. The relative contribution to deficit of the many factors that may contribute to lost function has remained elusive with previous experimental setups, with measurements often hampered by one or more limiting factors, such as (1) subjectivity, (2) the range or resolution of measurement, or (3) the breadth of measurement focus [8].

Subjectivity—Standard assessment tests that are manually administered are typically scored by a trained observer. Although some tests achieve high ratings for inter-rater reliability (a measure of how consistently different raters would score the same individual), subjectivity cannot be completely removed unless the determination of the measure can be fully automated.

Range and resolution—Many assessments use a discrete point scoring system; for example, the Fugl–Meyer Upper-Extremity Assessment (FMA-UA) is scored from 0 to 2, where 0 means the task cannot be performed at all and 2 means it can be performed as

well as with the unimpaired side [9]. This system, while usually affording high inter-rater reliability, offers poor resolution while at the same time making it difficult to show change, particularly at the upper and lower ends of the scale. These are called floor and ceiling effects and are acknowledged as significant barriers to progress tracking in a number of highly utilized assessments such as the FMA-UA, the Action Research Arm Test, the Wolf-Motor Function Test, and others.

Breadth of focus—As described above, deficits can occur in any of several subsystems and in some cases with similar functional impact. Therefore, it is important that a comprehensive measurement system include measures from the potentially affected subsystems, not just their functional outcomes.

1.3. Key Design Considerations

In the development of a machine for comprehensive measurement, several key design considerations emerge, including the importance of an exoskeleton vs. an end-effector design, the ability to take bilateral vs. unilateral measurements, and the inclusion of a lateral vs. axial donning approach.

1.3.1. Exoskeleton vs. End Effector

Among robotic systems for upper-extremity assessment and training, both exoskeleton and end-effector approaches are common. Exoskeletons provide structural links along the length of the arm with multiple points of human–robot attachment (HRA). Their kinematics mimic anatomical motion by aligning robot joint axes with approximations of human joint axes. End-effector robots, on the other hand, often use a single HRA at the hand and/or forearm and enable an end-effector workspace that typically coincides with a subset of the user's workspace [10].

Exoskeletons are typically more complex, requiring linkage geometries that fit around and align with the user, while end effectors can be made of simpler geometries with minimal regard to user geometry except at the point of contact, usually the hand or forearm. For safety reasons, the end effector's entire workspace is typically limited to a subset of the user's workspace since robotic workspace that falls outside the workspace of the user increases the risk of injury. Exoskeletons, on the other hand, are designed to align with joints and have range limits that more closely align with users' range of motion limits, facilitating a much larger overlap between the robot and user workspace.

Exoskeletons have a clear advantage in the workspace, but achieving high transparency within the workspace is still nontrivial due to the number of individual links and bearing connections required to support the mobility of the arm. However, while end-effector devices that utilize distal HRAs allow for lighter and simpler structures, their simplicity also makes them unable to provide single-joint control, limiting the ability of these devices to guide and support users [11] and limiting their potential for the assessment of individual joints or segments of the body.

Related to the exoskeleton vs. end-effector debate, there is ongoing controversy over whether training with 2D or 3D movements is better for rehabilitation. It is a debate of both cost and effectiveness. Exoskeleton devices that support spatial (3D) task training are typically more expensive than those that are limited to planar (2D) movements. Despite significant advantages and disadvantages to each, ultimately, the key factor is the benefit to the user being trained. The real question becomes the following: Do the benefits of 2D task training carry over into less-constrained activities of daily living? Although comparison studies of such devices are still limited, a recent study [12] found that the InMotion ARM (end effector) was more beneficial for patients with moderate to severe deficits at four weeks post-stroke than the ArmeoPower (exoskeleton). The authors proposed that this population may have benefited from the more task-oriented training approach, lower device inertia, and simpler movements provided by the InMotion ARM end effector [12]. Interestingly, a similar meta-analysis comparing end-effector and exoskeleton robots for finger–hand

motor recovery found the opposite result, with exoskeletons outperforming end-effector devices [13], although potential reasons for the difference were not provided.

While end-effector robotics may be lower in cost, the ability of exoskeletons to measure and/or assist at the level of individual arm segments or joints is an invaluable benefit for assessment. Because exoskeletons are directly in contact with their user over the length of the limb, their motors can provide assistive or resistive forces to individual joints and, therefore, provide segment-specific test conditions in the assessment of function. Using an end-effector robot for assessment provides quantitative information only at the point of contact and, therefore, provides a cumulative assessment for all the joints that contribute to controlling end-effector position and orientation. Limiting movement to a 2D plane can be attractive and, in some cases, necessary in order to eliminate confounding factors in a study; however, it is important to acknowledge that such constraints impose limitations on the type of task that can be performed and, therefore, the likeness to real-world tasks that can be assessed.

1.3.2. Bilateral vs. Unilateral

The choice of using bilateral (left- and right-arm) vs. unilateral (single-arm) systems is another important aspect in comprehensive measurement. The assessment of arm function can be highly individual, affected by aspects of body size, shape, composition, and the type or severity of impairment, complicating inter-subject comparisons as well as comparisons to population norms. Some impairments affect mainly one side of the body, making the opposite side of the body the most relevant intra-subject baseline comparison. Even if compatible for use with both the left and right arms, a unilateral system is limited to measuring one arm at a time, often sacrificing range of motion for the ability to fit either arm, and adds significant setup time to compare the left arm with the right. Furthermore, interlimb coordination and the ability to perform bimanual tasks are important aspects of arm function that are difficult to assess without a bilateral assessment system.

1.3.3. Importance of Lateral Arm Attachment

Early exoskeletons employed large-diameter thin-section bearings that surrounded the arm to support the rotation of the upper and lower arm segments about their long axes [14,15]. This election, however, complicated the donning process, particularly for individuals with arm impairment. Recognizing the importance of facilitating ease-of-use in the attachment process, recent exoskeleton developments for rehabilitation have almost exclusively employed an open attachment design that allows the user's arm to be secured and released from the device laterally via straps [16,17].

1.4. State-of-the-Art Review

Since the early exoskeletons of the late 1960s [18] and human extenders of the early 1990s [19], exoskeletons have steadily increased in number and capability. In the field of rehabilitation, their capacities for training and assessment have grown along with their number of active joints, range of motion, and multi-domain sensing systems.

1.4.1. Exoskeletons for Rehabilitation

In the past five years alone (2019–2023), more than 25 review papers have been published on the topic of rehabilitation robotics for the upper limbs [20–47]. These include reviews of systems targeting function in the shoulder [23], elbow [24], wrist [25], or hand [26,27]; systems that include support for multiple arm joints [28–38]; reviews comparing end-effector to exoskeleton-based approaches [13,39,40]; exoskeleton control methods [41,42]; human–robot interaction dynamics during rehabilitation [43–45]; and the recent incorporation of artificial intelligence and machine learning into the exoskeleton rehabilitation approach [46,47].

The vast majority of shoulder-to-wrist exoskeleton designs use between five and seven degrees of freedom (DOFs) per arm, with varying combinations of joints. The seven-

degree-of-freedom (DOF) Harmony exoskeleton [17], for example, spans shoulder elevation to forearm rotation, while the seven-DOF EXO-UL8 [48] and ARMinV [49] robots span shoulder flexion to wrist deviation. A more recent system, called ANYexo2 [50], includes a motor for each of the nine joints between the shoulder and wrist. With a particular focus on minimizing mechanism inertia, the motor axes of ANYexo2 have been positioned in non-orthogonal arrangements and links placed close to the axes of revolution. The resulting system achieves control bandwidths for the shoulder approaching two times the reported speeds of shoulder motion during typical ADLs [16], which are about 3 rad/s [51]. With any design approach, there are trade-offs determined by system requirements. For ANYexo2, the five motor placements at the shoulder are positioned such that two of the motors cross over the sagittal plane, preventing its use in a bilateral configuration.

1.4.2. Sensor-Based Assessment

Sensor-based systems offer a higher-precision quantification of signals than can be achieved with the manual scoring systems of traditional clinical assessments. Therefore, researchers are investigating new assessment methods that are more sensitive to change and rely less on therapist judgment. A recent literature review lists several sensor-based metrics that show strong inter-rater reliability and reviews their validity with traditional clinical assessments [8]. The more-promising metrics with both high reliability and validity scores included the mean speed, the number of velocity peaks, and the task time [8]. However, few studies were found that provided a multi-domain approach that included measurements of brain and muscle activity.

The primary non-invasive measures of brain and muscle activity utilize electroencephalography (EEG) on the surface of the scalp and electromyography (EMG) on the surface of the skin above a contracting muscle belly. Other biosignals include electrocardiography (ECG) for the heartbeat and electrooculography (EOG) for eye movement. Limited prior work has utilized EMG or EEG measurement in conjunction with exoskeleton robotics for the upper [52–54] and lower limbs [55,56]. While some systems utilize biosignals purely for assessment, such as to characterize movement smoothness [57] or identify movement primitives exhibited by persons recovering from stroke [58], the majority of work has focused on decoding EEG signals for brain–machine interfaces (BMIs) or on surface EMG (SEMG) signals for the SEMG-based control of robotics. Other groups are working to identify more effective methods of providing rehabilitation training; however, few efforts are being focused on finding the underlying sources of impairment.

1.5. Project Overview

The instrument described in this work has been conceived and developed with the aim of supporting both 2D and 3D tasks involving the shoulder, elbow, wrist, and/or hand of either the left or right side, or both arms simultaneously. Termed the BLUE SABINO, for BiLateral Upper-limb Exoskeleton for Simultaneous Assessment of Biomechanical and Neuromuscular Output, this new robotic exoskeleton instrument measures both activation and movement in order to enable full 3D reach-and-grasp tasks while measuring kinematic, dynamic, and neurological function. The goal of the system is to make comprehensive assessment possible, unlocking barriers to identification of sources and significance of factors in motor impairment not previously discernable with available measurement equipment. This paper will focus on the kinematics, controllers, and mechanical, electrical, and neuromuscular hardware used in the design of a nine-DOF arm exoskeleton, which was inspired by previous exoskeleton systems [48,59]. The system design and layout are explained in Section 2. Preliminary validations of the design's ability to simultaneously capture motion, interaction forces, and neuromuscular activity are reported in Section 3.

2. Materials and Methods

The BLUE SABINO is a third-generation design, built from two prior successful bilateral systems: EXO-UL7 (aka CADEN-7) [59] and EXO-UL8 [48] (Figure 1). With a primary

focus on assessment, and a secondary focus on training, the BLUE SABINO development targets the simultaneous collection of measures from the entire neuromusculoskeletal system, including intention to move, muscle activation, and the resulting kinetics and kinematics of arm movement. Importantly, the system aims to support such measures during activities of daily living (ADLs), such as grasping, positioning, manipulating, and releasing objects within the workspace of the shoulder, elbow, and wrist.

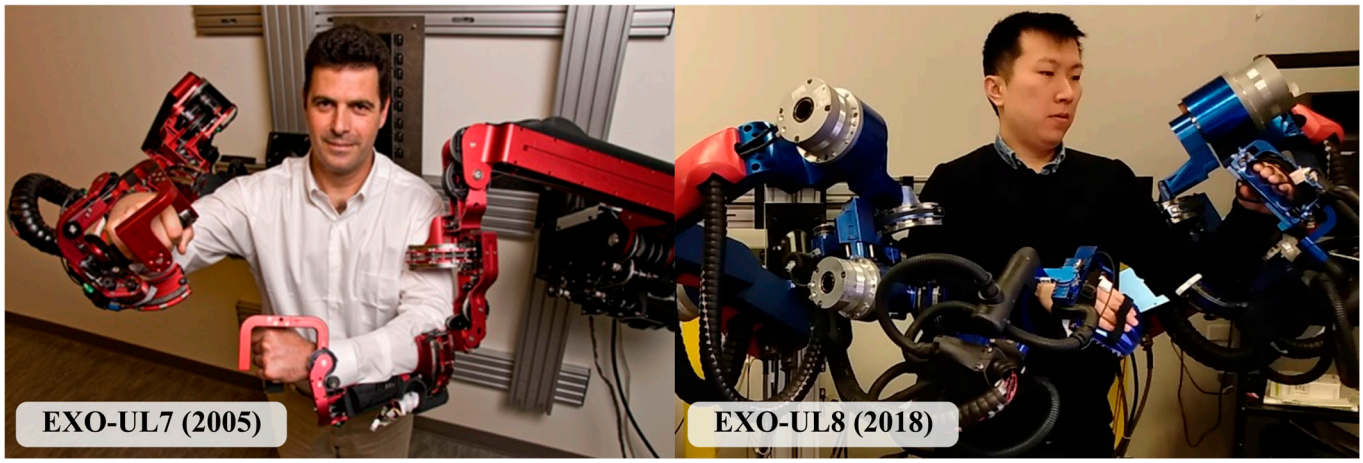

Figure 1. Bilateral exoskeleton predecessors to the BLUE SABINO: (**LEFT**) the EXO-UL7 and (**RIGHT**) the EXO-UL8.

2.1. System Requirements

Integral to the system requirements, common objectives for exoskeleton robotics include (1) safety, (2) usability, and (3) functionality.

Safety—Safety is paramount to all systems that interface with the human body. Safety is incorporated into the mechanical, electrical, and software systems to prevent unwanted behavior that could occur when using the device. For example, the range of motion of the joints is limited using mechanical hardstops and software limits to prevent hyperextension. Safety systems should consider not only foreseeable but also unplanned incidents. E-stops are designed to shut down the system by turning off the electrical power at the motors and using software disabling the controller input sent to the drivers. The E-stops are conveniently placed in locations accessible to the operator and subject and can be pressed at any time.

Usability—A significant emphasis should be placed on the ease of donning (putting on) and doffing (taking off), as this is important for both subjects and operators during impairment assessment after stroke. Some of the most crucial design elements that complicate the exoskeleton donning/doffing process are the use of open vs. closed bearing designs around axial joints (i.e., shoulder internal/external rotation and forearm pronation/supination) and the ease of attachment to the HRA interfaces. Closed bearings (i.e., bearings that fully encircle the arm) require passing an arm through the center of the bearing, like a sleeve, which is a difficult task for an impaired arm. The HRA design, similarly, makes a significant difference in the system's ease of use for the operator, determining the complexity of size adjustment and securement to the subject.

Functionality—The functional objective of the system is to assess and train arm and hand function during ADL tasks. These tasks require grasp-and-release movements and the ability to contact objects with the fingertips. The system's functionality would also be enhanced by the ability to measure unwanted compensatory shoulder movements that may occur during intense effort as a result of flexion synergies [60].

To investigate system requirements from a clinical perspective, a focus group was conducted with eleven clinicians at St. Luke's Rehabilitation Institute, including seven Occupational Therapists (OTs) and four OT Assistants (OTAs), with an average of 5 years

of experience in their current specialty [61]. Ten of the eleven participants also responded to a survey of 32 potential system attributes to rate their level of importance. Outcomes from the focus group and survey highlighted the importance of adapting the system movements and interaction forces to the needs and limitations of individual users. The responses recognized the importance of a bilateral system, an exoskeleton vs. end-effector approach, arm and hand motions that are commonly targeted in therapy, and the ability to support users in a seated posture that may be confined to a wheelchair.

In the survey, participants were asked to rate each attribute from 0 (unimportant) to 3 (extremely important). An average ranking was then computed for each attribute. Two attributes were ranked extremely important by all ten respondents, and just one attribute was not ranked extremely important by any respondent; that same attribute was also ranked unimportant by four respondents and was the only attribute to be ranked unimportant by any respondent. The results of the attribute survey, shown in Table 1, highlight the importance of (1) adjustability to the needs of the patient (e.g., variable/customizable resistance, motion, size, and difficulty); (2) the provision of supported movement from the shoulder to the fingers; (3) the provision of meaningful feedback to both patient and therapist; and (4) a preference for bimanual over unimanual training support. Overall, the rankings were high (26 of 32 receiving above 2), indicating a close fit between the attributes included in the survey and the desirable attributes from a clinical perspective. At the low end of the rankings, only 6 of 32 attributes were rated below 2 (important).

Of the eleven participants, three reported having some prior experience with upper-extremity robotics devices, including products from Neofect and Bioness. The focus group session lasted 45 min and was audio-recorded for accuracy. The main objectives of the focus group were to gather clinical perspectives on

1. Measures that would be of use to characterize patient performance and any change in performance over time.
2. Aspects of instrument design that would make the BLUE SABINO clinically useful.

To support the discussion, therapists were provided with a document outlining the project, the goals of the focus group, example measures that could potentially be obtained from a system, and the list of 32 potential system attributes. The major themes of the 45-min discussion centered on the importance of

- Short setup time (<10 min for set up, leaving >35 min for assessment).
- Providing instant feedback for the patient and therapist (motivation and insights).
- Detecting active muscle groups (to differentiate sources of deficit).
- System sensitivity to detect incremental change throughout recovery (helps to justify the continuation of care).

The strengths and weaknesses of the FMA-UE as an assessment test and the suitability of the system for inpatient vs. outpatient care were also discussed. Acknowledging the popularity of the FMA-UE, participants felt that the FMA-UE provides a good starting point metric from which robotic measures can be built. They also felt that instruments like BLUE SABINO are best aligned with outpatient care where functional improvement drives the continuation of treatment (with insurance coverage), whereas in-patient care requires a short setup time and there is a greater preference for using the device for training after the assessment. Key assessment metrics highlighted by the group included the following: active range of motion, movement accuracy, shoulder–elbow coordination, joint angles, smoothness, and proprioception. The anthropometric requirements of the system are summarized in Table 2.

Table 1. Clinical requirements of a robotic system, prioritized by therapist-perceived level of importance from Extremely Important (3) to Unimportant (0) *. Numbers in columns 2–4 indicate number of therapist votes. Weighted rank is computed from the sum of rank score times the number of votes at each rank divided by the total number of voters.

	System Attribute	Ranking *			Weighted Rank
		Extremely Important (3)	Important (2)	Not Very Important (1)	
1.	Adjusts resistance based on patient strength	10			3
2.	Accommodates a patient in a wheelchair	10			3
3.	Usable in a seated position	9	1		2.9
4.	Allows diagonal movement	9	1		2.9
5.	Allow different hand/finger grips to be practiced	9	1		2.9
6.	Allows full ROM movements of all arm joints	9		1	2.8
7.	Allows planar movement (e.g., in the sagittal plane)	8	2		2.8
8.	Has virtual ADL-specific activities	8	2		2.8
9.	Able to accommodate bariatric (large body) patients	8	2		2.8
10.	Gives performance feedback to the patient	8	2		2.8
11.	Gives performance feedback to the therapist	8	2		2.8
12.	Adjusts difficulty of movement task based on patient capability	7	2		2.8
13.	Allows bimanual performance of goal-directed tasks that are not mirror movements	7	3		2.7
14.	Provides assistance as needed from robot with shoulder, elbow, or wrist movement if patient cannot generate	7	3		2.7
15.	Provides strength exercises	7	2	1	2.6
16.	Provides range of motion exercises	7	2	1	2.6
17.	Assistance as needed from robot with finger movements	6	4		2.6
18.	Able to be used without trunk constrained to backboard	6	4		2.6
19.	Allows unimanual performance	5	5		2.5
20.	Designed as a bimanual exoskeleton with support for each joint (Note: contrast this with the design feature below)	4	4		2.5
21.	Able to accommodate pediatric (small body) patients	5	4	1	2.4
22.	Provides harness for trunk to be secured to a backboard	5	4	1	2.4
23.	Has goal-directed “games” to allow practice of non-ADL movements	4	6		2.4
24.	Requires little pre-performance adjustment from therapists	3	6		2.3
25.	Allows simultaneous mirrored movements of both arms	2	8		2.2
26.	Requires specific pre-performance adjustment from the therapist to ensure good fit	1	8		2.1
27.	Transportable	3	3	4	1.9
28.	Compact	2	5	3	1.9
29.	Movement from contralateral limb assists opposite limb	2	4	3	1.9
30.	Usable in a standing position		7	3	1.7
31.	Designed as an end-effector system with patient contact only at a handhold (Note: contrast this with the design feature above)	1	1	3	1.6
32.	Usable in a prone position		1	5	0.7

* The Unimportant (0) category is not shown as only the lowest-ranked attribute (Usable in a prone position) received any ratings in that column, for which it received four.

Table 2. Anthropometric design requirements.

Anthropometric Measure *	5th Percentile Female (cm)	95th Percentile Male (cm)	Range (cm)
Seat-Shoulder Height ($H_{S\text{-}SH}$), seat to join center	46.4	59.7	13.2
Shoulder Width (W_{SH}), center to center	29.4	39.2	9.8
Upper Arm Length (L_{UA}), center to center	25.3	30.3	4.9
Upper Arm Circumference (C_{UA}), muscles relaxed	21.8	35.1	13.3
Forearm Length (L_{FA}), center to center	22.5	26.9	4.4
Forearm Circumference (C_{FA}), muscles relaxed	19.9	32.7	12.8
Hand Length (L_{HD}), crease to fingertip	15.9	20.7	4.8
Hand Grip Length ($L_{HD\text{-}GR}$), crease to grip center	6.7	8.3	1.6
Hand Circumference (C_{HD}), around grip center	17.5	23.0	5.5
Hand Width (W_{HD}), across grip center	7.0	9.6	2.6
Hand Thickness (T_{HD}), across middle MCP joint	2.5	3.7	1.1

* Distances to the shoulder and elbow are measured with respect to their approximate joint centers for flexion/extension. Lengths of the hand are measured with respect to the wrist crease at the base of the palm. MCP = metacarpophalangeal [62,63].

In support of ADL movements, the system requirements for mobility are summarized in Table 3. These design requirements were selected based on mapped ADL motion-capture data from [62]. In the table, the ADL ranges are contextualized with biomechanics data from Tilley [63], NASA [64], and Ludewig et al. [65,66]. The ADL measures represent a subset of motions most interesting for rehabilitation and therapy, while the biomechanics ranges provide a clearer sense of the absolute range of motion of a healthy user. BLUE SABINO's mobility covers approximately 95% of ADL motion and 86% of the healthy 50th-percentile biomechanical range (83% of healthy 50th-percentile females, and 89% of healthy 50th-percentile males).

Table 3. Joint ROM requirements for combined male/female (M/F) population in comparison to ROM required in ADLs.

Joint	95% of ADL ROM (deg) *	Anthropometric M/F ROM (deg) **	
		Minimum	Maximum
Shoulder Protraction/Retraction	55.9	35.0 †	
Shoulder Elevation/Depression	42.1	40.0 †	
Shoulder Abduction/Adduction	164.3	142.0	207.5
Shoulder Flexion/Extension	110.7	202.5	284.5
Shoulder Internal/External Rotation	108.9	84.5	181.5
Elbow Flexion/Extension	120.5	122.0	160.5
Forearm Pronation/Supination	215.7	161.6 ‡	258.4 ‡
Wrist Flexion/Extension	131.4	100.5	177.0
Wrist Radial Ulnar Deviation	35.9	33.0	76.5

* Data from [62]; ** Data from [63]; † Data from [65,66]; ‡ Data from [64].

2.2. Mechanical Systems Design

The BLUE SABINO final system design is composed of two seven-DOF arms supported by two-DOF shoulder modules, shoulder-width adjusting base structures, a height-adjustable chair, and two optional 12-DOF (six active, six passive) hands (Figure 2). The chair height is adjusted to vertically align the user's shoulders with the exoskeleton shoulder centers. The chair position and base width are adjusted to align the shoulders in the horizontal plane. The two-DOF shoulder module, called the Parallel Remote Inclusion of Shoulder Mobility (PRISM), allows for continuous shoulder alignment during scapulothoracic movement and has been detailed in [67]. Additional length adjustments in the exoskeleton's upper- and lower-arm links allow for alignment with the elbow and wrist joints. Novel aspects of the design include the PRISM module, the inclusion of a three-fingered hand exoskeleton, adjustable rigid orthoses along the arm and hand, and the support of all degrees of freedom in a bilateral design.

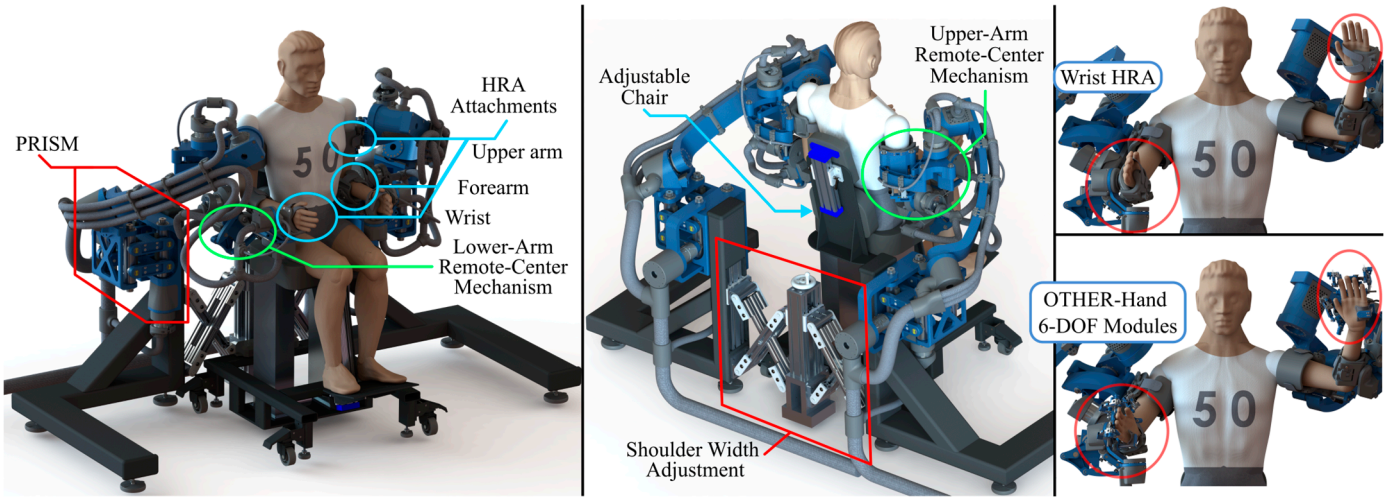

Figure 2. The BLUE SABINO instrument design is composed of a width-adjustable base, height-adjustable chair, length-adjustable upper arm and forearm segments, size-adjustable HRA attachments, remote-center four-bar mechanisms, two-DOF shoulder modules (PRISM), and optional 12-DOF hand modules.

2.2.1. Human Arm Joints: Seven DOF vs. Nine DOF

In both previous generation systems, the human arm was represented as a seven-DOF shoulder-to-wrist mechanism, comprised of a three-DOF shoulder, a one-DOF elbow, a one-DOF forearm, and a two-DOF wrist [48,59]. A seven-DOF shoulder-to-wrist design allows the hand to reach a position and orientation with multiple possible arm poses, facilitating task-specific reach patterns and obstacle avoidance. Despite the mobility redundancy supported, this seven-DOF arrangement treats the shoulder center as a stationary point, precluding movements of the arm that involve joints of the scapula and clavicle. This prohibits shoulder movements such as up/down and fore/aft shrugs that are commonly employed by populations both with and without cortical damage [68,69]. To allow for the full assessment of shoulder mobility, two additional joints are needed to support movements of the scapula and clavicle. These movements are termed elevation/depression (up/down) and protraction/retraction (fore/aft), bringing the total number of arm DOFs to nine, as shown in Figure 3.

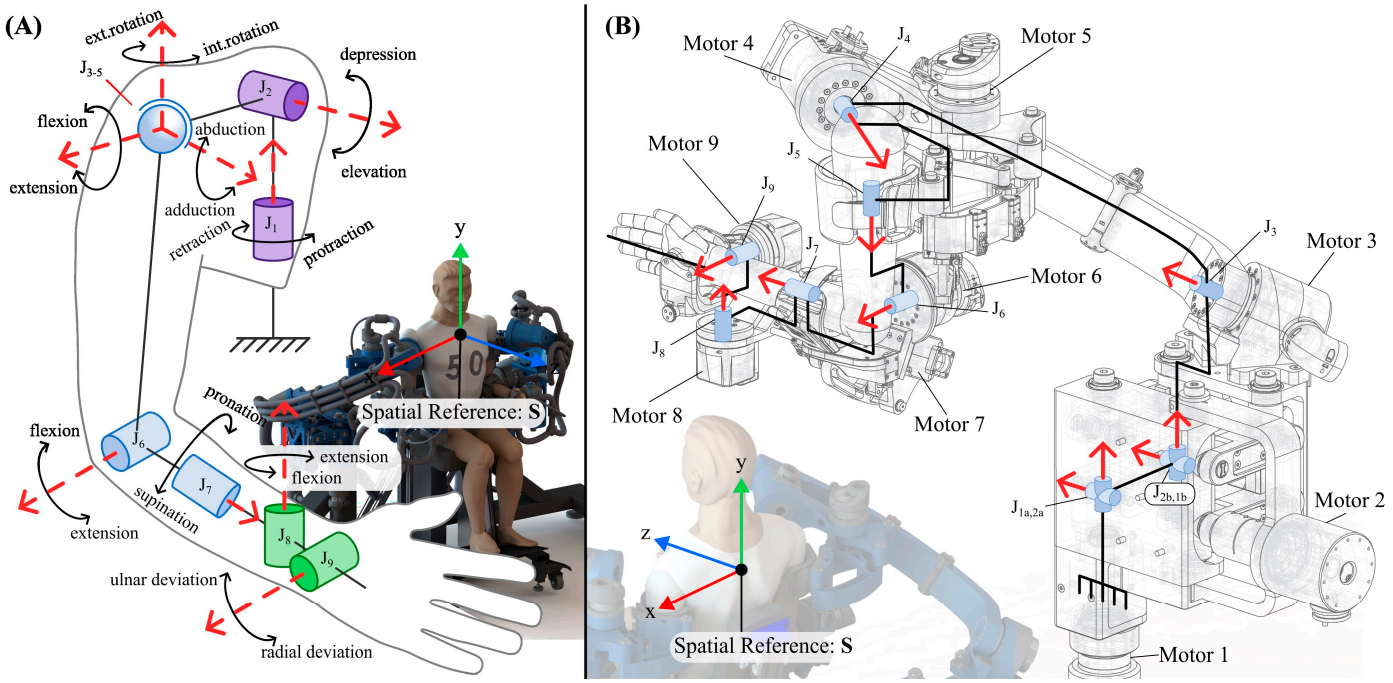

Figure 3. The kinematics of the human arm from the shoulder to the wrist can be represented by nine degrees of freedom. (**A**) Joints J_1–J_9 and their corresponding anatomical axes (indicated by red dashed arrows oriented along the axes of rotation). (**B**) The kinematics of BLUE SABINO accommodate these nine degrees of freedom per arm (here, red arrows indicate the selected positive orientation of each joint's rotation axis).

2.2.2. Exoskeleton Arm Design

The arm design follows the same kinematic structure as its predecessor (EXO-UL8) with the addition of two joints to support the translation of the shoulder. Thus, EXO-UL8 joints 1–7 become BLUE SABINO joints J_3–J_9 (Figure 3A). While the kinematics of these joints remain the same, the BLUE SABINO arm linkages have been redesigned with significant changes occurring in remote-center (RC) mechanisms for axial rotation about the upper arm and forearm, as well as the addition of the shoulder translation mechanism.

The nine-DOF arm structure is composed of a serial chain of eight linkage assemblies driven by nine motors (Figure 3B). Five of the assemblies form rigid links connecting one motor to the next, while the remaining three form movable assemblies composed of variations of parallel-link mechanisms located at the upper arm, the forearm, and the shoulder (Figure 4).

The shoulder structure maintains the orientation of axes from the EXO-UL series exoskeletons, which place the shoulder singularity at an edge of the arm's workspace that is both difficult and rare to reach [64]. The largest link (L_1 in Figure 4) is used to place motor 3 (M3) at a distance from the shoulder, allowing a large workspace for the elbow. The shape of link L1 allows motors M4 and M5 to articulate their corresponding linkages while maintaining clearance between links.

The parallel mechanisms at the upper arm and forearm are used to couple the axial motion of an arm segment to a motor axis that is offset to the side of the arm, forming a triple-pivot parallel mechanism [70] similar to that used in the upper arm [71] and forearm [17] of two prior exoskeleton designs. Additional details of the triple-pivot parallel mechanism implemented in the upper arm and forearm can be found in Appendix A.

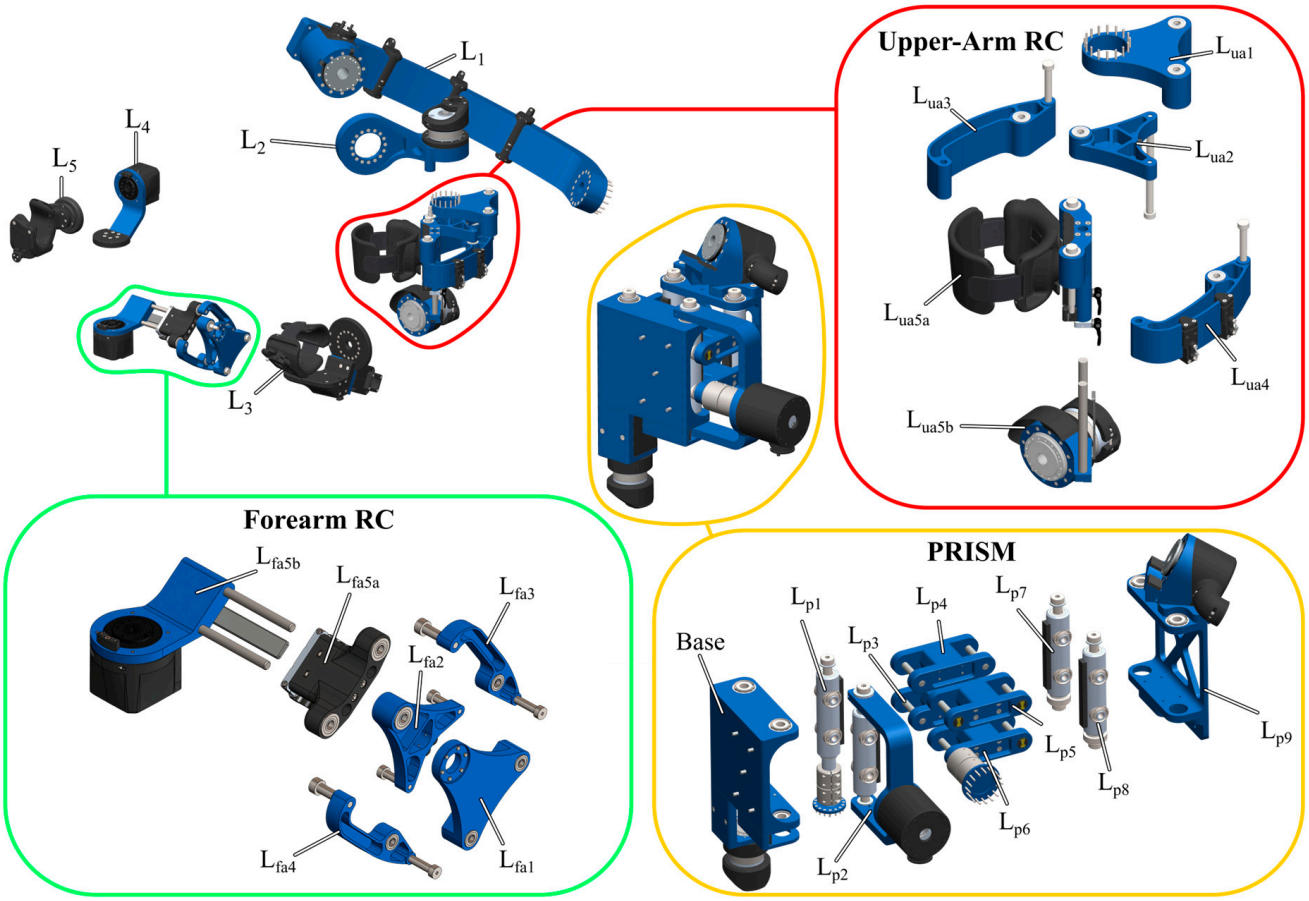

Figure 4. BLUE SABINO rigid body links. The right-side rigid links of the right BLUE SABINO arm are shown in an exploded view ((**top left**) and (**center**)). Three of the links form movable assemblies composed of various parallel link mechanisms. The upper-arm (**top right**) and forearm (**bottom left**) remote-center mechanisms are composed of five primary links and an additional link for arm-length adjustment. PRISM (**bottom right**) is constructed with ten links, nine moving, and one stationary base.

The parallel mechanism for the shoulder (previously shown in the center and bottom right of Figure 4) is composed of two sets of orthogonal four-bar mechanisms that form an imaginary cube, where the cube edges are rigid and allowed to pivot about vertices, while the front and back faces of the cube remain square in shape. One four-bar set aligns with the top and bottom faces of the cube, while the other set aligns with the left and right faces. Each of the four horizontal links is connected proximally to a stationary bracket aligned with the front face of the cube and distally to a moving bracket aligned with the back face. Both ends of each of the four links connect to each bracket through a two-DOF universal joint located at each of the cube's eight vertices. With the proximal bracket fixed to the base structure, the distal bracket is allowed to translate with the distal end of each link, while the parallelograms formed by links on the left, right, top, and bottom faces change shape with the movement of the distal bracket; the parallelograms formed by links on the left and right faces change shape with up and down movement, while the parallelograms on the top and bottom faces change shape with left and right movement. The front and back faces remain parallel throughout movement in both directions. The resulting kinematic constraints effectively mimic scapulothoracic movement, translating the entire arm exoskeleton (mounted to the distal bracket) along the surface of the sphere, where the radius of the sphere is defined by the length of the links connecting front and back faces—approximately the length of a human clavicle. As described in [67], the design

results in a two-DOF mechanism that can be actuated to drive the (1) protraction–retraction and (2) elevation–depression of the shoulder.

2.2.3. Exoskeleton Hand Design

The hand exoskeleton, termed the "OTHER Hand", was developed in collaboration with researchers at the UCLA Bionics Lab to enhance the hand function of both the University of Idaho's BLUE SABINO and UCLA's EXO-UL8 systems. The primary objectives of the hand were (1) to add grasping ability to both exoskeleton systems; (2) to support the independent control of the thumb, index, and middle fingers in order to allow for a wide array of grasp types; and (3) to keep the fingertips and palm open to enable direct interaction with real objects.

2.2.4. Human–Robot Attachment Design

Human–robot attachments (HRAs) require an intimate fit with their wearer to ensure a stable, comfortable connection. A poor fit in HRAs can result in gaps between the orthosis and user that introduce delays or spikes in sensor readings, in addition to points of higher stress that reduce aspects of comfort and safety. Achieving comfort across different body shapes and sizes is particularly challenging at the hand and forearm due to bony prominences and the movement of underlying bone structures during pronosupination. Scan geometry and elliptical approximations of arm geometry were used to facilitate the design of an anthropomorphic attachment in SolidWorks 2021. The upper-arm interface (Figure 5A) is based on two aligned elliptical shapes, whereas the forearm interface (Figure 5B) is generated from an elliptical model derived from best-fit ellipses to scanned forearm geometry [72]. The hand interface surface is modeled from a 3D-scanned hand that was processed in Blender 3.0 and imported into SolidWorks to generate a bent U-shaped contour formed around the base of the thumb (Figure 5C). The surfaces are offset by 2 mm from the skin to allow room for padding material. The upper-arm and forearm orthosis surfaces are each 10 cm long.

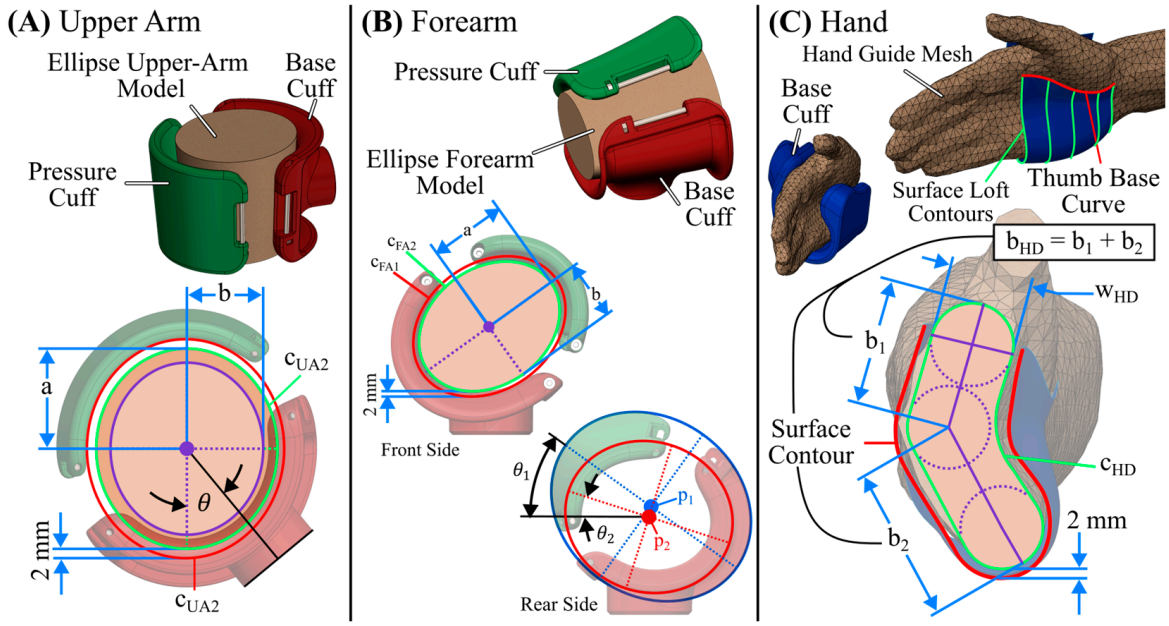

Figure 5. Anthropomorphic arm modeling for human–robot attachments (HRAs). Elliptical profiles for proximal and distal ends of the (**A**) upper arm and (**B**) forearm, and (**C**) lofted bend-U-shaped profile for the hand.

To further improve the fit with the user, the orthoses are each size-adjustable and designed with internal sliding mechanisms that allow their widths to be increased/decreased with thumbscrews, as shown in Figure 6. The slides are spring-loaded and widen as the thumbscrew is loosened. The upper-arm and forearm orthoses also include a smaller thumbscrew that can be used to lock the slide in place.

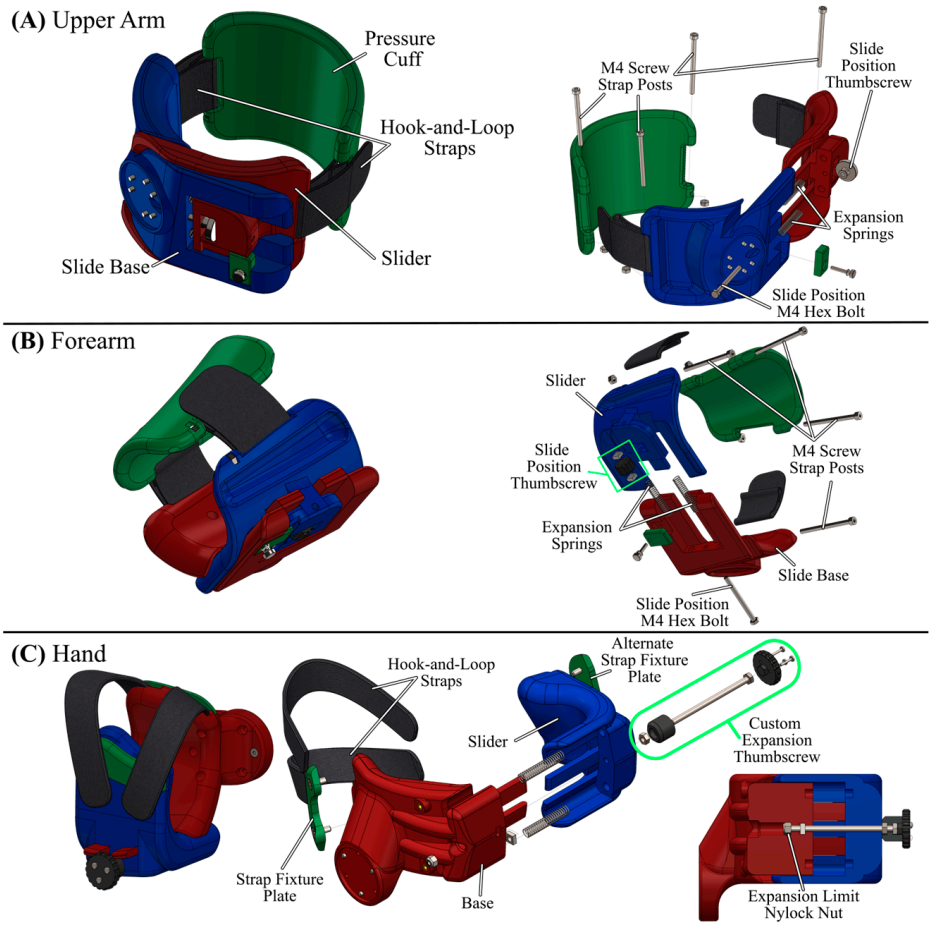

Figure 6. Adjustable HRA orthotic designs and exploded assembly views. (**A**) The upper-arm orthosis. (**B**) The forearm orthosis. (**C**) The hand orthosis.

The upper "pressure cuff" is optional for the upper arm and forearm to aid with the distribution of strap tension to a larger surface area of the arm. The hand orthosis uses two thin foam-padded straps on either side of the thumb to comfortably fix the hand position within the orthosis and prevent the forearm from sliding axially in the exoskeleton while providing responsive force measurement.

2.3. Manipulator Kinematic and Dynamic Modeling

Kinematic and dynamic models of the human arm and nine-DOF exoskeleton are developed for application in a control simulation. The "home" orientation of the right-side manipulator is shown in Figure 7, as are points and vectors q and ω, which denote the coordinates and directions of the manipulator's joints.

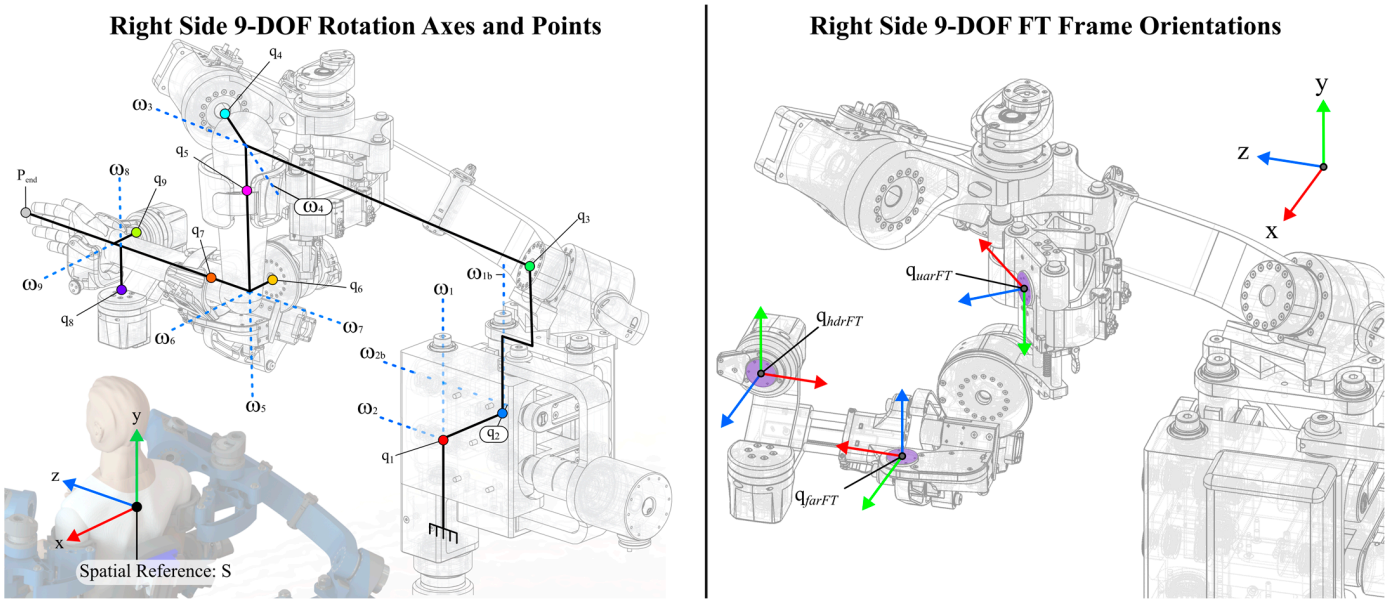

Figure 7. Definition of manipulator points (q), axes (ω), and force sensor body frames.

2.3.1. Forward Kinematics

The accurate control of BLUE SABINO requires forward kinematic relationships between the measured joint angles and link positions, as well as knowledge of key locations of the human arm, the force sensor body frames, and the center of mass coordinates of the robot's links. Combined, this awareness allows for the use of force sensors to drive the robot (i.e., force control), the implementation of trajectory tracking (i.e., position control), and modeling the effect of dynamic forces on the system, such as friction and gravity (i.e., control compensation), to improve accuracy. Our approach used the product of exponentials formulation to derive the forward kinematics [73,74]. For the sake of brevity, only forward kinematics for the end effector and the force sensors on the right side are described here. A complete formulation of BLUE SABINO's forward kinematics, including both arm sides and all of the robot's rigid links, is available in [75].

Using the joint axis location and direction vectors q and ω defined in Figure 7, homogeneous coordinate frames and points can be computed for each of the manipulator links as functions of the robot's joint positions, θ. Transforms are determined using the definitions for a twist, ξ, and for the hat operator, ˆ, which are

$$\xi = \begin{bmatrix} -\omega \times q \\ \omega \end{bmatrix}, \hat{\xi} = \begin{bmatrix} \hat{\omega} & -\omega \times q \\ 0 & 0 \end{bmatrix}, \hat{\omega} = \begin{bmatrix} 0 & -\omega \\ \omega & 0 \end{bmatrix}. \quad (1)$$

Given the manipulator's joint positions, θ_i, the position of the end effector point, P_{end}, with respect to the fixed spatial coordinate frame, is

$$P_{end} = e^{\hat{\xi}_1\theta_1} e^{\hat{\xi}_2\theta_2} e^{\hat{\xi}_3-\theta_2} e^{\hat{\xi}_4-\theta_1} e^{\hat{\xi}_5\theta_3} e^{\hat{\xi}_6\theta_4} e^{\hat{\xi}_7\theta_5} e^{\hat{\xi}_8\theta_6} e^{\hat{\xi}_9\theta_7} e^{\hat{\xi}_{10}\theta_8} e^{\hat{\xi}_{11}\theta_9} g_{st,end}(0). \quad (2)$$

2.3.2. Body Manipulator Jacobians and Human–Robot Interaction Applied Force

Accurate force control relies on mapping measurements of human–robot interaction forces and torques to joint reaction torques about the manipulator's actuated axes. Interaction forces and torques are measured by sensors at each of the orthotic interfaces and the manipulator structure. These sensors measure force and torque in a local frame of reference (the body frame of the sensor), the orientation of which is dependent on the position of the manipulator. Body manipulator Jacobians that relate these body measures to resultant

joint torques are developed according to the approach in [73]. The derivation uses the Ad operator, defined as

$$\mathrm{Ad}(g)^{-1} = \begin{bmatrix} R^T & -R^T\,\hat{r} \\ 0 & R^T \end{bmatrix}, \text{ where } g = \begin{bmatrix} R & r \\ 0 & 1 \end{bmatrix}. \tag{3}$$

R and r are the 3×3 rotation matrix and 3×1 displacement vector from the 4×4 homogeneous transformation matrix g, respectively, defining the joint angle vector as follows:

$$\phi = \begin{bmatrix} \theta_1 & \theta_2 & -\theta_2 & -\theta_1 & \theta_3 & \theta_4 & \theta_5 & \theta_6 & \theta_7 & \theta_8 & \theta_9 \end{bmatrix} \tag{4}$$

and the home locations of the sensor body frame coordinates $g_{ua}(0)$, $g_{fa}(0)$, and $g_{hd}(0)$, allow the body twists, $\xi^\dagger$, to be defined as

$$\begin{aligned} \xi^\dagger_{ua,i} &= \mathrm{Ad}^{-1}\left(\left(\prod_{k=i}^{7} e^{\hat{\xi}_k \phi_k}\right)(g_{ua}(0))\right), && \text{where } i \in \{1:7\}, \\ \xi^\dagger_{fa,i} &= \mathrm{Ad}^{-1}\left(\left(\prod_{k=i}^{9} e^{\hat{\xi}_k \phi_k}\right)(g_{fa}(0))\right), && \text{where } i \in \{1:9\}, \\ \xi^\dagger_{hd,i} &= \mathrm{Ad}^{-1}\left(\left(\prod_{k=i}^{11} e^{\hat{\xi}_k \theta_{full,k}}\right)(g_{hd}(0))\right), && \text{where } i \in \{1:11\}. \end{aligned} \tag{5}$$

The body manipulator Jacobians are then given by

$$J^B_{st} = \begin{bmatrix} \xi^\dagger_i & \cdots & \xi^\dagger_{n-1} & \xi^\dagger_n \end{bmatrix}. \tag{6}$$

Thus, the body Jacobians can be established for any of BLUE SABINO's coordinate frames. The force sensor Jacobians are of immediate interest for control and are defined as

$$\begin{aligned} J^B_{ua,full} &= \begin{bmatrix} \xi^\dagger_{ua,1} & \cdots & \xi^\dagger_{ua,7} & 0_{(6x4)} \end{bmatrix}, \\ J^B_{fa,full} &= \begin{bmatrix} \xi^\dagger_{fa,1} & \cdots & \xi^\dagger_{fa,9} & 0_{(6x3)} \end{bmatrix}, \\ J^B_{hd,full} &= \begin{bmatrix} \xi^\dagger_{hd,1} & \cdots & \xi^\dagger_{hd,11} \end{bmatrix}. \end{aligned} \tag{7}$$

Since only nine DOFs are directly actuated, the Jacobians can be reduced in size from 6×11 to 6×9 matrices by defining a transform:

$$\theta = T\phi, \text{ where } T = \begin{bmatrix} 1 & 0 & & \\ 0 & 1 & & \\ 0 & -1 & 0_{4x7} & \\ -1 & 0 & & \\ & 0_{7x2} & & I_{7x7} \end{bmatrix}, \tag{8}$$

then applying it as follows:

$$\underbrace{J^B_{ua}}_{(6x9)} = \underbrace{J^B_{ua,full}}_{(6x11)} T, \quad \underbrace{J^B_{fa}}_{(6x9)} = \underbrace{J^B_{fa,full}}_{(6x11)} T, \quad \underbrace{J^B_{hd}}_{(6x9)} = \underbrace{J^B_{hd,full}}_{(6x11)} T. \tag{9}$$

2.4. Electromechanical Systems Design

BLUE SABINO's electromechanical system can be divided into five distinct parts. These include:

1. Operator Console: the primary interface for the experimenter/therapist. It includes a "Host PC" from which the control mode and therapy task can be configured. It also includes an emergency-stop button for the operator.

2. Main Electronics Box: a modular vertical server-rack structure that houses stationary system components, including power supplies, motor drivers, EtherCAT networking, and the real-time target PC, which serves as the primary processing unit for the system.
3. ATI Electronics Boxes: these mount to the base structure and contain interface boards that convert analog force/torque signals to digital EtherCAT signals. These components are external to the main electronics box because A/D conversion is performed near the transducers to minimize measurement noise.
4. Human Interfaces: these allow the user and the robot to interact. They include the HRAs, the two robotic exoskeleton arms, an emergency-stop switch for the user, a foot pedal switch that turns control throughput on/off, and a display for presenting a digital virtual environment.
5. Bio-Measurement System: this collects EMG and EEG signals. It includes an EEG skullcap, EMG sticker electrodes, and an amplification system for simultaneous real-time data collection.

2.4.1. System Components and Layout

The system uses actuators from Harmonic Drive (Beverly, MA, USA), dual-axis XE2 motor drivers from Copley Controls (Canton, MA, USA), six-axis force/torque (F/T) sensors from ATI Industrial Automation (Apex, NC, USA), a target PC from Speedgoat (Natick, MA, USA), an EtherCAT network block from Beckhoff (Savage, MN, USA), and safety hardware including a PNOZ s5 relay (Pilz, Canton, MI, USA), two emergency-stop buttons (Omron, Hoffman Estates, IL, USA), and a control-enable foot pedal switch (Linemaster, Woodstock, CT, USA) (Figure 8).

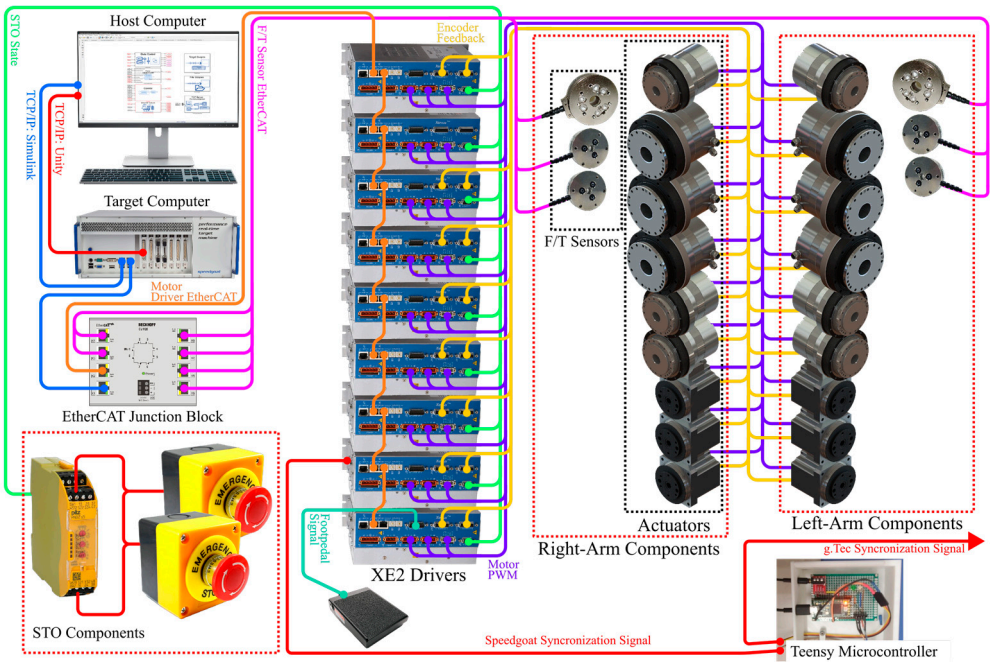

Figure 8. BLUE SABINO 18-DOF bilateral electromechanical system.

For system actuation, Harmonic Drive actuators were selected for their performance characteristics of high torque, backdrivability, and power-to-weight ratio. Harmonic Drive motors were also used in the EXO-UL8 but with differently sized motor and gear combinations, as the redesign for BLUE SABINO provided an opportunity to downsize motors and further reduce system weight.

System power requirements are largely driven by the expected current demands from the actuators during continuous and peak loading conditions, considering the weight of the

human and exoskeleton arms in an extended pose undergoing a typical peak acceleration against gravity for ADL movements [51].

Anticipated torque distributions per joint during ADL tasks are illustrated in Figure 9 for Joints 1–6. Elbow flexion, wrist extension, and radial deviation all require the ability to sustain gravitational loading in near-continuous conditions, while gravitational loading on the other joints is more position-dependent and transient.

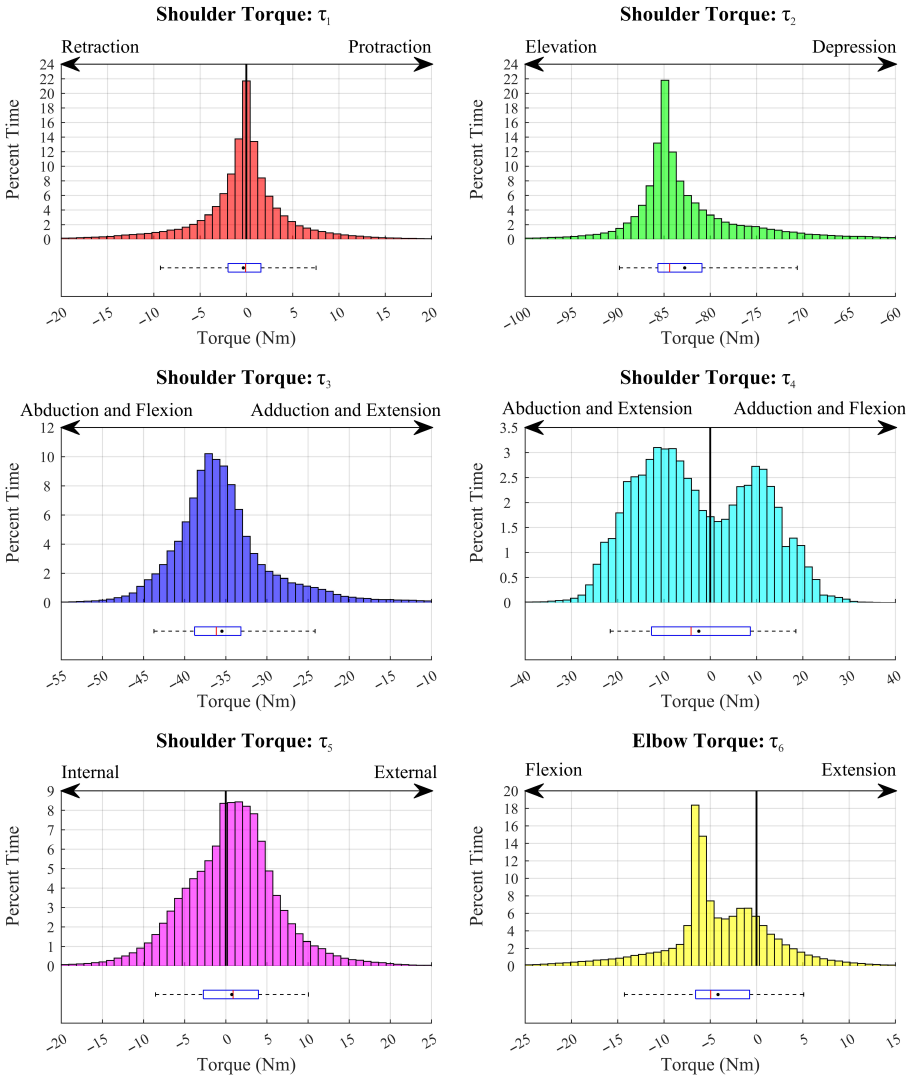

Figure 9. Anticipated torque distributions per joint during ADL tasks (adapted from [75]) used to select motors and gears for Joints 1–6.

Based on the anticipated ADL position and torque distributions, motors were selected to meet the desired continuous and peak load characteristics. Minimizing the number of unique motor/gear combinations, the BLUE SABINO arms (shoulder to wrist) use just three unique motors (Table 4).

Table 4. Harmonic Drive actuators and specifications.

Joints	Motor/Gear Combination	Cont. Torque (Nm)	Peak Torque (Nm)	Max Speed (RPM)
J_2, J_3, J_4	SHA25A/81:1	67	178	69.1
J_1, J_5, J_6	SHA20A/51:1	21	73	117.6
J_7, J_8, J_9	FHA11C/50:1	3	8.3	120

2.4.2. Power and Communication

The power and communication layout is illustrated in Figure 10. Standard 120-V wall power is distributed to the main electronics box, the g.tech bioamplifier, and the operator console. The main electronics box provides power through two power supply units (PSUs) to the F/T EtherCAT interface board and the Copley motor drivers, which in turn provide power to the F/T sensors and the nine system actuators. The EtherCAT interface board and the Copley motor drivers are connected to an EtherCAT junction box (Beckhoff CU1128) that communicates with the real-time controller compiled to and run on the target PC. A backup battery in the main electrical box provides Zener-diode-protected power to each of the motor encoders to maintain calibration data even when powered off or in transit [76].

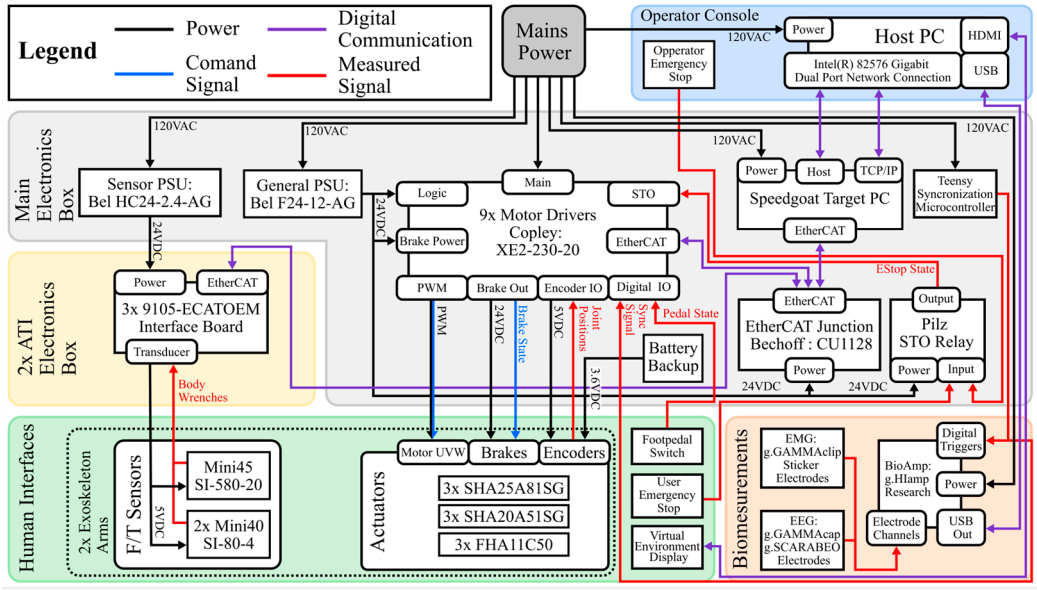

Figure 10. Layout for BLUE SABINO power and communication distribution.

2.5. System Safety

BLUE SABINO incorporates design for safety into mechanical, electrical, and software mechanisms. For critical risks, redundant systems are implemented. Safe operating procedures are established at startup and in transitions between operational modes to reduce the potential for unwanted behavior that could harm the subject, the operator, or the system. Both enable switches and emergency-stop (E-stop) switches are included for routine and emergency use, respectively. Other limits include physical hardstops and soft limits controlled in software by measures of force, position, and velocity.

2.5.1. System Startup Sequence

The operator performs a pre-operation check sequence on system startup, illustrated in Figure 11. First, wiring harnesses and mechanical HRAs are inspected to ensure all wires are contained within their protective covers and that the HRAs are rigidly secured to each F/T sensor without additional points of contact internal or external to the robot. After the initial inspection, the power is turned on, the status of LEDs on the driver and sensors is checked, and the robot's overall status is checked via the target PC's monitor. If status indicators show proper function, the E-stop is inspected to verify it is in the closed (unpressed) position, and the robot is manually backdriven to confirm the brakes have disengaged. If the system passes each of the four checkpoints, the operator may proceed to the desired control mode for system use.

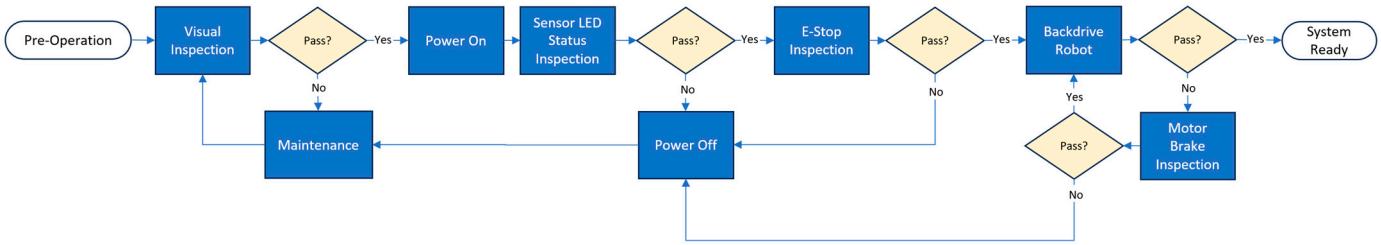

Figure 11. BLUE SABINO system startup sequence.

2.5.2. Regular Operation "Enable" vs. "E-Stop" Switches

The enable switch is a foot-operated pedal that determines when force/torque command signals are sent from the ATI sensors to the controller. When unpressed, interaction-force signal transmission to the admittance control ceases and the inner-loop position control holds the robot in its current position. When pressed, the gain on force signals is gradually ramped up from zero to one to minimize instability. The ramp-up time allows the subject to recognize that the robot is no longer stationary and to reinitiate self-supported control via HRA interaction forces. The foot pedal remains depressed during system use and is released at the end of a session to return the controller to a hold-current-position mode.

Two system E-stop switches (A22E-M-02B, Omron) are located near the therapist and patient. When either E-stop is pressed, control signals are turned off and brakes are initiated. Tests were conducted to verify the functionality and responsiveness of the E-stop system. Estimates indicate that safety stops can be initiated within 1.5 s, which includes the delay from humans engaging the E-stop. Once pressed, the delays added by the hardware components are relatively small (15–20 ms from the Pilz relay; minimum 2.5 ms from the Copley driver), according to the manufacturers' documentation. The minimum brake onset time from hardware is, therefore, between 17.5 and 22.5 ms. To reduce the delay caused by human reaction and not rely solely on the operator to initiate the safety response, automated hardware and software limits are in place to prevent overextension and high forces from being exerted on the arm.

2.5.3. Hardware and Software Safety System

During normal operation, the target computer runs control software, which monitors the force, torque, position, velocity, and status of the electromechanical hardware listed in Figure 12 at a rate of 1000 Hz (i.e., every millisecond). If a system component reaches a limit, the control program can detect overage within one timestep (1 ms) and initiate a system control fault in the next timestep such that detection and communication of faults in software occur within 2–3 ms. Possible software-level faults include (1) out-of-range force/torque, (2) out-of-range joint position/velocity, (3) loss of network communication, (4) non-operational motor status, including faults detected at the motor driver level (e.g., wiring short or break detection), (5) force-sensor status (e.g., disconnect or overload detected), and (6) active E-stop status.

The software safety system is divided into value limits and state monitoring. Limit enforcement prevents out-of-range signals from impacting control. For example, if an orthosis makes stiff contact with an external hard surface, a large reaction force will result on the force sensor; the force and torque limits also limit the response of the admittance control, helping to ensure stable, safe control. State monitoring protects against more severe issues. A Stateflow program is configured to switch the controller to safe mode if a driver or sensor reports a fault, if communication with devices on the EtherCAT network is interrupted, or if any measured position, velocity, or force/torque state exceeds a safe-limit threshold.

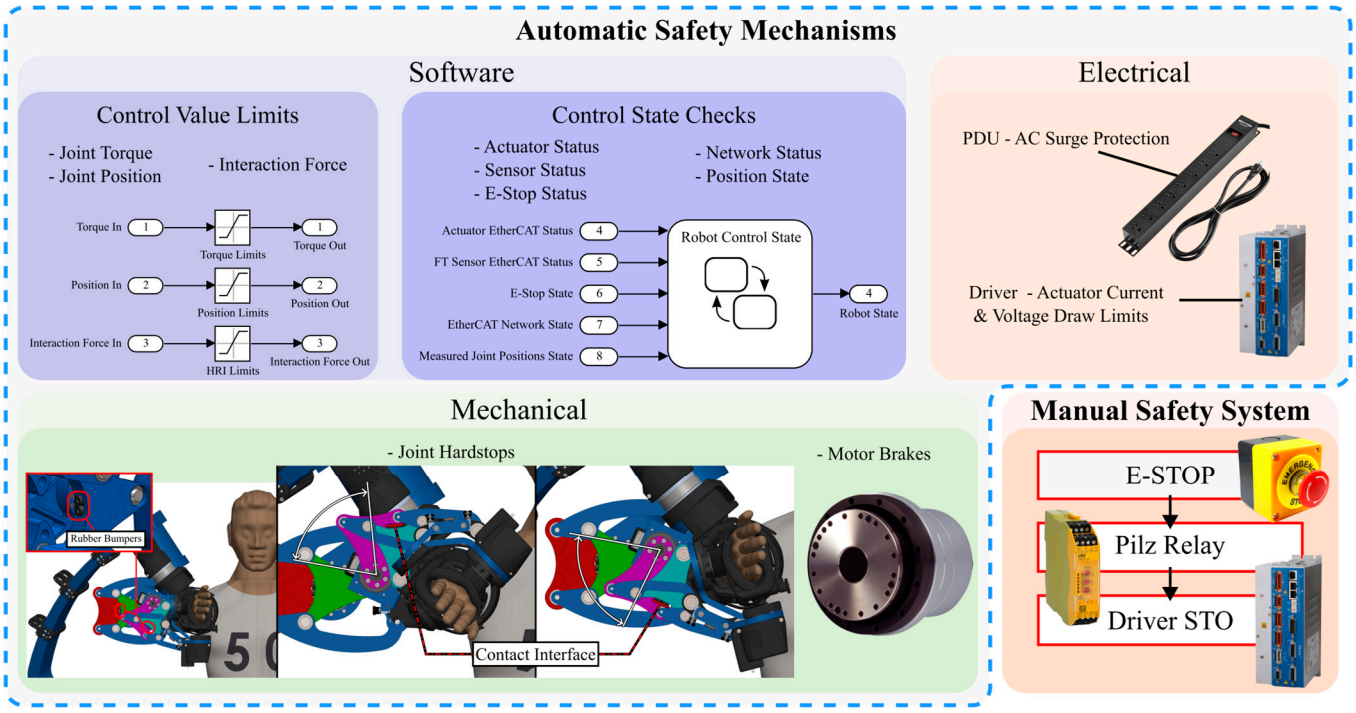

Figure 12. Automatic and manual safety systems are integrated into the BLUE SABINO control architecture. Automatic systems provide fast and dependable safety responses, while the manual system allows the user and operator to stop the system manually, if needed.

Startech PDUs provide electrical protection and limit system-level total current draw to 15 Amps. The XE2 motor drivers monitor for various electrical faults at the hardware level, including over/under current and voltage, drive over-temperature, short circuits, or encoder battery failure, and initiate a drive fault when any limit is exceeded. Drive faults are communicated to the target via the EtherCAT status, but drivers do not wait for the target to respond to protect the user and hardware.

Mechanical hardstops function as an ultimate limit on range of motion and as a fallback if all other software/electronic limits were to fail. Brakes are included in all SHA actuated joints, and while they are not intended to be used for regular stopping due to the potential for wear, they can assist in bringing the device to a halt in an emergency.

Finally, a manual safety system is implemented via operator and user E-stop switches monitored by a Pilz relay. If any E-stop switch is pressed, the relay tells each driver's Safe Torque Off (STO) circuit to trigger brakes and halt motion.

2.5.4. Soft and Safe Range of Motion Limits

Software position constraints are enforced using soft and safe limits. If soft limits are exceeded but safe limits are not, the control attempts to correct the user's position using a combination of limits on control states and model-based corrective joint torques. This approach allows the user to continue operating the device without interruption so long as no safe limit is surpassed. If any of the safe limits are exceeded, the state monitoring safety system sets the robot to safe mode, which turns off control throughput and enables the brakes on all joints that include them. The device can only be set to run mode again by first setting the robot to setup mode to the release brakes and manually backdriving the joints into the safe range. Both the soft and safe limits are adjustable, which allows the robot's ROM to be customized for users with a limited range of motion.

2.6. Controller Design

This section presents the nine-DOF right-control design for BLUE SABINO's low-interaction force-free motion admittance control mode. Just the right-side arm's control

is discussed for the sake of brevity. The control for the left-side arm is identical to that of the right side, except that where Jacobians or forward kinematic transformations are used, mirror versions are applied instead.

2.6.1. Control Overview

BLUE SABINO's control software had been implemented using MATLAB's Simulink (R2019a) graphical programming environment [77]. The control program is developed on a host PC for a real-time target (Speedgoat) deployment. Simulink's real-time toolbox provides I/O interface blocks for network communication with devices on an EtherCAT network whose structure is configured using TwinCAT software (TwinCAT 3.1 Builder 4024).

The target acts as the main EtherCAT device, coordinating and acquiring data from subordinate devices on the network. Control applications are automatically compiled to C-code and downloaded to the target PC. TCP-IP communication between the host and target allows control states and parameters to be accessed and changed by the host PC for hardware-in-the-loop control development.

BLUE SABINO's low-interaction-force controller is composed of a joint-level admittance control loop, a trajectory control loop, a model-based compensation control loop that includes compensation for friction and gravity, and a control safety system (Figure 13). User-applied forces are mapped to joint torques via manipulator Jacobians [73]. The admittance control loop sets the target position and velocity for the trajectory control loop, which computes joint torque commands that are summed with model-based compensation for joint-level friction and gravity torques before being sent to driver-level control.

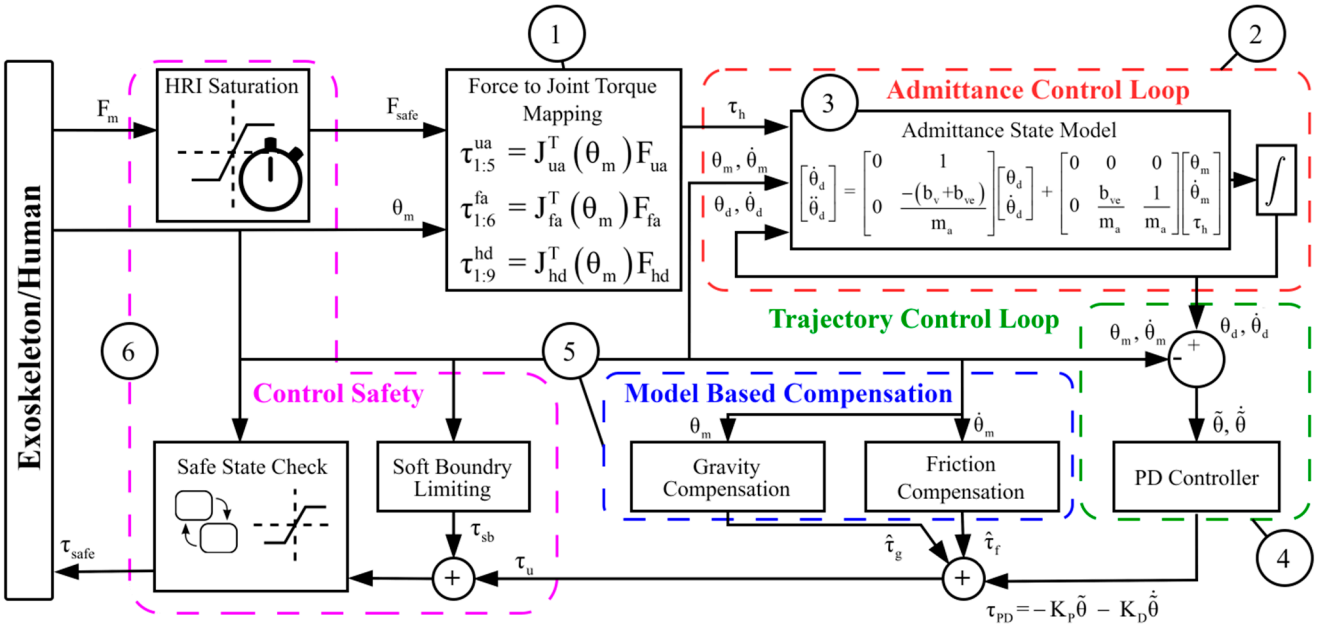

Figure 13. Admittance control scheme for BLUE SABINO. (1) User-applied forces are converted to human joint torques, τ_h. (2) The admittance-control loop uses τ_h to set target states. (3) Joint-level admittance models, including inertia, m_a velocity damping, b_v, and velocity error damping, b_{ve}, to set the inner-loop trajectory targets. (4) The trajectory-control loop computes proportional-derivative (PD) admittance-state tracking control torques, τ_{PD}. (5) Model-based compensation for friction and gravity is added to the control torque, resulting in τ_u. (6) Safety limits are enforced on human–robot interaction forces and joint range of motion. Control-state monitoring disables control torque throughput if any safety limits are exceeded or network/device faults are detected.

2.6.2. Combined Human and Robot Dynamics Control Law

The dynamics of BLUE SABINO can be described as follows:

$$M(\theta)\,\ddot{\theta} + C\left(\theta,\,\dot{\theta}\,\right)\dot{\theta} + \tau_g + \tau_f = \tau_u + \tau_h, \tag{10}$$

where θ, $\dot{\theta}$, and $\ddot{\theta}$ are joint position, velocity, and acceleration, respectively. M is the manipulator inertia matrix, **C** is the Coriolis matrix, τ_f is friction torque, τ_g is gravity torque, τ_u is the control input vector, and τ_h is the human input torque.

The control input includes model-based compensation for friction and gravity as well as the proportional-derivative (PD) tracking of the desired trajectory set by the admittance model. Compared to gravity and friction, inertial torques are relatively small for typical human movement speeds [59] and thus are not included in the control law, similar to [78,79]. The control law is defined as

$$\tau_u = -K_P\,\widetilde{\theta} - \,K_D\,\dot{\widetilde{\theta}} + \hat{\tau}_f + \hat{\tau}_g, \tag{11}$$

where K_P and K_D are positive-definite proportional and derivative gain matrices. Terms $\widetilde{\theta} = \theta_m - \theta_d$ and $\dot{\widetilde{\theta}} = \dot{\theta}_m - \,\dot{\theta}_d$ are joint position and velocity error vectors, respectively, with the *m* and *d* subscripts indicating the measured and desired states. Joint friction, $\hat{\tau}_f$, is estimated by experimentally identified sigmoid models that capture coulombic and viscous effects for each motor [80]. Gravity, $\hat{\tau}_g$, is estimated using manipulator kinematics and CAD modeling.

2.6.3. Mapping Human–Applied Forces/Torques to Joint Torques

Input forces are measured via three force sensors located at the upper arm, the forearm, and the hand HRAs. The sensors measure interaction forces and torques between the human and the robot in their respective body frames. These signals are mapped to equivalent joint-level torques via body manipulator Jacobians. The resulting torque vectors are, therefore, defined as follows:

$$\begin{aligned} \tau_{1:5}^{ua} &= \left(J_{ua}^{B}\right)^{T} F_{ua}, \\ \tau_{1:6}^{fa} &= \left(J_{fa}^{B}\right)^{T} F_{fa}, \\ \tau_{1:9}^{hd} &= \left(J_{hd}^{B}\right)^{T} F_{hd}. \end{aligned} \tag{12}$$

where J_{ua}^{B}, J_{fa}^{B}, and, J_{hd}^{B} are the body Jacobians defined in Equation (7). The mapped joint torques are combined to compute overall human applied joint torque as

$$\tau_h = \begin{bmatrix} \tau_1^{ua} & + & \tau_1^{fa} & + & \tau_1^{hd} \\ \tau_2^{ua} & + & \tau_2^{fa} & + & \tau_2^{hd} \\ \tau_3^{ua} & + & \tau_3^{fa} & + & \tau_3^{hd} \\ \tau_4^{ua} & + & \tau_4^{fa} & + & \tau_4^{hd} \\ \tau_5^{ua} & + & \tau_5^{fa} & + & \tau_5^{hd} \\ & & \tau_6^{fa} & + & \tau_6^{hd} \\ & & & & \tau_7^{hd} \\ & & & & \tau_8^{hd} \\ & & & & \tau_9^{hd} \end{bmatrix}. \tag{13}$$

2.6.4. Admittance Force Control

The joint-level admittance model takes human joint torques (mapped from F/T sensors at the HRAs) and outputs a desired trajectory to the inner-loop controller. The model

includes inertia, m_a, velocity damping, b_v and velocity error damping, b_{ve}. The admittance model for an individual joint has the form

$$\begin{bmatrix} \dot{\theta}_d \\ \ddot{\theta}_d \end{bmatrix} = \begin{bmatrix} 0 & 1 \\ 0 & \frac{-(b_v+b_{ve})}{m_a} \end{bmatrix} \begin{bmatrix} \theta_d \\ \dot{\theta}_d \end{bmatrix} + \begin{bmatrix} 0 & 0 & 0 \\ 0 & \frac{b_{ve}}{m_a} & \frac{1}{m_a} \end{bmatrix} \begin{bmatrix} \theta_m \\ \dot{\theta}_m \\ \tau_h \end{bmatrix}. \tag{14}$$

The joint-level models can be arranged into a state–space matrix form that accommodates all nine joints as follows:

$$\underbrace{\begin{bmatrix} \dot{\theta}_d \\ \ddot{\theta}_d \end{bmatrix}}_{\dot{x}_{18\times1}} = \underbrace{\begin{bmatrix} 0_{9\times9} & I_{9\times9} \\ 0_{9\times9} & I_{9\times9}\begin{bmatrix} \frac{-(b_{v,1}+b_{ve,1})}{m_{a,1}} & & \\ & \vdots & \\ & & \frac{-(b_{v,9}+b_{ve,9})}{m_{a,9}} \end{bmatrix} \end{bmatrix}}_{A_{18\times18}} \underbrace{\begin{bmatrix} \theta_d \\ \dot{\theta}_d \end{bmatrix}}_{x_{18\times1}} + \underbrace{\begin{bmatrix} 0_{9\times27} \\ 0_{9\times9} \quad I_{9\times9}\begin{bmatrix} \frac{b_{ve,1}}{m_{a,1}} & & \\ & \vdots & \\ & & \frac{b_{ve,9}}{m_{a,9}} \end{bmatrix} \quad I_{9\times9}\begin{bmatrix} \frac{1}{m_{a,1}} & & \\ & \vdots & \\ & & \frac{1}{m_{a,9}} \end{bmatrix} \end{bmatrix}}_{B_{18\times27}} \underbrace{\begin{bmatrix} \theta_m \\ \dot{\theta}_m \\ \tau_h \end{bmatrix}}_{u_{18\times1}}. \tag{15}$$

The choice of admittance parameters determines the force "feel" of the interactive force control. Most admittance/impedance controllers include heuristically tuned inertial and resistive elements that store and dissipate energy so that the controlled system can sufficiently reject unwanted disturbances [81,82]. Capacitive elements are not typically used for free motion but are sometimes employed to guide the user's motion [83,84]. Generally, the lower the inertia and resistive parameters set, the more responsive the control will be to input forces. However, in most cases, inertia and damping are required to achieve stable force interaction. An investigation of different combinations of these parameters was undertaken in [85]. In the remainder of this paper, we use a hybrid of the velocity-damping (VD) and velocity-error-damping (VED) modes. VED was previously determined to provide the best overall performance in terms of required user effort and the vibration rejection of the considered modes. A small level of constant velocity damping is applied here for its stabilizing effect, which was found to aid the user in bringing the device to a stop when desired. The value used is small to maintain the low level of work required by the user to move. The selected admittance parameters for this configuration are provided in Table 5.

Table 5. Selected velocity-error-damping admittance control parameters.

Term	Unit	Joint								
		J_1 *	J_2 *	J_3	J_4	J_5	J_6	J_7	J_8	J_9
m_a	$kg \cdot m$	0.6	0.6	0.5	0.5	0.3	0.1	0.01	0.01	0.01
b_v	$kg \cdot m/s$	0.5	0.5	0.5	0.5	0.3	0.3	0.05	0.05	0.05
b_{ve}	$kg \cdot m/s$	15	15	15	15	9	9	3	3	3

* This tuning has only been tested on $J_{3–9}$ at time of writing. Initial parameters for $J_{1–2}$ are informed by knowledge of acceptable tuning for $J_{3–9}$.

2.6.5. Inner-Loop PD Control

Selecting appropriate inner-loop PD gains is critical to achieving accurate state tracking with the exoskeleton. BLUE SABINO's inner-loop PD gains were tuned heuristically in a hardware-in-the-loop configuration such that each joint accurately tracks sinusoid command inputs spanning the bandwidth of healthy human upper-limb motion (0.1–3 Hz for the shoulder joints, 0.1–5 Hz for the elbow and wrist joints) [59]. Control gains are selected to achieve high position- and velocity-state accuracy, as proposed in [86,87], which is ad-

vantageous for achieving high force-rendering accuracy in the outer loop. The heuristically selected diagonal gain matrices are

$$\begin{aligned} K_P &= \mathrm{diag}([\ K_{P2}\ \ K_{P1}\ \ K_{P1}\ \ K_{P1}\ \ K_{P2}\ \ K_{P2}\ \ K_{P3}\ \ K_{P3}\ \ K_{P3}\ ])\ \left(\tfrac{N\times m}{rad}\right), \\ K_D &= \mathrm{diag}([\ K_{D2}\ \ K_{D1}\ \ K_{D1}\ \ K_{D1}\ \ K_{D2}\ \ K_{D2}\ \ K_{D3}\ \ K_{D3}\ \ K_{D3}\ ])\ \left(\tfrac{N\times m\times s}{rad}\right), \end{aligned} \tag{16}$$

where values selected per actuator are given in Table 6.

Table 6. Proportional and derivative gains for admittance control gain selection.

Motor	Term	Value (Nm/rad)	Term	Value (Nms/rad)
SHA25A	K_{P1}	4000	K_{D1}	200
SHA20A	K_{P2}	3000	K_{D2}	40
FHA11C	K_{P3}	320	K_{D3}	1

It should be noted that this selection of gains is only appropriate for admittance force control where the position-state targets change continuously with small time intervals between updating targets. In position-tracking mode, these gains can result in large control torques if there is a significant position error (e.g., the command position is distant from the robot's current position) or if updates are infrequent (e.g., a latency in communication of the target position by a game creates a discontinuous state target).

2.6.6. Friction Compensation

Joint friction in BLUE SABINO's structure primarily results from the Harmonic Drive actuators' gearing. Friction in Harmonic Drive actuators is often described as a combination of Coulomb and viscous friction and additional nonlinear effects, including Stribeck effects and motor position dependencies [88]. While identifying perfect compensation for friction effects in the motors is notoriously tricky, we only aim to achieve increased control bandwidth here. Therefore, simplified models of friction-capturing dominant effects are deemed acceptable.

To model the friction within each motor/gear pair, friction–velocity maps were experimentally estimated following the procedure outlined in [89]. Further details on the friction modeling and compensation process can be found in Appendix B.

2.6.7. Gravity Compensation

Given the forward kinematics functions of the link center-of-mass points, the joint torques due to the external gravitational force on BLUE SABINO's rigid links are computed via the potential energy as in [74]. CAD model estimates of the mass of each link, m_i, and the forward kinematic mappings $p_{COM,i}(\theta)$, to center-of-mass (COM) as functions of the joint position vector θ are used to derive the overall potential energy of the serial chain. Defining gravitational acceleration in the negative y-direction, the overall potential energy is

$$P_{grav} = \sum_{i=1}^{N_{links}} m_i g^T p_{COM,i}(\theta). \tag{17}$$

Gravitational torque is computed via partial differentiation with respect to the joint position as

$$\tau_g = \frac{\partial P_{grav}}{\partial \theta}, \tag{18}$$

where τ_g is the vector of torques about the actuated joints due to gravity.

2.6.8. Soft Limits: Joint Range of Motion and Boundary Torques

A soft boundary torque is applied at the joint level to any joints exceeding positive or negative limits. The boundary torque is computed according to

$$\tau_{sb} = \begin{cases} -\left(k_{sb}|\theta_{sb,Max} - \theta|^2 - d_{sb}\ \dot{\theta}\right)\Big) & \text{if} \quad \theta_i > \theta_{sbMax,i} \\ \left(k_{sb}|\theta_{sb,Min} - \theta|^2 - d_{sb}\ \dot{\theta}\right) & \text{if} \quad \theta_i < \theta_{sbMin,i} \\ 0 & \text{otherwise} \end{cases} \tag{19}$$

where k_{sb} and d_{sb} are vectors of virtual-boundary torsional spring constants and damping coefficients corresponding to each actuated joint and $\theta_{sb,Max}$ and $\theta_{sb,Min}$ are the selected maximum and minimum soft range of motion limits. The parameter values are defined per actuator type as

$$\begin{aligned} k_{sb} &= \text{diag}(\begin{bmatrix} k_{sb2} & k_{sb1} & k_{sb1} & k_{sb1} & k_{sb2} & k_{sb2} & k_{sb3} & k_{sb3} & k_{sb3} \end{bmatrix}) \left(\tfrac{N\times m}{rad}\right), \\ d_{sb} &= \text{diag}(\begin{bmatrix} d_{sb2} & d_{sb1} & d_{sb1} & d_{sb1} & d_{sb2} & d_{sb2} & d_{sb3} & d_{sb3} & d_{sb3} \end{bmatrix}) \left(\tfrac{N\times m\times s}{rad}\right), \end{aligned} \tag{20}$$

with values defined in Table 7.

Table 7. Selected soft boundary spring and damping coefficients for free-motion admittance force control.

Motor	Term	Value (Nm/rad)	Term	Value (Nms/rad)
SHA25A	k_{sb1}	4000	d_{sb1}	500
SHA20A	k_{sb2}	3000	d_{sb2}	300
FHA11C	k_{sb3}	100	d_{sb3}	10

The spring force magnitude is squared with respect to the magnitude of boundary displacement, ensuring that the rate of applied corrective torque increases along with displacement. The damping term reduces kinetic energy when a joint runs into a stop, which helps prevent underdamped oscillation when a joint bounces off the virtual spring. Instead, adequately tuned damping results in a joint smoothly coming to a halt after impacting the virtual boundary.

Since the admittance controller operates by moving a joint state target in response to interaction force, the admittance target positions must be bounded within the soft limits of the range of motion. Otherwise, the admittance targets can drift away from the robot's position when a stop is reached, creating excessive control torques and the potential for unexpected motion. Therefore, the integration function for the admittance control model is also bounded by the soft position limits so that the admittance target state can only assist in driving the user back into the acceptable range of motion.

2.7. Biosignal Acquisition System Selection

Significant design efforts throughout development were devoted to ensuring compatibility with acquiring electromyography (EMG) and electroencephalography (EEG) biosignals. The analysis of electrophysiological signals complements the insights drawn from kinematics and kinetics, offering a holistic picture of movement even before its occurrence. However, several critical considerations must be addressed when acquiring biosignals with actuated exoskeleton devices like BLUE SABINO to maximize signal-to-noise ratio (SNR) in a potentially noisy environment and ensure proper synchronization between subsystems.

The inherently low SNR of these signals, particularly in EEG, influences the selection of the biosignal amplifier, electrode types, and placement, as well as experimental paradigms [90] and processing pipelines [91]. Due to the proximity to multiple active

motors around the participant, the system uses active electrodes. These electrodes digitize the signal directly on the sensors (located on the scalp for EEG and on the skin for EMG), enhancing signal robustness and reducing vulnerability to noise as the signal is transmitted the rest of the way from the body to the amplifier. The SNR can be further enhanced if low electrode impedances are maintained during experiments, which is essential for establishing a good "connection" between the acquisition system and the participant. Furthermore, the location of the biosignal amplifier, situated directly behind the participant's chair, was chosen to prevent EEG/EMG wires from interfering with motor power lines. As an additional layer of isolation, biosignal acquisition is conducted on a dedicated computer, separate from the robot's real-time control system.

The high time resolution of EEG and EMG signals renders these measurements capable of informing us about physiological processes that evolve rapidly over time [92,93]. These processes are commonly studied by analyzing oscillatory activity and its evolution over repetitions of the same task. Therefore, proper synchronization with the robot is paramount in interpreting these signals in conjunction with kinematic and kinetic information. Synchronization between systems is typically achieved by exchanging electrical pulses between devices. These pulses denote moments of interest in repetitions of a task.

Other measures to minimize noise should be integrated into experiment design, including the optimization of sensor placement and ensuring low impedances. Employing a clear, simple, and repeatable task facilitates the differentiation of electrical biological activity related to the task from noise and other activity (muscle or brain activity not related to the task). Despite these precautions, residual noise in the signal persists, necessitating further minimization during the various stages of signal preprocessing applied to these signals. Common factors that contribute to biosignal acquisition quality are further discussed in Appendix C.

2.7.1. Biosignal System Specifications

The specifications for a biosignal recording system in the context of this project were the following:

- A multichannel system capable of synchronously recording different types of biosignals: EEG (unipolar signals referenced to a common location), EOG and EMG (bipolar signals).
- Compatibility with active electrodes to minimize the incidence of electromagnetic noise.
- Flexible EEG montages, allowing for layout customization to address various research questions. The minimum number of electrodes should encompass 19 locations as per the 10–20 standard.
- Multiple digital inputs to facilitate synchronization with other devices in different experimental protocols.

2.7.2. Component Selection and Layout

The gtec g.HIamp RESEARCH multi-channel amplifier (g.tec, Schiedlberg, Austria) was selected for biosignal acquisition. This device offers wide input sensitivity, enabling the recording of EEG, ECG, EMG, EOG and others without saturation. It supports the simultaneous acquisition of up to 80 channels (expandable to 256) with flexible montages. It also allows for communication with other devices for the synchronization of simultaneous data acquisition using 16 digital-input trigger channels. The amplifier is paired with g.Scarabeo active electrodes for EEG measurement and disposable snap electrodes for EMG.

2.8. System Integration and Validation Methods

During system development, two-DOF, five-DOF, and seven-DOF configurations of the arm were constructed and evaluated. The two-DOF configuration (Figure 14A) supported movements of elbow flexion/extension and forearm pronation/supination. The five-DOF configuration (Figure 14B) added movements of shoulder flexion/extension,

abduction/adduction, and internal/external rotation. The seven-DOF configuration further added wrist flexion/extension and wrist radial/ulnar deviation. The later addition of PRISM will expand each arm to nine DOFs for an 18-DOF configuration (Figure 14C). In each configuration, robotic cable guides from IGUS (Tri-flex TRL 30, TRE30, and TRL60) protect actuator and sensor cables from excessive bending, tension, and torsion over the length of the arm, from the stationary base modules to the hand.

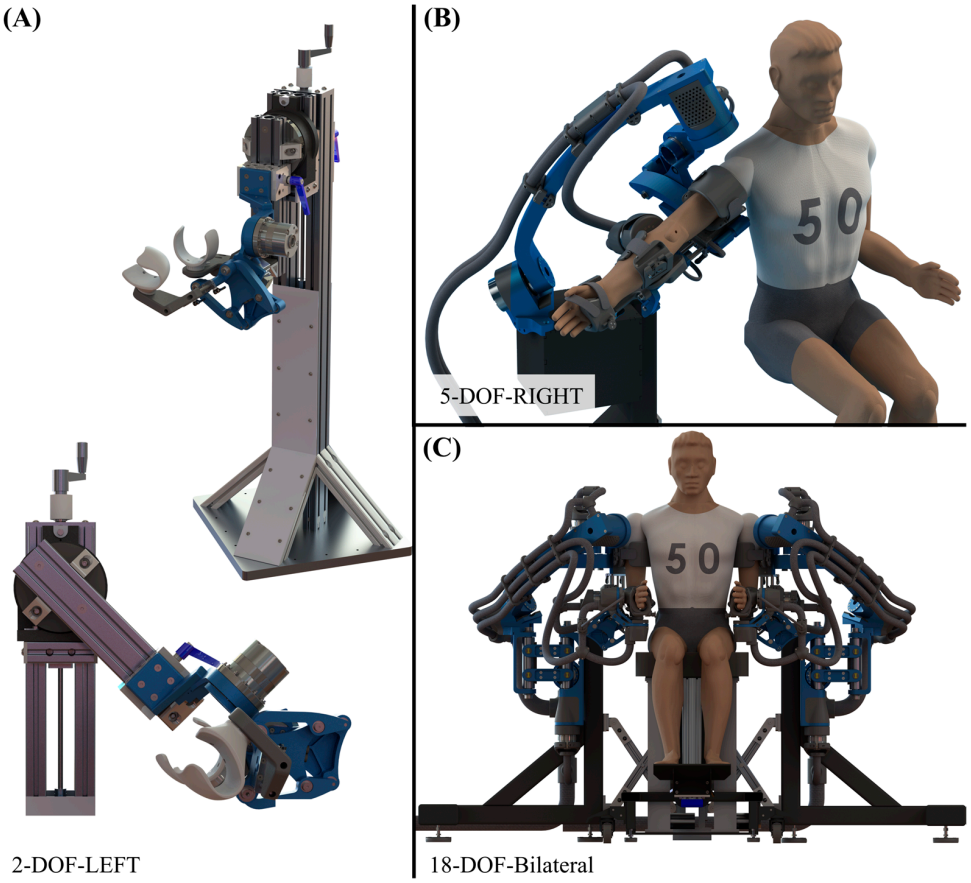

Figure 14. System integration phases: (**A**) An initial two-DOF version supported elbow flexion/extension and forearm pronosupination. (**B**) The five-DOF version added three orthogonal joints to the shoulder. (**C**) The future 18-DOF bilateral version adds two joints at the wrist and two joints at the base of the shoulder.

The system operation was validated first through (1) kinematic simulation, and then through systematic tests to measure aspects of exoskeleton system performance, including (2) spatial measurement validation; (3) anthropometric validation (i.e., size adjustability, and range of motion); (4) safety validation (i.e., hardware and software systems and limits); (5) controller validation (i.e., accuracy and repeatability); and (6) biosignal acquisition validation (i.e., quality of simultaneous biosignal measurements).

2.8.1. Kinematic Validation Methods

A MATLAB script was developed that generates kinematics, Jacobians, and gravity models tailored to BLUE SABINO. These models were exported as Simulink function blocks for integration with the real-time control model. They were also exported as MATLAB functions and C-code for utilization within the virtual game environment.

Additionally, an animator was created to play back trajectories and visualize the robot in various joint configurations. The animator displays STL representations of the robot links, force sensors, and a human user within a MATLAB 3D plot environment.

2.8.2. Spatial Measurement Validation Methods

The accuracy of BLUE SABINO's kinematic measurements is critical for evaluating the precise motion of users. Joint position measurements are collected via Nikon encoders located in each Harmonic Drive actuator, which achieve an accuracy of ±0.003 degrees. However, deflection in the robot's links, bearings, or post-gearing is not accounted for in this measurement. For this reason, BLUE SABINO's design has been carefully developed to maximize structural rigidity and to also achieve low link weights. The balance of these two design factors is critical to the performance of any upper-limb exoskeleton. Since our FEA/FEM models cannot accurately account for all of the sources of deflection in the exoskeleton, we sought to establish an empirical measure of its position measurement accuracy using the forward kinematics and the encoder measurements. A motion-capture setup used Flex 13 cameras and Motive software (OptiTrack, Corvallis, OR, USA) to track reflective markers on the robot (Figure 15—top). A special end effector was placed at the wrist with markers such that the tracked rigid body was located at the anatomical wrist center. An inverse kinematic solver was established to define a set of shapes, including a "UofI-I", a "Circle", a "Cube", and a "Star" (Figure 15—bottom).

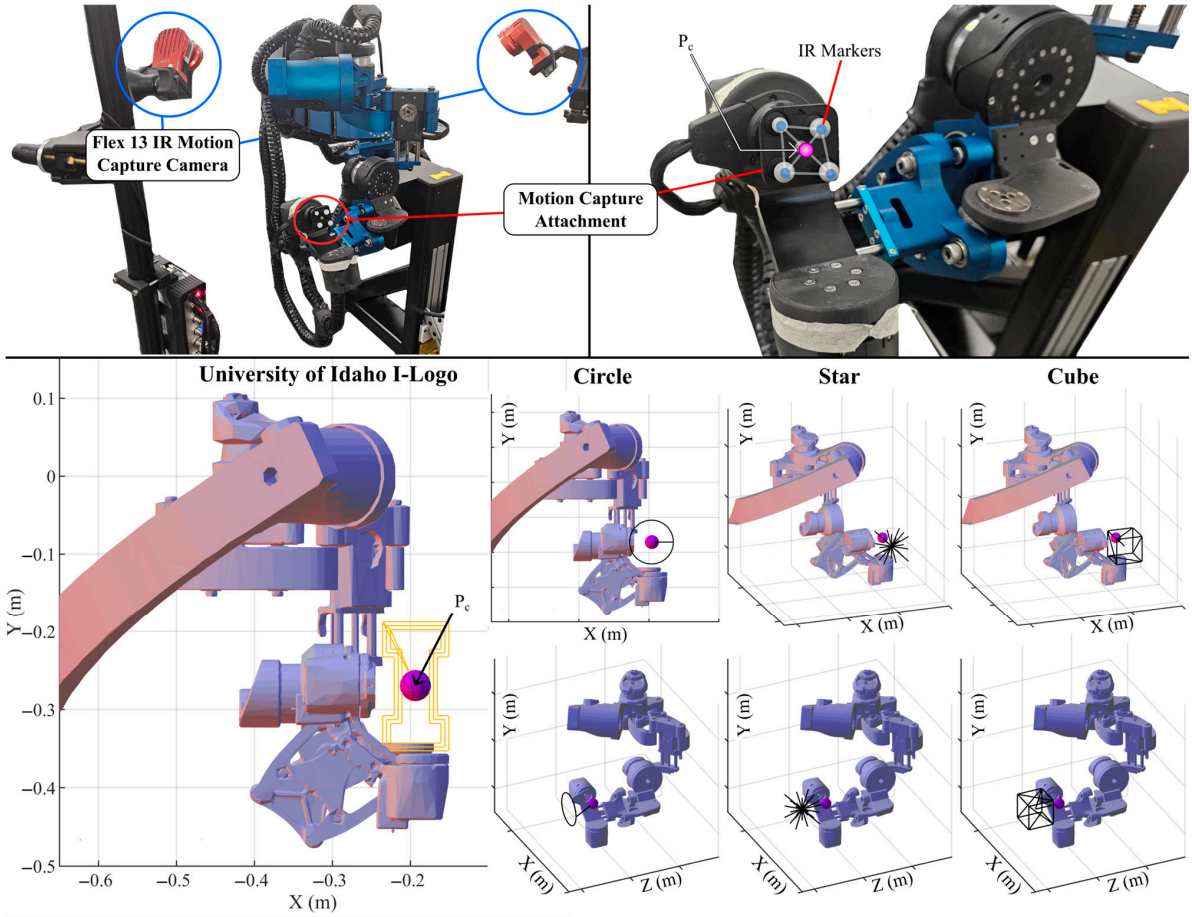

Figure 15. Motion-capture setup and predefined robot trajectories. (**Top**) The motion of the right-side seven-DOF BLUE SABINO arm is recorded simultaneously using a set of five Flex 13 IR motion-capture cameras. The cameras track the spatial positions of retroreflective markers on a special wrist-mounted motion-capture end-effector part. Optitrack software fits a rigid body in real time to the markerset to define the position and orientation of P_c. (**Bottom**) Three-dimensional views of the upper-arm section of BLUE SABINO (with orthosis components removed for clarity) are shown in relation to the predefined trajectories traced out for motion-capture experiments. The path is traced by the end-effector point P_c, whose initial position is indicated by the purple sphere and represents the centroid of the rigid body tracked by the motion-capture system.

The robot was placed in a trajectory tracing mode (simple PD control with the same K_p and K_d values used for admittance control), and BLUE SABINO's right seven-DOF arm was commanded to trace out predefined shapes. Motion capture and joint kinematics were recorded simultaneously for five repetitions of each motion to establish measures of error between the motion capture and forward kinematic mapped-encoder measurements, as well as estimates of inter-repetition variance.

2.8.3. Anthropometric Validation Methods

Anthropometric validation includes confirming the ranges of adjustability and the ranges of motion of each arm joint. The adjustments for shoulder alignment, segment length, and segment width were measured at the minimum and maximum limits of their adjustable ranges and are reported in Section 3.2. The anthropometric size adjustments include floor-to-seat height, exoskeleton shoulder width, upper-arm length, forearm length, upper-arm width, forearm width, and hand width.

The range of motion allowed by the design is compared between joints of the arm and exoskeleton following common conventions for joint movement axes, and it was measured in CAD. However, for the shoulder, it should be noted that while the range of shoulder internal/external rotation remains a consistent value, the orientation of the range moves relative to the user depending on the orientation of the previous two shoulder joints (J_3 and J_4) that both introduce combinations of shoulder flexion/extension and abduction/adduction. As described in [64], the election of J_3 and J_4 axial placements shifts the robot singularity to the edge of the workspace; it centers the shoulder range of motion in a region of high mechanical manipulability (i.e., isotropy close to 1). This arrangement is also desirable in that it shifts the shoulder range of motion for J_5 during the movement of J_3 and J_4 in an anthropomorphically desirable manner. For example, when the shoulder is abducted, the J_5 range of motion is shifted toward greater external rotation, similar to what occurs in the biological shoulder.

2.8.4. Safety Validation Methods

The joint hardstops are designed to reliably limit the robot's motion in the event that all other safety mechanisms fail. The stops have been designed to withstand maximum actuator torques and impacts under anticipated conditions. They have been tested under normal use by temporarily disabling the soft and safe stop limits and placing the robot in free-motion admittance control mode, with an external operator intentionally driving each joint one at a time into collision with the stops to simulate realistic use cases. The device was then inspected for any permanent deflection or structural failure and observed to have sustained no damage.

The safe limits were similarly evaluated by disabling the soft stops and setting the control to free-motion force mode. The operator then intentionally drives each joint past the safe stop limits and observes that the control state is correctly changed to safe mode in acceptable time.

To evaluate the soft stop limits, the limit positions are set temporarily to the midpoint of the joint range of motion, and the external operator again drives the joints into the limits at three different speeds. This process was repeated, with the joint boundary model parameters being adjusted until the maximal overshoot was under three degrees and the interaction with the soft boundary was sufficiently damped to produce no buzzing and sufficiently stiff so as to correct the user's position after the driving force was removed in under 0.5 s.

2.8.5. Controller Validation Methods

To achieve the force-tracking bandwidth necessary for responsive, low-interaction force-free motion admittance control, the inner-loop control is tuned to accurately track command inputs spanning the bandwidth of healthy human upper-limb motion (0.1 to 3 Hz for the shoulder joints 0.1 to 5 Hz for the elbow and wrist joints) [59]. This ensures that

high force-rendering accuracy can be achieved on the outer loop [86,87]. The performance of the selected control gains is evaluated based on the achieved position- and velocity-state accuracy and frequency response characteristics.

Joint Position Control—Trajectory error is used to benchmark the trajectory-tracking performance of the inner-loop control. Joints 3–7 on the five-DOF version of the exoskeleton right arm (see Figure 14) were driven through a sinusoidal input to compare tracking accuracy in both position and velocity.

The sinusoidal input test was conducted by sequentially commanding each of the robot's joints to track 1 Hz position and velocity wave inputs. The sine input amplitude is ramped up from 0 to 10 degrees over 10 s. The amplitude is held constant for 70 s and then ramped down to zero over 10 s so that the joint returns to the center position. Ten seconds of pause time was included before repeating the process on a different joint to allow any vibration in the robot structure to dampen out. The state target inputs and resulting control torque signals are shown in Figure 16 for the experiment conducted on J_5.

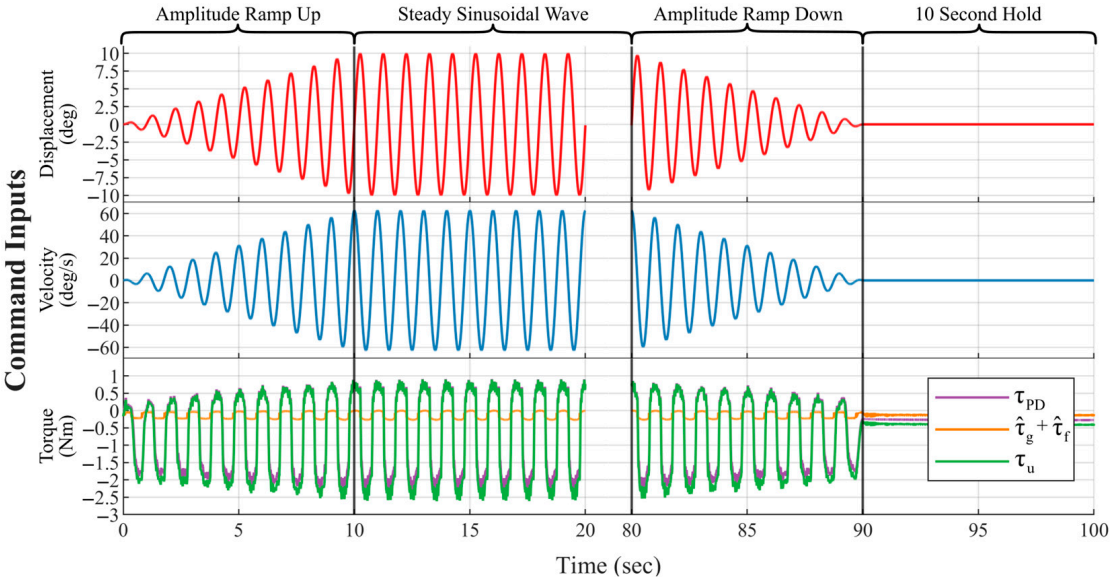

Figure 16. Sinusoid tracking inputs. The input position (red)- and velocity (blue)-state target signals are shown for an experiment using joint J_5. The PD control torque τ_{PD} (purple) and gravity/friction compensation torque $\hat{\tau}_g + \hat{\tau}_f$ (orange) are combined to generate the control input torque τ_u.

Defining the achieved tracking error for each joint as

$$\tilde{\theta} = \theta_d - \theta_m, \quad \dot{\tilde{\theta}} = \dot{\theta}_d - \dot{\theta}_m. \tag{21}$$

State-tracking accuracy for each joint is characterized by computing the root-mean-square error (RMSE) of position and velocity over the time samples in the steady-state portion of the tracking experiments (time t = 10 s to 80 s) and the variance of position and velocity error over time. Phase and time-response lag are estimated by locating the input and output position peak times and velocity response waves. Phase lag, Φ, is estimated by computing the time delay of the position and velocity states. On the steady-state portion of the input and response data, position and velocity waveform peaks are identified using MATLAB's "findpeaks" peak-finding function. A noncausal infinite-impulse response lowpass filter was used to smooth the state response signals so that the peak-finding algorithm is unaffected by high-order nonlinear dynamics. Then, time delay β, position-state magnitude response ratio, M_p, and velocity-state magnitude ratio, M_v, are estimated and averaged over all recorded time samples.

Chirp Test—Chirp-signal tracking experiments were performed to evaluate tracking performance over typical range-of-motion frequencies. The chirp tracking experiment

procedure is very similar to the sinusoidal tracking tests. Each of the five-DOF exoskeleton joints is sequentially commanded to track a logarithmic chirp wave whose frequency ranges from 0.1 to 2 Hz and has a 10-degree amplitude (Figure 17). The chirp wave is ramped up over 75 s and then ramped down over 75 s. In addition to recording state-tracking accuracy, the actuation torques were also recorded to measure the control/actuator effort required to maintain tracking over the considered frequency range.

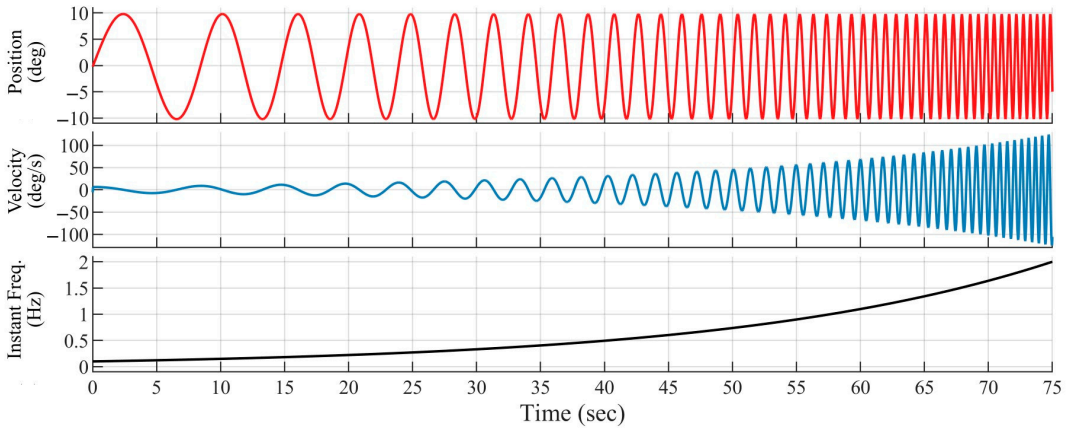

Figure 17. Logarithmic-ramping chirp-state inputs. The input position (red) and velocity (blue) state target signals, and the instantaneous command frequency (black) are shown for the first half of the experiment with chirp ramping up between 0.1 and 2 Hz.

2.8.6. Biosignal Acquisition Validation Methods

To assess the capability of our system to simultaneously capture electrophysiological data and kinematic measurements and yield valid results, we conducted a proof-of-concept multi-domain experiment. A simple and repeatable task involving movements of the right arm was performed while wearing the robot and EEG/EMG sensors. The task consisted of reaching with the shoulder and elbow to a predetermined point in a single fluid motion, and then returning to the initial position, with both initial and secondary locations marked by physical targets in the workspace (Figure 18). Thirty-two EEG channels referenced to the left earlobe (Figure 19) and five bipolar EMG channels (Figure 20) were acquired with the gHiamp biosignal amplifier (Sample Rate = 1200 Hz). An auditory cue (beep) was presented every 5 s to prompt movement initiation.

Figure 18. Biosignal acquisition validation task. The user begins the task with the fingertips touching the start target (tennis ball) located in the lower front part of the workspace. After hearing an audio cue, the user reaches to the second target (tennis ball) in the upper right part of their workspace, touches it, and returns their hand to touch the start target. An example trajectory for a single motion is illustrated in pink (**left**) in context of a virtual robot model. Pink arrows overlaid on the experimental setup (**center**) represent the movement from one target to the next and back. The transparent grey scatter (**right**) illustrates the area traveled in all repetitions on the same virtual robot charts.

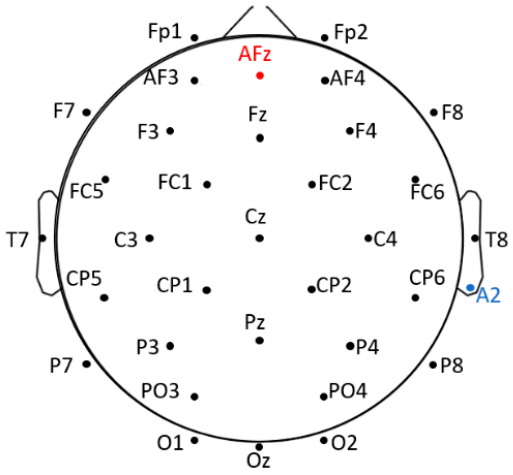

Figure 19. Topographical layout of EEG montage with reference electrode at A2 (blue) and ground at Afz (red).

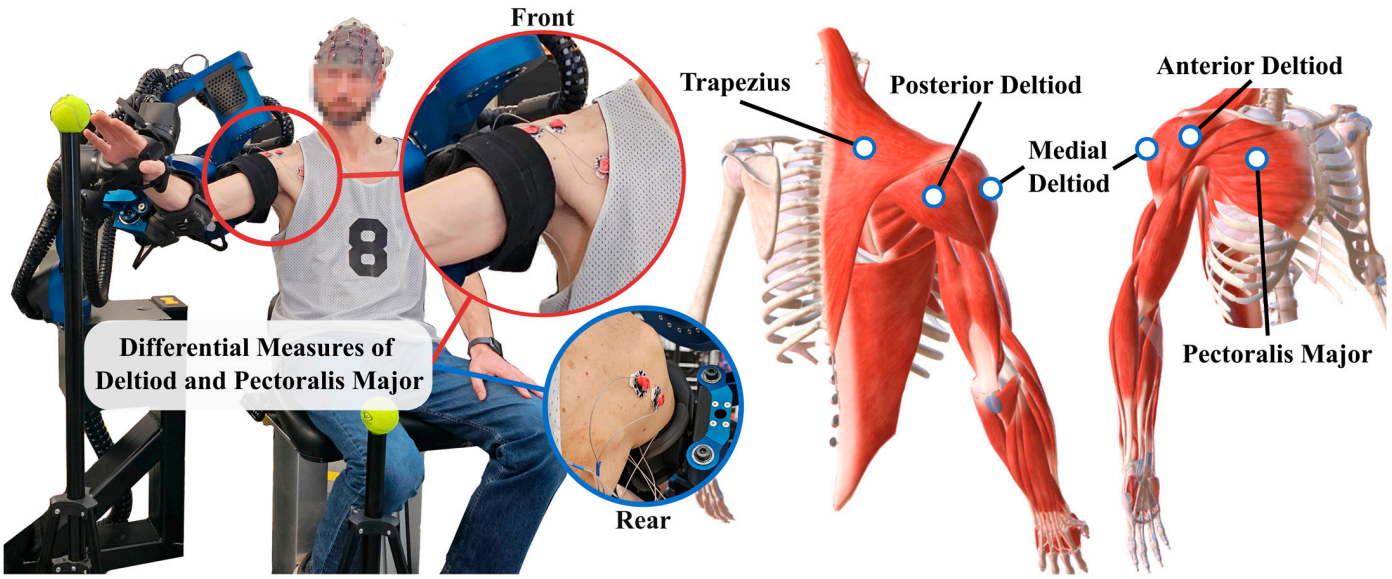

Figure 20. EMG montage and target muscles of the upper limb. Five EMG locations were placed on the skin over the shown target muscles. Bipolar electrodes were placed in pairs to enable differential measurement for improved noise rejection.

EEG electrodes were placed on the scalp in standard positions, overlapping functionally known areas of the brain (Figure 19) [94]. Proper electrode placement, required for acquiring reliable EEG data, is ensured by taking measurements of head circumference, the distances between mastoids, and the distance from nasion to inion, to correctly size and locate the cap, prior to data acquisition. During participant setup, conductive gel is applied at each electrode ring to reduce impedance and increase conductivity from the scalp to the electrode.

EMG electrodes were located bipolarly over large muscles involved in right-side shoulder movement (anterior, posterior, and medial deltoids; the trapezius; and the pectoralis major) (Figure 20). The skin under the electrodes was prepared with gentle use of fine-grit sandpaper and isopropyl alcohol to remove dry skin and oils.

A right-handed participant completed three blocks of 30 repetitions of this movement, totaling 90 repetitions. The instruction was to initiate the movement promptly upon hearing the cue and to maintain consistent timing in the movements throughout the repetitions. To ensure consistency in movement trajectories, a tennis ball denoted the location of each movement target.

Electrophysiological data recording (EEG/EMG) and stimulus presentation were managed through BCI2000 [95], and robotic data acquisition was facilitated by Speedgoat. Auditory cues were processed and translated into electrical pulses, which were transmitted to both Speedgoat and the biosignal amplifier as digital inputs (shown in Figure 10). This synchronization of cue presentation across systems was achieved by adapting the teensy code in the Audiomath Library [96], following the approach outlined in previous work by Rueda-Parra et al. [97]. Epochs were created for all signals (EEG, EMG, kinematic, and kinetic) for periods in the range of −2 to 4 s with respect to auditory cues. Then, all extracted features were plotted over this period (using the same time scale) as feature means over trials.

EEG was preprocessed following the steps in [97], with the goal of removing noise sources and extracting frequency band-specific power over time. We focused on contralateral (left hemisphere) changes in mu (μ, 8–12 Hz) and low-beta (Lβ, 13–20 Hz) power [98], as the behavior of these frequency bands during movement is well-documented [99,100]. This allows us to qualitatively compare our results with known electrophysiological patterns of active movement. The regions of interest were electrodes positioned over the left sensorimotor area, especially C3.

EEG power was obtained using the Morlet wavelet convolution method [91] and normalized to the period −800 to 200 ms with respect to stimulus presentation. Percentage changes relative to this baseline were calculated for both frequency bands. Frequency band power was averaged across trials. Lβ power was selected from the broader beta band (12–30 Hz) due to its close association with upper-extremity control [98].

Muscle activation patterns were extracted from EMG. These signals underwent band-pass filtering and rectification [101]. Subsequently, activation traces were averaged across trials. Finally, muscle activation patterns were normalized to the period −500 to 0 ms with respect to cue presentation and expressed as a percentage change. Muscle group activation was averaged across trials.

3. Results

The BLUE SABINO instrument is composed of nine core exoskeleton modules (Figure 21). Modules include (1) left and (2) right versions of the arm exoskeletons; (3) left and (4) right versions of the hand exoskeletons; (5) an individual module for positioning the patient with respect to the exoskeleton (i.e., a mobile chair with position-lockable casters and seat-height adjustment); (6) an individual module for adjusting the distance between left- and right-arm exoskeletons (i.e., a shoulder width adjustment mechanism); (7) a task display; (8) an operator console; and (9) a control tower. The PRISM modules (still under development) are represented in Figure 21 by a rigid box connecting each arm to each base. The final PRISM module will include a gravity-balancing mechanism and counterbalance that will replace the sandbags that currently enhance the stability of the arms when used individually. In the configurations shown in Figure 21, the control tower houses the electronics for the left arm while the operator console houses the electronics for the right arm; both employ open designs for easy access during development, while the final configuration will likely merge these into a single enclosed operator console, reducing the footprint of system peripherals.

Each arm module includes the exoskeleton, HRA orthoses, a rigid PRISM stand-in, a rigid base structure, and wiring with connectors to the operator console. The base of support is constructed from welded rectangular steel tubing and holds the arm exoskeleton at a pre-determined height. A purpose-built adjustable chair uses commercial lifting columns to elevate the subject for shoulder alignment. A width-adjusting mechanism connecting the steel-base structures provides a shoulder width adjustment range of 126 to 760 mm (5 inches to 30 inches). The large shoulder width range of motion (greater than anthropometrically required) allows for extra clearance during patient ingress/egress and makes the system more practical for use as a unilateral system. Therefore, the arm modules can be used independently or simultaneously as a bilateral arm and chair system. The

combined bilateral robot occupies a footprint of approximately 4 feet by 8 feet to ensure clearance from surrounding objects during use.

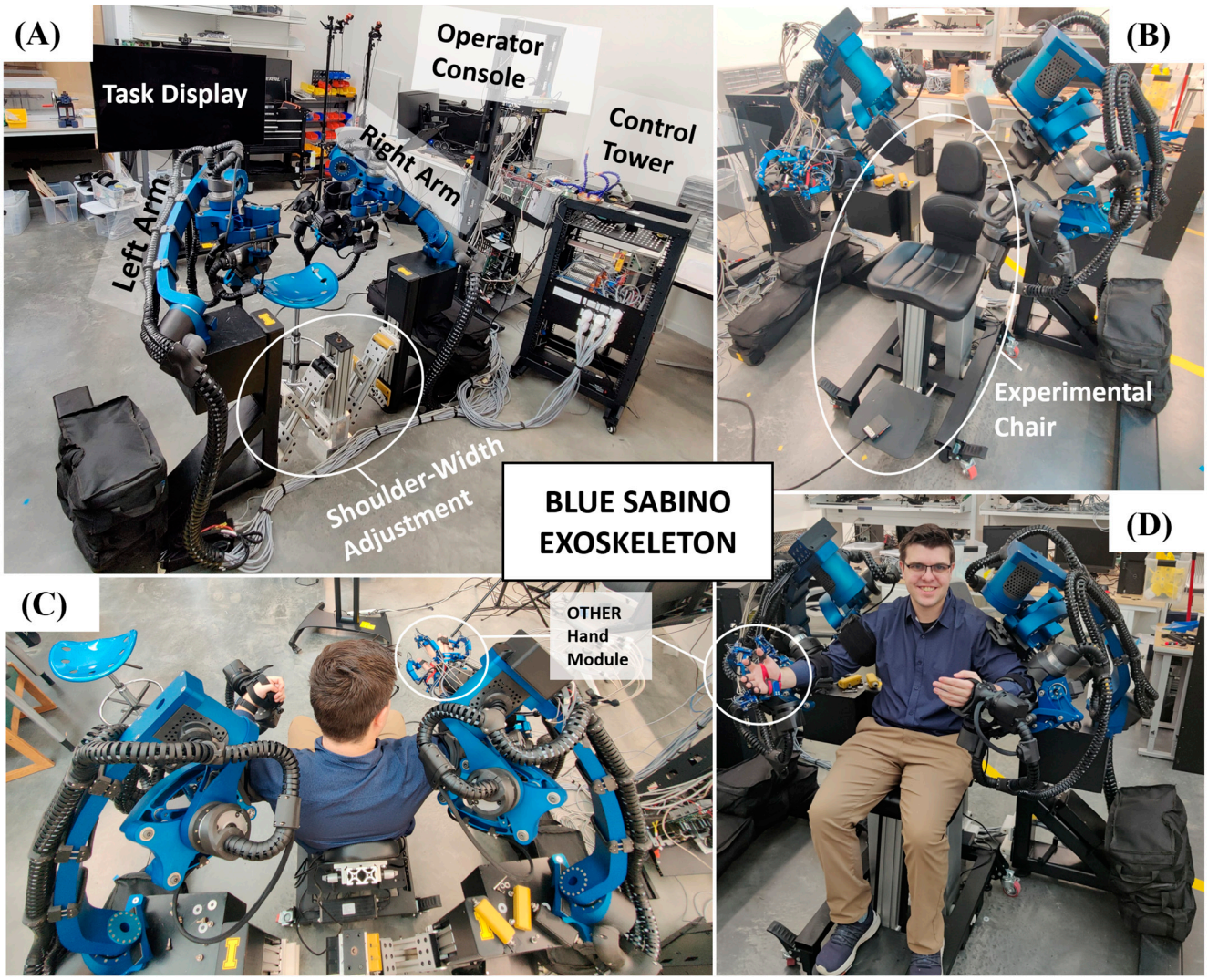

Figure 21. BLUE SABINO exoskeleton: (**A**) Seven-DOF bilateral arm configuration with task display screen, operator console, control tower, and shoulder-width adjustment mechanism; (**B**) Experimental chair with footrest and control-enable footswitch; (**C**) Overhead and (**D**) front views with subject wearing right-hand three-fingered OTHER Hand module.

In bilateral configurations, left and right base modules are connected via a leadscrew-driven scissor mechanism that symmetrically pushes or pulls the two modules apart or towards a central adjustment column. The base modules provide a stable base of support to each arm exoskeleton and can be used as standalone unilateral structures or as a connected bilateral (left- and right-arm) system. In the system shown in Figure 21, weights have been added to the base to increase stability; however, these will later be replaced by a gravity-balancing mechanism for PRISM with integrated counterweights while maintaining the minimum footprint required to delineate the robot workspace boundaries. In the bilateral setup, the width-adjusting scissor mechanism connects left- and right-arm base structures to create a base of support with increased stability, one that delineates the bounding workspace of both left and right arms of the robot. In both unilateral and bilateral setups, wheels on the mobile chair are used to position the subject with respect to the robot and then are retracted to lock the desired position in place. Once in position, the seat height can be electronically adjusted with a digital readout ($\pm$0.05 inches; $\pm$1.27 mm).

The hand modules are equipped with 12 DOFs (six active and six passive) in each hand, allowing for the independent control of the thumb and index and middle fingers. Additional details of the hand exoskeletons (Figure 22) are reported in [102]. The following subsections provide results of the BLUE SABINO instrument functional validation of the following areas: (1) kinematic calculations, (2) exoskeleton position accuracy, (3) anthropometric adjustability, (4) safety systems, (5) control systems, and (6) biosignal acquisition.

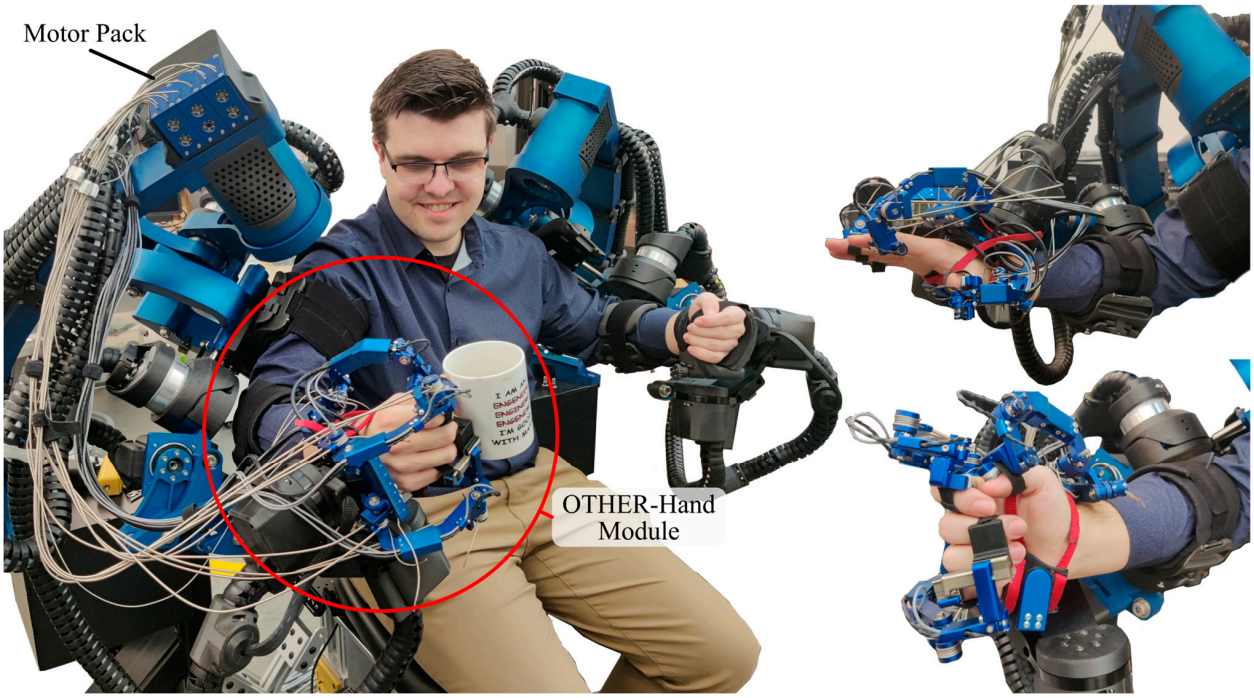

Figure 22. OTHER Hand on the BLUE SABINO System.

3.1. Kinematic Validation

The developed kinematic simulation code incorporates features including the ability to display link centers-of-mass and coordinate frame orientations, and it offers configurability such that any subset of links, human arm segments, or robot version (e.g., 5-DOF-RIGHT or 9-DOF-LEFT, etc.) can be shown. Using the 18-DOF-BILATERAL robot configuration, the animator was used to generate videos of ADL joint motions (from [59]), demonstrating the expected mirrored robot kinematics for bilateral arm movements (Figure 23).

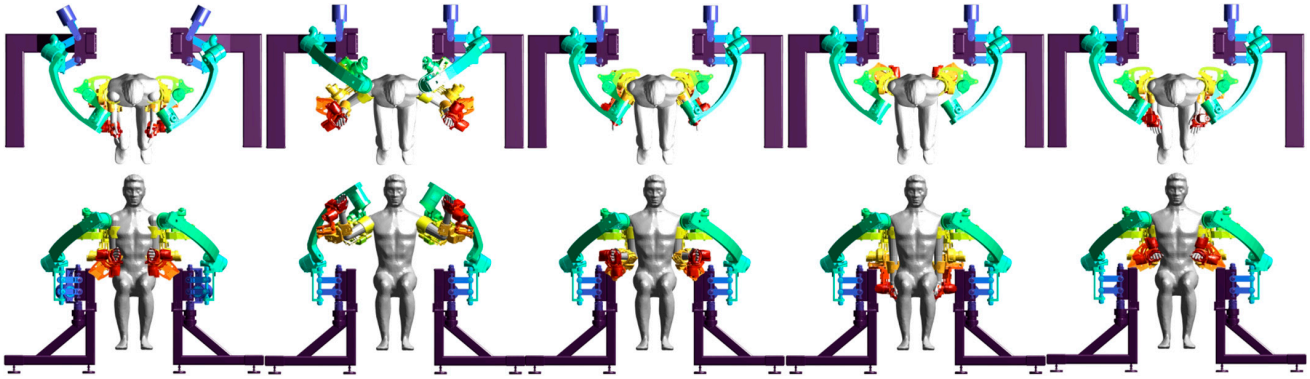

Figure 23. Animation of BLUE SABINO joints via kinematics-driven MATLAB script.

The force mapping was validated first by inspection, ensuring that the application of simplified wrenches at each joint produced forces in the expected directions. The Jacobians

for 14-DOF-BILATERAL have been further tested through application to the force control, resulting in the robot correctly responding to user-applied forces.

3.2. Spatial Measurement Validation

In the trajectory tracing experiment, two different types of error are measurable, corresponding to (1) the ability of the system to accurately track a pre-determined trajectory, referred to as tracking error or tracking accuracy, and (2) the ability of the system to accurately know its current position, referred to here as position error or position accuracy. Tracking error is more relevant for industrial robotics, where inaccurate trajectory tracking results in task failures. Position error is more relevant for rehabilitation and assessment, where knowledge of true arm position is the primary objective.

The experimental validation of position accuracy shows that the tracking accuracy predicted by the encoder-driven forwards kinematics (FK) are in good agreement (i.e., within 2 mm at the end effector) with the motion-capture (MC) results. Figure 24 shows the measured trajectories using FK and MC approaches in comparison to the target trajectory. Figure 25 provides a comparison of errors between each tracking method, where the first two charts provide an indication of the absolute tracking accuracy per motion, and the rightmost chart provides a measure of the agreement between FK and MC measurements (i.e., the accuracy of the device to know its current position). The mean error across the selected tasks was approximately 1.8 mm between FK and MC estimates, whereas the mean errors from the target trajectory across all tasks were 2.8 and 3.1 mm for the FK and MC approaches, respectively (Figure 25). The MC results of Figure 24 show second-order damped oscillatory responses at corners of motion, indicating that much of the disagreement between the encoder and motion-capture results is due to periods of vibration in the exoskeleton structure; however, the low magnitude of error indicates that the joint and link designs were successful in producing a structure with adequately high stiffness. Interestingly, the front-plane UofI-I task exhibited notably less error than the other three tasks, with a mean error of less than 0.5 mm, as opposed to 2 mm (Figure 25).

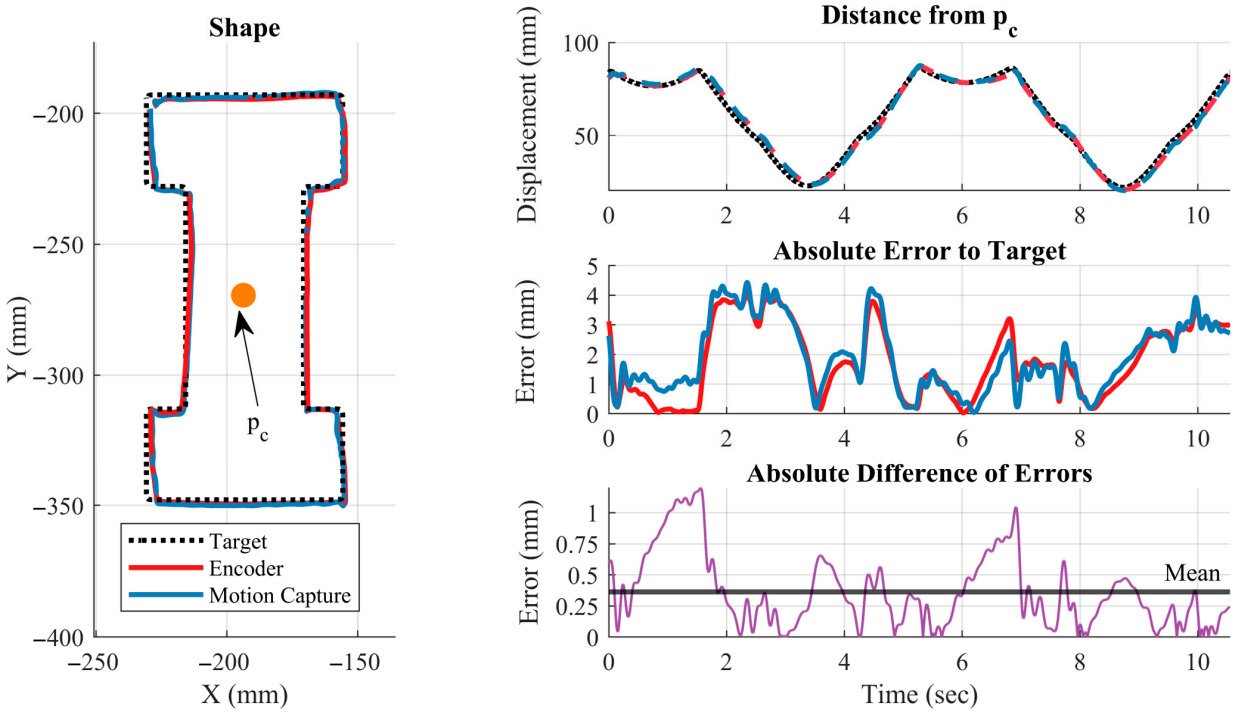

Figure 24. Results of motion capture for a segment of the UofI I trajectory illustrate the high agreement between end-effector position measured by motion capture (blue) vs. encoder position (red). The absolute difference (purple) remains low, indicating that the robot is able to accurately measure its true position within 0.4 mm on average for the task.

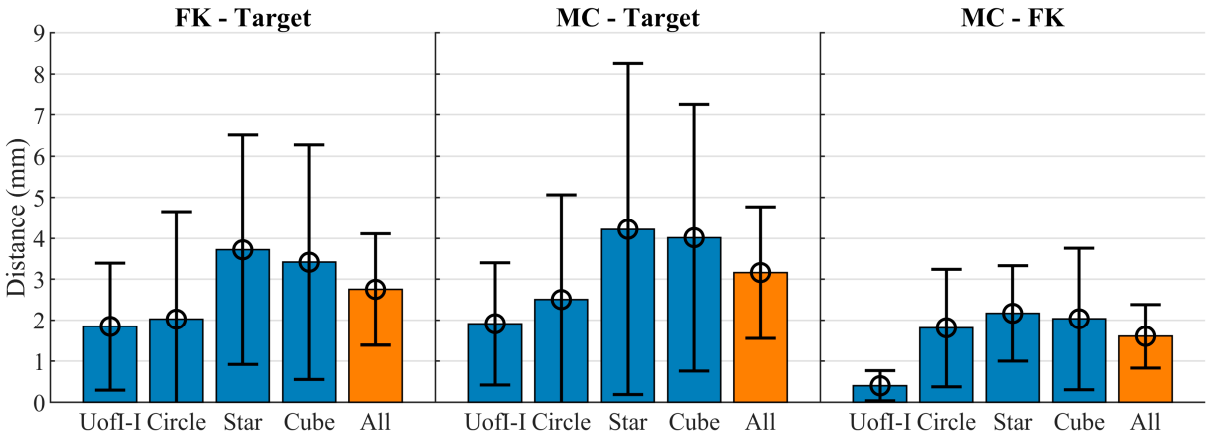

Figure 25. Mean tracking error per shape. The means of the distance error between the end-effector point p_c and the target position are shown on the left and center charts. The left chart shows errors reported by forward kinematics according to joint position measurements. The center chart shows the error according to motion capture. The rightmost chart displays mean absolute difference between the forward kinematic and motion capture measurements. Error bars display 95% confidence intervals of the means. Blue bars indicate statistics computed over individual actions (five repetitions each), while orange bars show statistics over all motions and repetitions (20 repetitions total).

3.3. Anthropometric Validation

The achieved range of anthropometric adjustments for body size is detailed in Table 8 and Figure 26, including adjustments in the custom chair, the base structure, the exoskeleton arm links, and the HRAs. The ROM accommodated is estimated in terms of the percentage of ADL and 50th-percentile male and female ROM coverage per joint, and on average over all joints (Table 9). Figure 27 graphically compares BLUE SABINO's attained ROM to the reported 5th- to 95th-percentile anthropometric healthy ROM [62,63,103–105] and to the approximate ROM used during ADL tasks (collected in a previous study [64,106,107]), which is most relevant for rehabilitation. For further information on the ADL data mapping to anthropometric joint ranges, see [75,106,107].

Table 8. BLUE SABINO-achieved anthropometric adjustment ranges in millimeters.

Measure	BLUE SABINO Adjustability			Anthropometric Reference [62]	
	Min	Max	Range	5th-95th M/F Pctl.	M/F Range
Seat-to-Shoulder Height	425	805	380	519–651	132
Foot-to-Seat Height	80	530	410	377–470	93
Shoulder Width	126	761	635	368–508	140
Upper-Arm Length	229	330	121	256–302	46
Forearm Length	222	330	109	221–271	50
Upper-Arm Circumference	304	440	136	244–351	107
Forearm Circumference	251	327	76	225–327	102
Hand Width	25	45	20	25–36	11

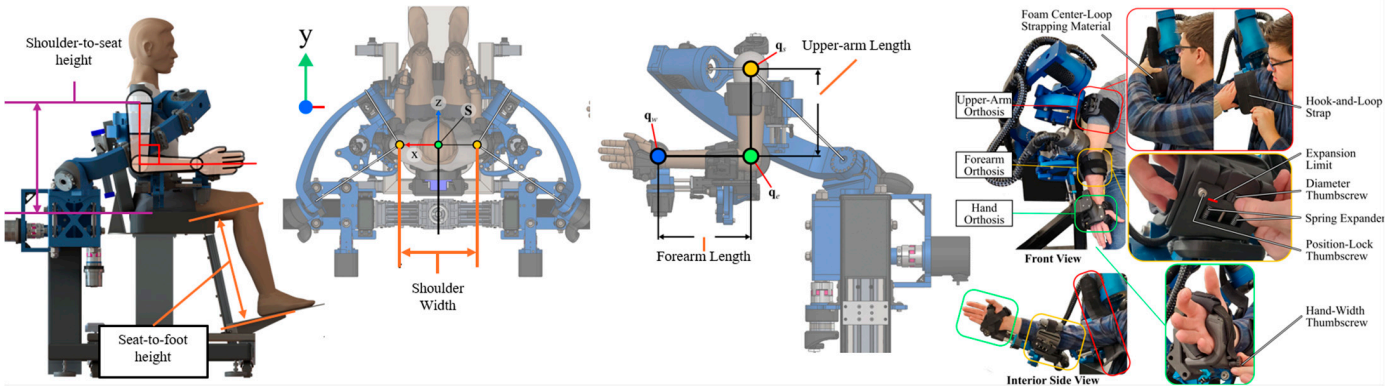

Figure 26. The adjustments supporting 5th to 95th percentile users in BLUE SABINO are included in its custom chair, base structure, length-adjustable arms, and the size-adjustable orthotic components forming the human–machine attachments (HMAs) and adjustment mechanisms.

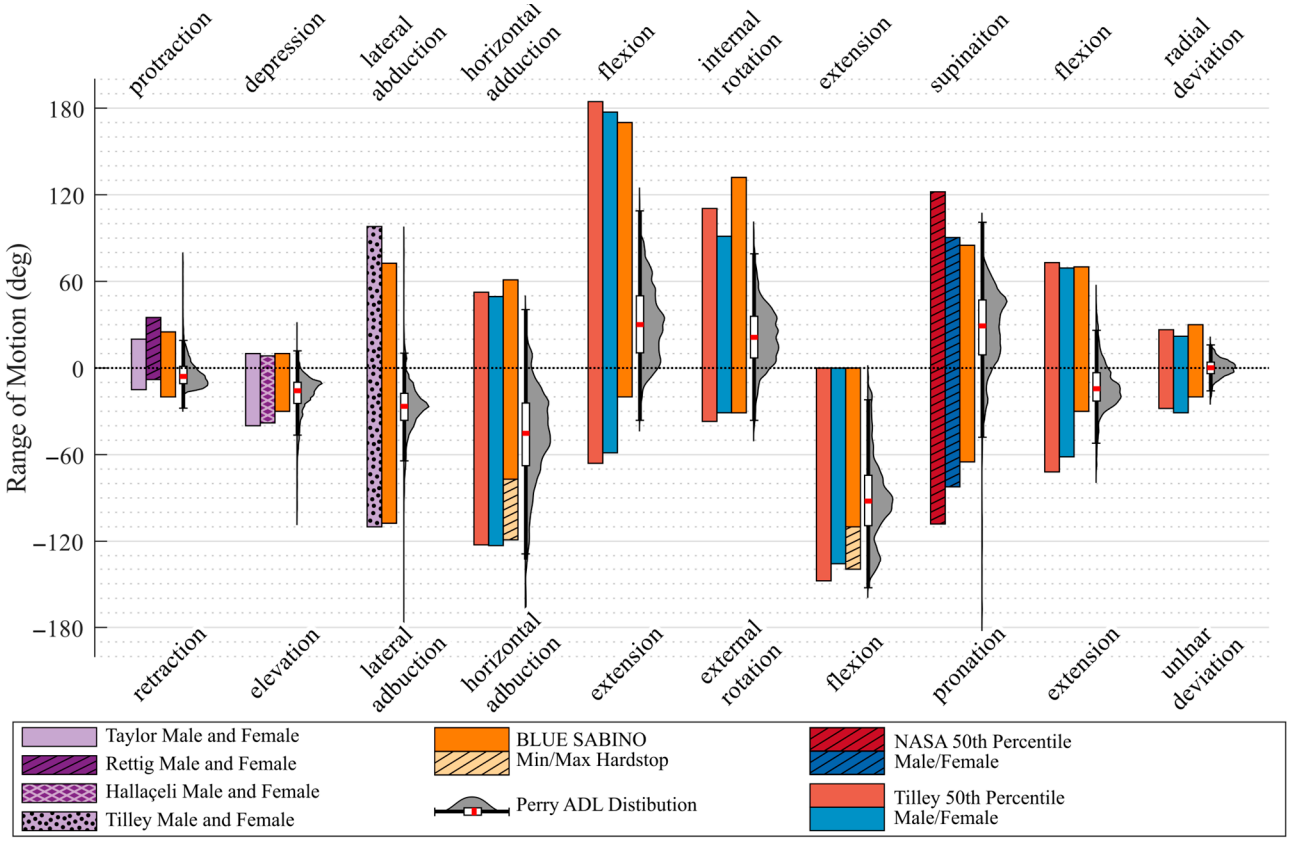

Figure 27. Range of motion comparison between healthy male and female ROM reported in [62,63,103–105], healthy movements measured by motion capture during ADL tasks [64,106,107], and BLUE SABINO's achieved ROM. BLUE SABINO's ROM encompasses approximately 95% of the ADL motion range for all joints combined. It also covers between 83% and 89% of healthy 50th-percentile ROM on all joints.

Table 9. BLUE SABINO achieved a range-of-motion coverage percentage of ADL distributions and 50th percentile male/female biomechanical range.

	Protraction/ Retraction	Depression Elevation	Adduction Abduction	Horizontal Abduction Horizontal Adduction	Flexion Extension	Internal Rotation External Rotation	Extension Flexion	Supination Pronation	Flexion Extension	Radial Deviation Ulnar Deviation	Total Coverage
Perry ADL	97.0%	82.0%	99.2%	96.4%	98.7%	99.0%	96.8%	98.1%	89.6%	99.8%	95.6%
50th Percentile Male	100.0%	82.8%	86.5%	97.7%	80.5%	100.0%	100.0%	86.9%	75.9%	79.2%	88.6%
50th Percentile Female				98.0%	75.8%	95.9%	94.6%	65.2%	69.0%	85.3%	82.9%

3.4. Safety Validation

The safety validation includes the confirmation of location and operation of manual E-stops, built-in hardstops, and automatic software limits.

3.4.1. Manual E-Stops Human/Electromechanical Response Time

The manual E-stops were verified through a simulated error event. An error message was presented to the operator at a random time, and the operator was required to hit an emergency-stop button. The recorded time between the error occurring and when the robot detected the E-stop being pressed is reported in Table 10. The test includes human reaction time and the motor driver's response in initiating the safety torque off (STO) feature in the driver. The average response time was 1.49 s with a standard deviation of 0.41 s, while the system contributes just 0.11 s (7.4% of the overall delay).

Table 10. Simulated response time to perform an emergency stop based on repeated trials with a random event.

Human Response Time (s)	System Response Time * (s)	Total Response Time (s)
1.3196	0.110	1.4296
0.8621	0.110	0.9712
0.9680	0.110	1.0780
1.4159	0.110	1.5259
2.0883	0.110	2.1983
1.3580	0.110	1.4680
1.6250	0.110	1.7350
Average: 1.377 s		Average: 1.487 s

* Estimated delay from E-stop relay documentation.

3.4.2. Range of Motion Hardstop Limits

The absolute ranges of motion of BLUE SABINO's joints are limited by the mechanical hardstops integrated into its design. The maximal ROMs allowed by the mechanical hardstops are reported in Table 11.

Table 11. BLUE SABINO ROM hardstop limits. Limits are reported for the right side following the robotic sign convention and home position defined in the earlier kinematics section (Figure 3) for positive (Pos) and negative (Neg) direction of motion for the shoulder (SH), elbow (EL), forearm (FA) and wrist (WR).

Robot Joint	Pos CCW Limit (deg)	Corresponding Anthropometric Motion	Neg CW Limit (deg)	Corresponding Anthropometric Motion	Total Joint ROM (deg)
J_1	25 *	SH. Prot.	20 *	SH. Retr.	45 *
J_2	20 *	SH. Elev.	20 *	SH. Depr.	60 *
J_3	10	SH. Add./Flex.	170	SH. Abd./Ext.	180
J_4	55 (No Insert)	SH. Abd./Ext.	187.5	SH. Add./Flex.	242.5
	31 (45° Insert)				218.5
	10 (24° Insert)				197.5
J_5	31	SH. Ext. Rot.	132	SH. Int. Rot.	163
J_6	20 (110° Front Plate)	EL. Flex.	90	EL. Ext.	110
	50 (140° Front Plate)				140
J_7	65	FA. Pron.	85	FA. Sup.	150
J_8	30	WR. Ext.	70	WR. Flex.	95
J_9	20	WR. Uln. Dev.	30	WR. Rad. Dev.	50

* Joints 1 and 2 limits represent the limit specified in the CAD model.

As indicated by the terms insert and front plate in Table 11, the hardstop limits for J_4 and J_6 can be modified by inserting one of several optional components designed to reduce the range of motion of particular joints, in the event that the individual has difficulty or pain with normal ranges of shoulder elevation or elbow flexion.

3.4.3. Software and Safe Limits

In addition to hardstops, software limits are used to both reduce contact with hardstops and maintain safety within the allowable workspace. Soft-limit boundaries are therefore set to a three-degree offset from hardstop contact, with a maximum overshoot of three degrees. Safe limits have been set at one degree from the hardstop impact, leaving a two-degree range available without triggering a safe mode. In normal use, this was found to be the smallest window that was not regularly triggered accidentally under normal movement conditions.

3.5. Controller Validation

At the time of writing, the left and right sides of BLUE SABINO have been implemented without the PRISM mechanism (Joints J_1 and J_2). Below, we report on results of a sinusoidal tracking experiment and a chirp-trajectory tracking experiment, both conducted with the five-DOF configuration (J_3–J_7).

3.5.1. Sinusoidal Input Tracking Experiment

The achieved steady-state position- and velocity-state-tracking accuracy are shown per joint for the five-DOF system in Figure 28. The shoulder joint, J_3, exhibits a peak alignment error of approximately one degree. Joint J_4 shows decreased velocity accuracy at peak speeds. Joints J_5 and J_6 are the most accurate overall, while joint J_7 exhibits the most variance, particularly in the velocity state. Notably, even when there is velocity error, it appears to be highly cyclical, as the velocity-error magnitude displays very little variance between waves, which is indicative of the under- or over-compensation of friction or drive dynamics stemming from the Harmonic Drive strain-wave gearing, as reported in [88,108–110].

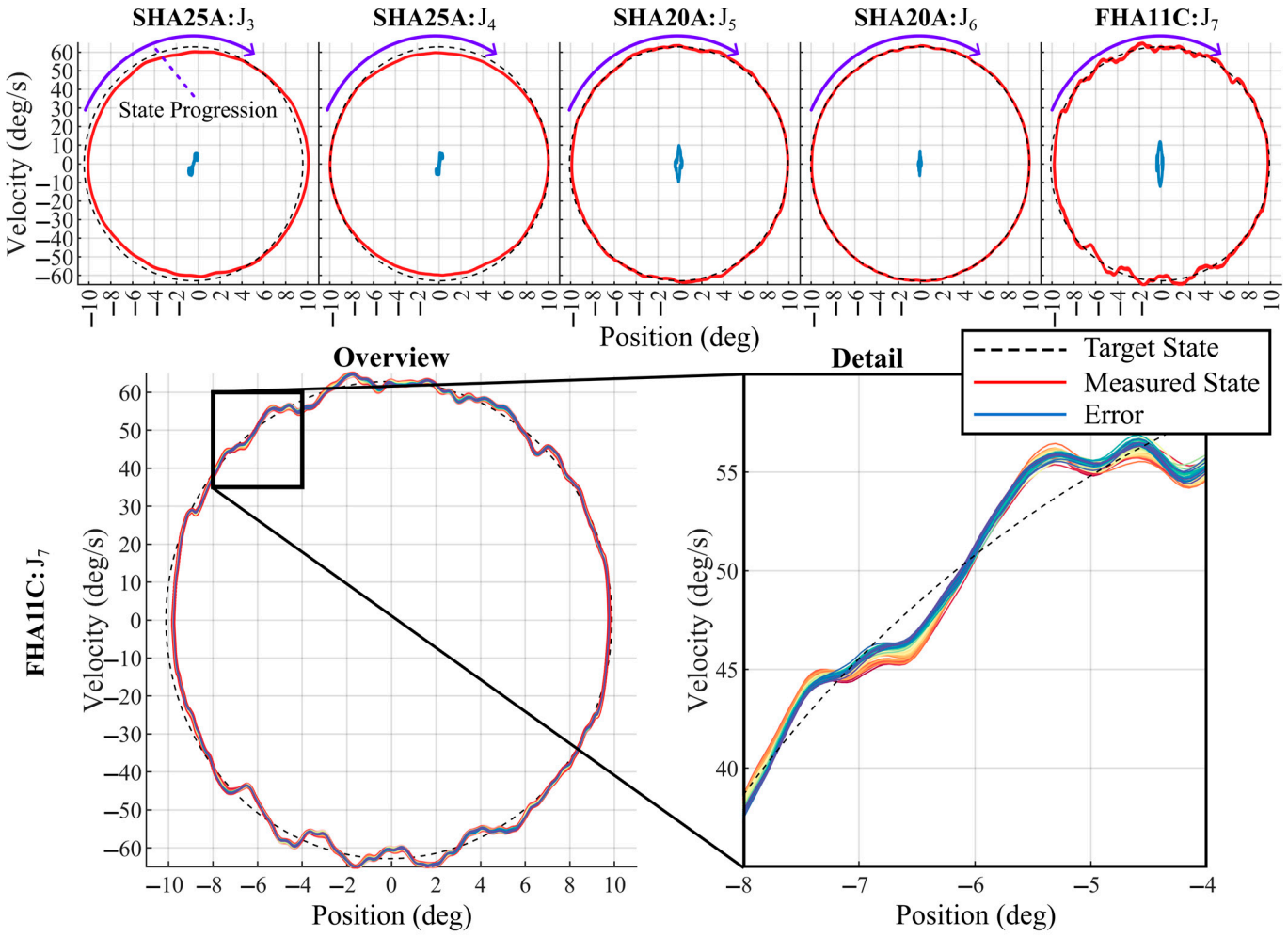

Figure 28. Sinusoid tracking-state accuracy. (**Top**) Position- and velocity-state tracking accuracy is shown for each of the joints of BLUE SABINO 5-DOF-RIGHT. Progression between states moves clockwise around each circle with the position and velocity states shown in red, and the error shown in blue. Only the portion of the input with full 10-degree amplitude (between 20 and 80 s in Figure 16) is shown. (**Bottom**) An enlarged view of the J_7 state chart shows the cyclical tracking error present in detail. Sixty wave cycles are shown with measured state line colors progressing from red to yellow to blue to highlight the variation of tracking accuracy between cycles.

Figure 29 illustrates the phase-delay estimation procedure on a segment of the J_7 time-series data. Table 12 summarizes the results of joint angle, phase delay, RMSE, and error variance results across all joints for the sine-wave-tracking performance evaluation. The estimated phase delay averaged 0.007 ± 0.002 s across the five joints, with the largest delays occurring on J_5 and J_7 and the smallest on J_6.

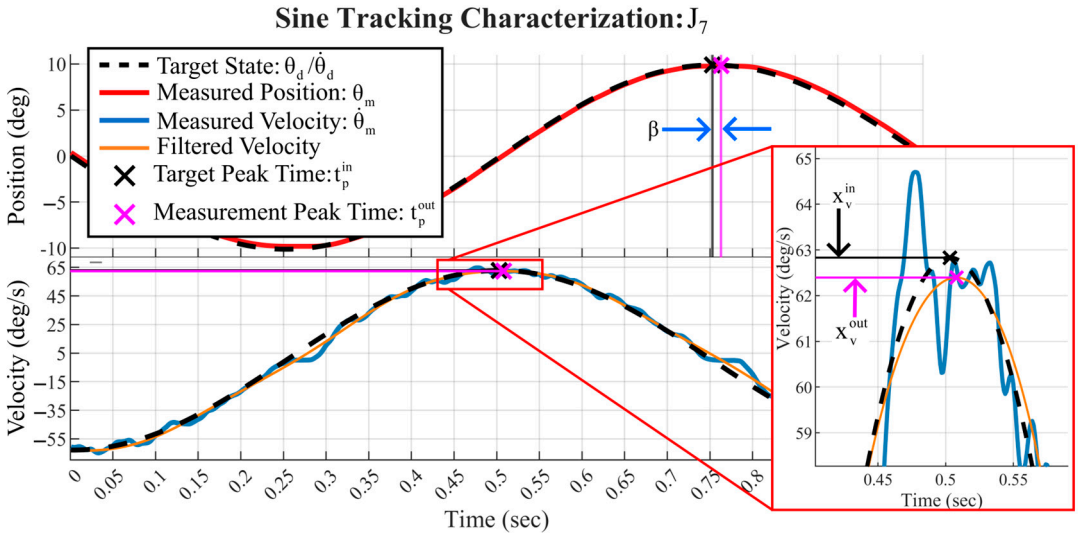

Figure 29. Sinusoid tracking phase magnitude characterization. A single sine-wave input and position/velocity response is shown for J_7. The velocity-state measurement is filtered using a noncausal low-pass filter with a 10 Hz cutoff that smooths the signal, making it easier to identify the response peak time. The state time delay β is extracted as the time distance between peaks of the target and measured position states. The state-magnitude ratios are computed via the measurement and target state values at the identified peak times.

Table 12. Sinusoid tracking results.

	Joint	Position				Velocity	
		M_p	Φ_p (deg)	β (s)	θ_{RMSE} (deg)	M_v	$\dot{\theta}_{RMSE}$ (deg/s)
Metrics	J3	1.056	2.526	0.007	0.509	0.956	3.125
	J4	0.999	2.367	0.007	0.187	0.946	3.261
	J5	1.002	3.240	0.009	0.254	1.000	2.692
	J6	1.004	1.800	0.005	0.128	1.000	1.616
	J7	0.997	3.246	0.009	0.255	0.992	3.286
Joints Avg.		1.012	2.636	0.007	0.267	0.979	2.796
Joints Std. Dev.		0.025	0.616	0.002	0.145	0.026	0.701

3.5.2. Chirp-Trajectory Tracking Experiment

For the chirp test analysis, the RMSE position and velocity error are computed over ten frequency bins; they are shown in Figure 30 to summarize tracking accuracy vs. input frequency. Each joint successfully maintains accurate tracking over the 0.1 to 2 Hz range. At low frequencies, the velocity states exhibit higher noise-to-input signal ratios but maintain high tracking accuracy. At higher frequencies, position and velocity errors increase. At 2 Hz, J_3 elicits the highest RMS position error of 0.7 deg, whereas J_5 and J_7 elicit the highest RMS velocity errors of just under 8 deg/s.

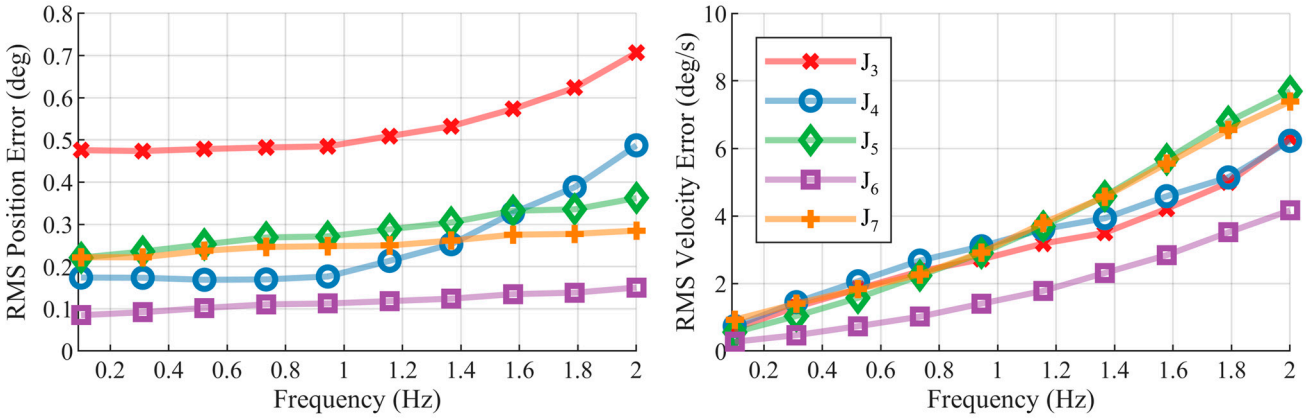

Figure 30. RMS chirp-trajectory state-tracking error vs. frequency.

To characterize the consistency of tracking performance vs. frequency, the position- and velocity-error variance are computed over ten bins. Because the directionally separated distributions exhibit lower variance, and the variance is approximately the same for clockwise and counterclockwise motions, only the results for the clockwise data are reported in Figure 31.

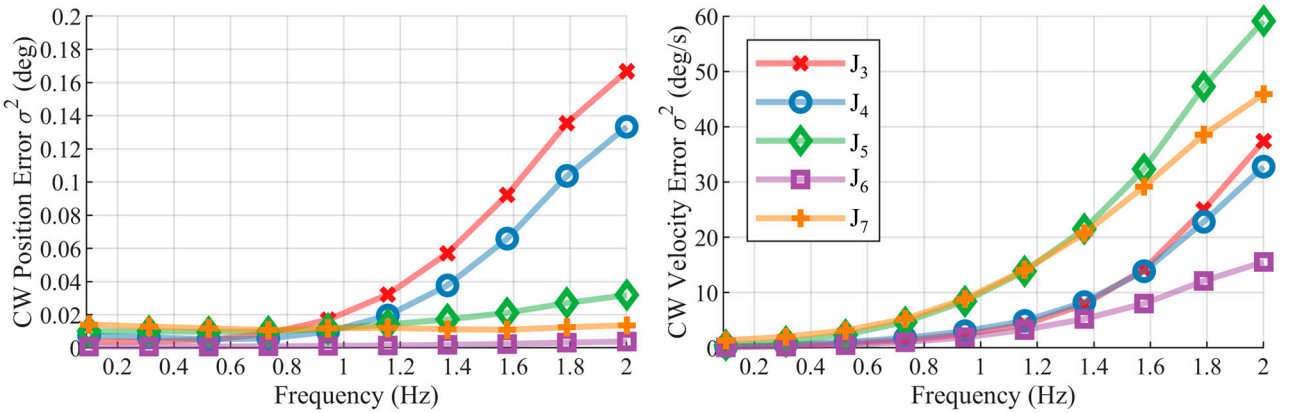

Figure 31. Chirp-trajectory state-tracking-error variance vs. frequency.

Comparing the command torque (i.e., control "effort") required to perform the chirp-tracking tasks at each joint provides insight into the adequacy of each motor/gear pair to deliver the desired movement. Control effort results are shown in Figure 32 in comparison to the continuous and peak torque bands. At low frequencies, all joint torques remain within the continuous torque band (green). At 2 Hz, the torque demands on joints J_3 and J_4 regularly exceed the continuous torque limits and enter the max torque band (blue). None of the joints exceeded the maximum torque band limit (red), indicating that the five-DOF robot maintained acceptable torque command levels for low and high frequencies.

As shown in Figure 32, most of the continuous torque band is used, and the maximum torque band is used transiently without exceeding its limits. This indicates that our tuning effectively leverages the capabilities of our motors and achieves nearly the best frequency-tracking capabilities that can be produced with PD control. This also means that we can achieve the maximal potential force bandwidth via our method of admittance tuning.

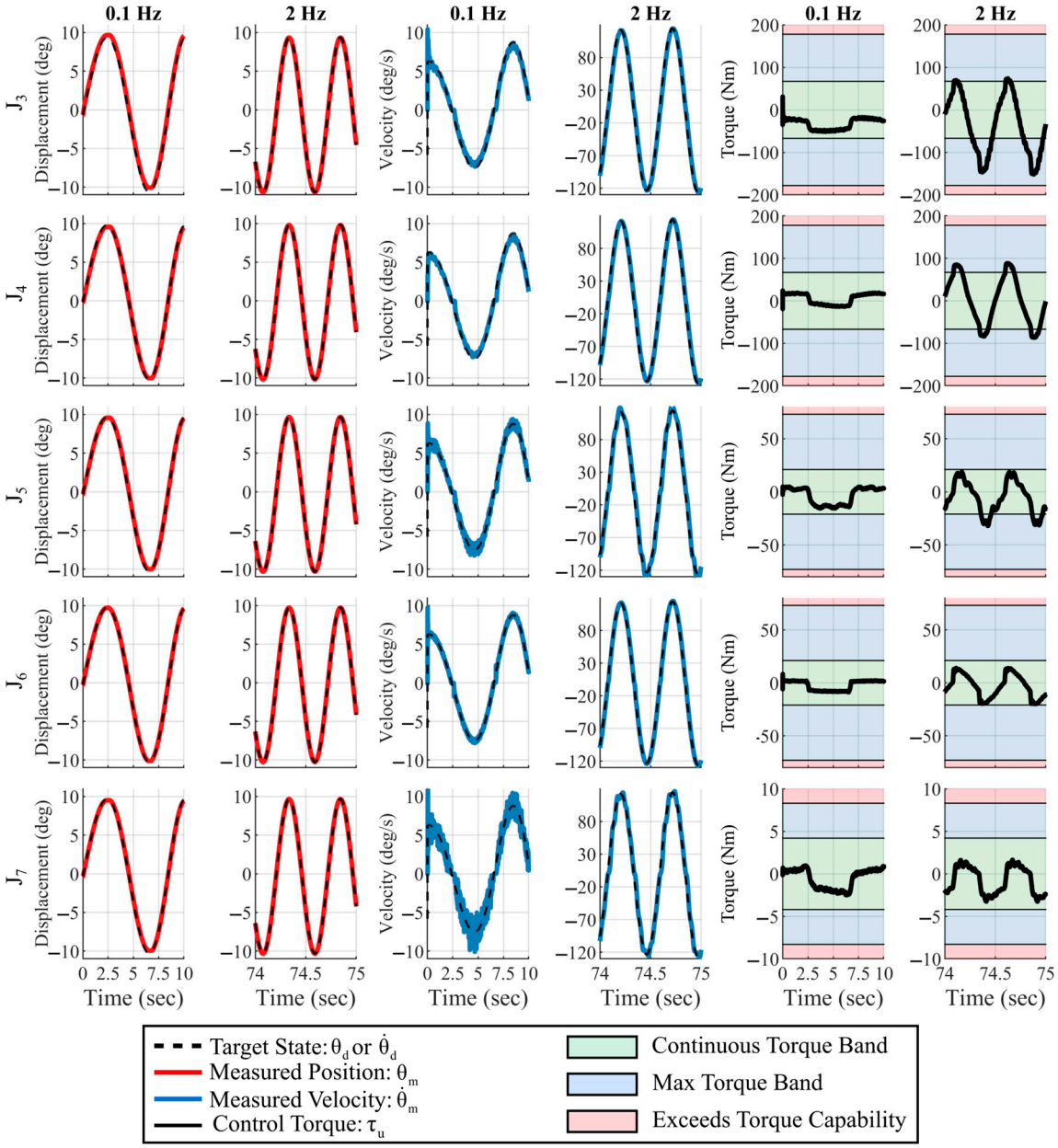

Figure 32. Logarithmic-ramping chirp-tracking time-series results. The input position (red)- and velocity (blue)-state targets signals and the instantaneous command frequency (dashed black) are shown in the first four columns. Command torque signals are shown on the fifth and sixth columns, overlaid with each actuator's continuous and peak torque output band.

3.6. Biosignal Acquisition Validation

The biosignal acquisition experiment was conducted with the right arm of the seven-DOF configuration. In Figure 33, hand displacement, hand velocity, and shoulder torque are plotted for each reach-and-return repetition along with their respective ensemble averages, giving a sense of the overall variance in the data. In Figure 34, similar ensemble averages of EEG power (μ and Lβ) and EMG power are plotted on the same timescale as the ensemble averages from Figure 33 to qualitatively assess the correspondence between neurological and biomechanical signals. Time correlations between these signals were computed to further validate this correspondence (Table 13). Finally, EEG topographical plots are presented to provide insight into the brain regions that are most responsive to the experimental task in the Lβ band (Figure 35).

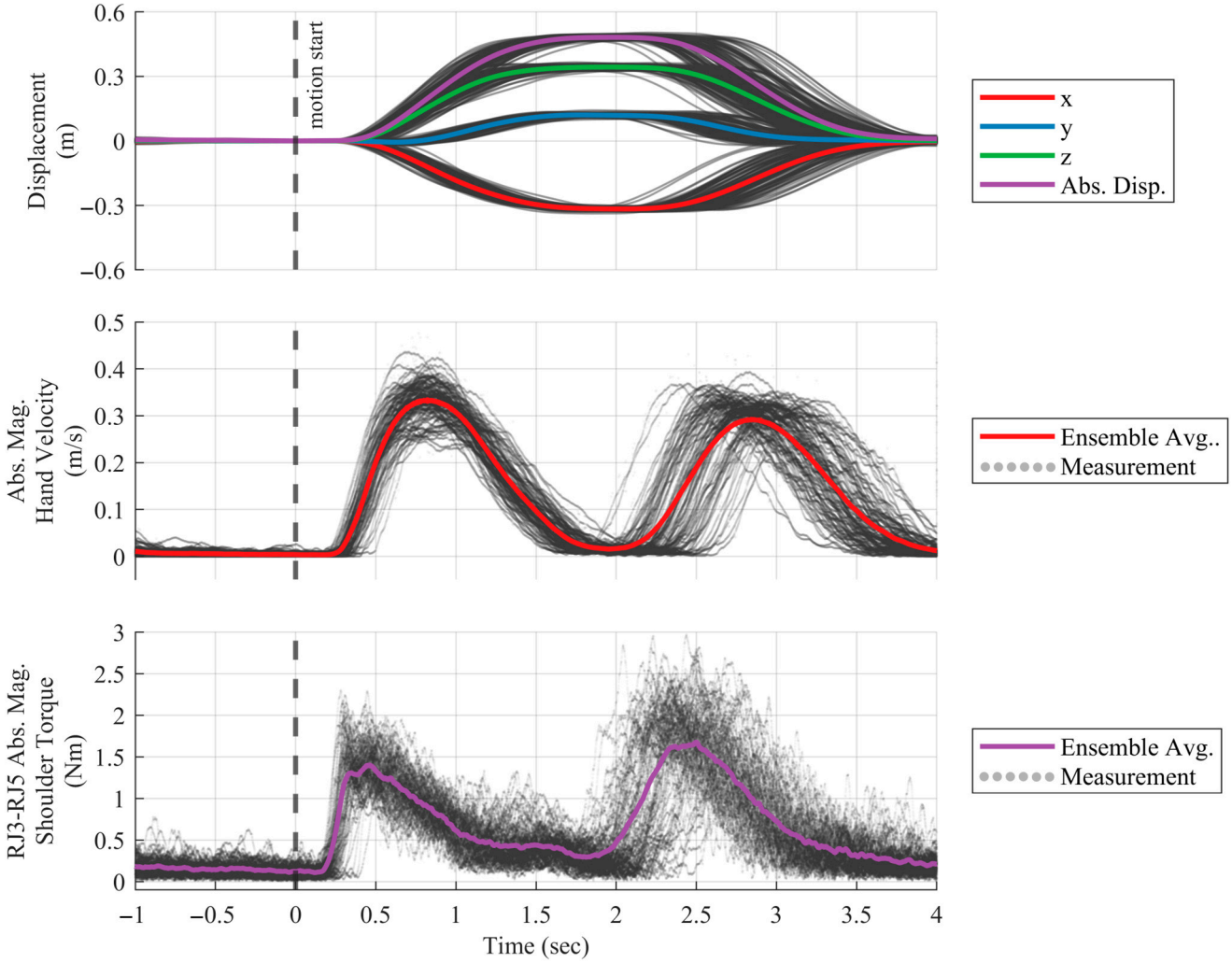

Figure 33. Ensemble-averaging robotic measures. (**Top**) Hand displacement in x (red), y (blue), z (green), and absolute displacement (purple); (**Middle**) Hand-velocity ensemble average (red) of all measurements (grey); (**Bottom**) Required shoulder torque to complete each reach trajectory and the ensemble-average torque profile (purple). Individual trajectories from all reach movements and shoulder torques required to drive the exoskeleton are displayed in grey.

Several relationships can be seen in the multi-domain data of Figure 34, including synchronizations between features of contralateral EEG power and right-hand displacement, velocity, and right-shoulder torque. Two event-related synchronizations (ERS) occur in the EEG power time-series in both Lβ and μ bands in concert with shoulder torque. Torque and EMG are also synchronized, as expected, as are EEG Lβ power and EMG activation—a confirmation of cortico-muscular coherence [111]. The first ERS in Lβ power is observed following the rise of EMG, shoulder torque, and hand velocity. One clear event-related desynchronization (ERD) in Lβ power is observed at about 1.4 s, which coincides with maximal EMG and the reduction of torque and velocity measures toward local minimum values. A second ERS follows at 2.51 s, corresponding to the return-to-home motion. Using the 20%-rise point as the onset event for displacement, velocity, and torque, the onset order following a muscle contraction is torque, velocity, and then displacement, with displacement's 20%-rise point occurring 0.12 s after the first ERS peak and the 20%-fall point occurring 0.10 s after the second ERS peak. Similarly, the 20%-rise points in hand velocity occur 0.13 s after each of the 20%-rise points in shoulder torque.

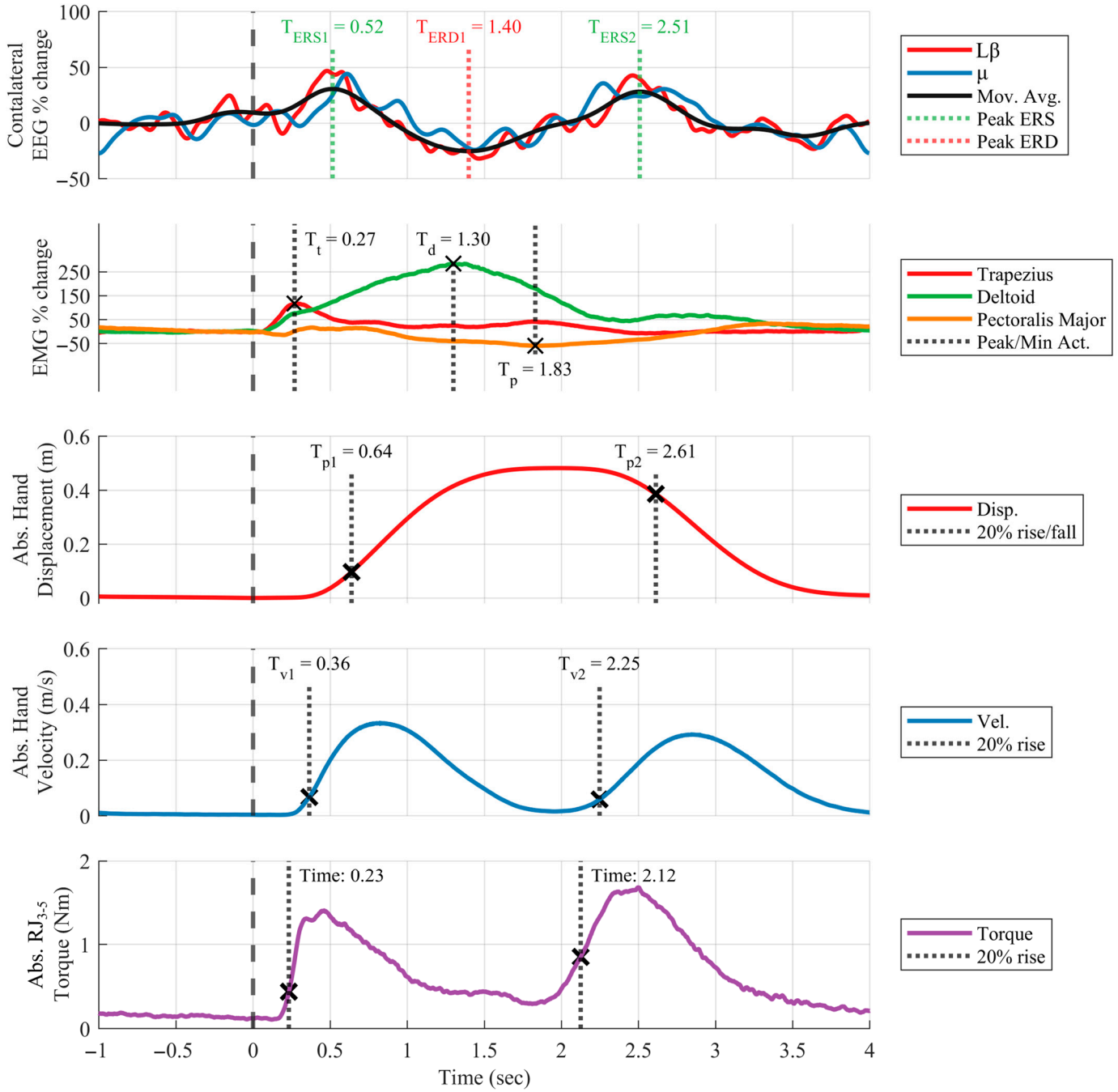

Figure 34. Trial average EEG, EMG, and robot kinematics. The ensemble-averaged biosignal including contralateral low-beta EEG at C3, EMG from three shoulder muscles, and robotic measurements, including the displacement and velocity of the right hand, and the absolute summed magnitude of interaction torque between the user and robot's shoulder joints.

Analysis with Pearson's correlation coefficient (Table 13) provides additional support for the relationships between signal profiles, highlighting the correlation between shoulder torque and EEG, hand displacement and EMG (proportional with deltoid, inversely proportional with pectoralis major), and hand velocity and shoulder torque.

Table 13. Correlation matrix showing Pearson's correlation coefficients between select measures of EMG, EEG, displacement, velocity, and torque.

Pearson's Correlation Coefficients									
	EEG Contra. Beta	**EEG Contra. Low Beta**	**EEG Contra. Mu**	**EMG_Trap.**	**EMG Med. Delt.**	**EMG Pect.**	**Hand Disp.**	**Hand Vel.**	**Shld. Torq.**
EEG Contra. Beta	1.00								
EEG Contra. Low Beta	0.92	1.00							
EEG Contra. Mu	0.82	0.72	1.00						
EMG Trap.	0.00	0.12	0.06	1.00					
EMG Med. Delt.	−0.23	−0.33	−0.07	0.40	1.00				
EMG Pect.	0.07	0.14	−0.09	−0.16	−0.58	1.00			
Hand Disp.	−0.02	−0.17	0.13	0.02	0.65	−0.89	1.00		
Hand Vel.	0.32	0.13	0.43	−0.03	0.47	0.04	0.26	1.00	
Shld. Torq.	0.73	0.62	0.74	0.20	0.18	−0.22	0.41	0.56	1.00

Color Scale
1.00
0.00
−1.00

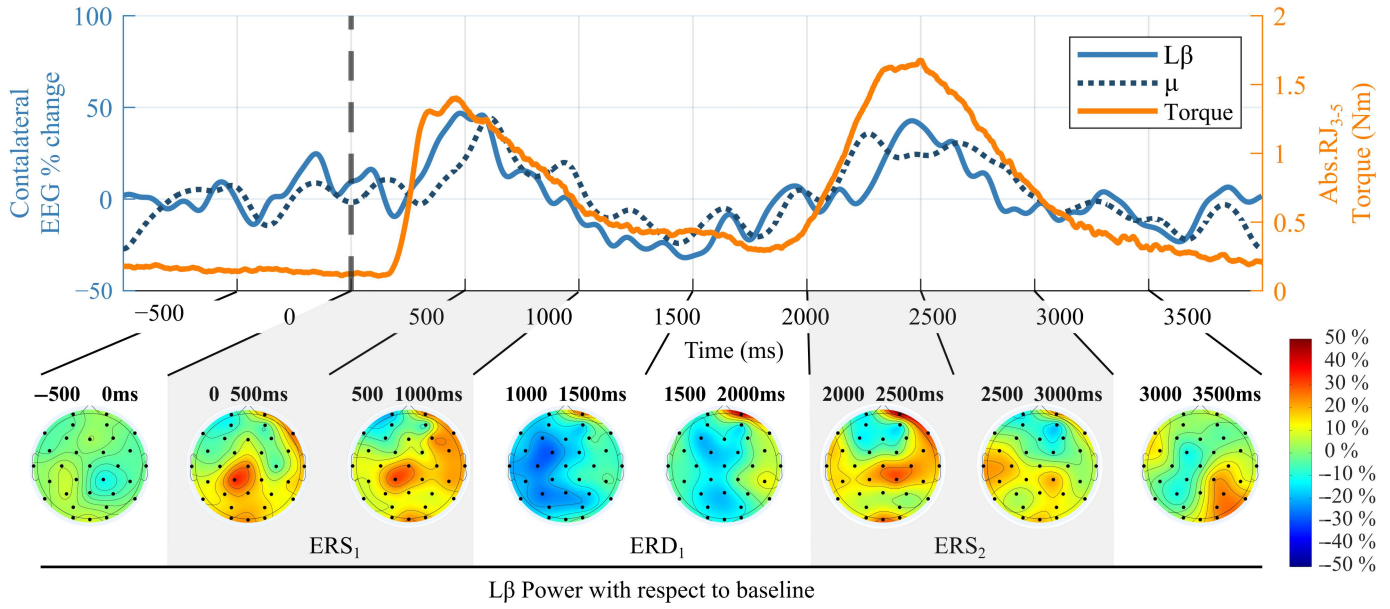

Figure 35. Topographical progression of EEG power: The top portion of the plot shows Lβ power and μ power at C3, as well as shoulder torque from robot joints (RJ) 3–5, from 1000 ms before the cue presentation to 4000 ms after the cue. On the same timescale along the bottom are topographical heat maps showing the percent change in Lβ power with respect to baseline.

The topographical time progression of Lβ power in the brain can be visualized in Figure 35 alongside the time-series plot of Lβ power, μ power, and shoulder torque from Figure 34. Relative to baseline −800 to 200 ms before the audio cue, a first left-hemisphere ERS develops from 200 to 1000 ms maximally located over CP1 and Cz electrodes. The ERD then develops from 1000 to 2000 ms with significant presence over the contralateral (left) electrodes. Finally, as the movement is terminated, a bilateral ERS over the centro-parietal areas is observed (from 2000 to 3000 ms).

4. Discussion

The results of the validation are further discussed in the subsections below, starting with a discussion of the importance of bilateral measurement and implications on design, followed by the same subsection structure of Section 2.8 (System Integration and Validation Methods) and Section 3 (Results), with the exception that the first two subsections on kinematics (Sections 2.8.1 and 3.1) and spatial measurement (Sections 2.8.2 and 3.2) are combined into a single discussion section (Section 4.2) following a discussion on the importance of bilateral kinematics.

4.1. The Importance of Bilateral Kinematics

A major focus in the BLUE SABINO design has been to support a large ADL-compliant workspace for both arms. This means that each exoskeleton arm can only occupy space on the side of the body that it supports. This constraint drove the original placement of the shoulder singularity in UL-EXO7 and the design and placement of PRISM for BLUE SABINO. To our knowledge, these elections and the resulting design furnish BLUE SABINO with the largest workspace of any bilateral robotic exoskeleton system to date. While PRISM will further extend this workspace with the ability to maintain proper shoulder alignment during scapulothoracic movements, the range of motion provided by $J_{3–9}$ is already sufficient for the majority of tasks in both healthy and impaired users.

The bilateral capability allows individuals with impairment from stroke—a highly heterogenous population that primarily results in one-sided impairment—to perform intra-subject comparison between left- and right-side function. It also supports both the assessment and training of bilateral tasks such as folding clothes, washing dishes, cooking, or driving a car. The benefits of bilateral training have been reported in the literature for decades and have been shown to produce improvements in both bilateral and unilateral function. A bilateral exoskeleton system like BLUE SABINO has the capability to leverage these findings and quantitatively compare outcomes from different bilateral training approaches.

4.2. Kinematics and Spatial Accuracy

Achieving high positioning accuracy in the joints is extremely important for precision assessment instruments. While error varies with speed of motion, in the ranges of speed anticipated, average errors were 0.3 deg and 2.8 deg/s in 1 Hz sine-wave tracking, less than 1 deg and 8 deg/s in 0.1–2 Hz chirp testing, and 2 to 4 mm at the wrist in the trajectory tracing of predefined profiles. The correct measurement of its own position at the wrist (as confirmed by a separate motion-tracking camera setup) was more accurate than the accuracy of tracing predefined profiles. The system's self-measurement of position via motor encoders provides average errors between 0.4 and 2.1 mm. As a system for precision measurement, these are acceptable values as the measure of true position is the most relevant for impairment assessment.

The spatial accuracy of the system is a product of correct kinematics, the avoidance of play in joints and gearing, the rigidity of linkages, and precision sensing. Comparing motor encoder-driven forward kinematics (i.e., robot-calculated wrist position) to wrist position, measured with a motion-capture system (i.e., true wrist position), the BLUE SABINO achieves a highly accurate self-awareness of pose. The accuracy was highest in the frontal (X-Y) plane (~0.4 ± 0.4 mm) during the UofI-I task and was about five-times higher on average when the movement involved motions in the Z direction, perpendicular to the frontal plane. The UofI-I was the only task that involved no motion in the Z direction. It is possible that this difference in accuracy reflects play in the joints involved in the Z-direction movement and can be further reduced with error compensation strategies. Further testing and analysis should be conducted to confirm the accuracy of motion in the different directions as well as in different locations of the workspace, and the results can then be used to steer the error compensation approach as needed throughout the

workspace. Accuracy in trajectory tracing may be further improved through additional control optimization.

4.3. Anthropometric Adjustability

The anthropometric goal of the design was to accommodate 95% of the population (5th percentile male/female to 95th percentile male/female). While all but one of the adjustments are larger than the corresponding target range, some ranges are far greater than anthropometrically needed. The large range of shoulder width adjustment facilitates greater ease of use during subject ingress/egress and provides space for single-arm system use without full system separation.

The only values that currently fall short of the full target range are the sizes of forearm attachments, which lack coverage for the smallest arm sizes. However, it is worth noting that there is progressively less difference between percentiles at the lower end of the range, and as such, smaller subjects can easily be accommodated in the reported design by adding or changing the layers of internal HRA foam padding.

Between the adjustable range and use of additional layers of foam, a single adjustable HRA can provide a secure and comfortable fit with arms of the full 5th-to-95th-percentile target range. The current HRA design, however, does not adjust the radial offset from the exoskeleton (with respect to the long axis of the arm) to compensate for misalignment between the arm center and rotational center of the exoskeleton. If this alignment error were large, this offset would produce a noticeable circumduction of the arm around its long axis during axial rotation. Fortunately, the alignment error remains small across the expected population size (see Figure 36) and is imperceptible by subjects during use.

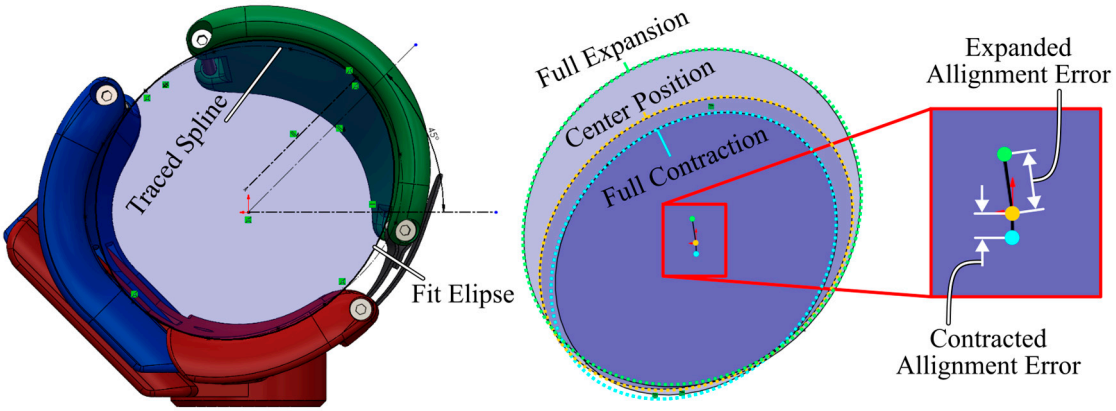

Figure 36. Adjustable HRA based on ellipse-fit forearm model. (**Left**) Three-piece HRA design. (**Right**) Ellipse size range with enlarged view of potential range of alignment errors. Colored dots represent the center location of each ellipse when the adjustment is fully contracted (cyan), centered (yellow), and fully expanded (green). Red axes represent the model coordinate system which was built around the 50th-percentile arm.

The most important segmental alignment occurs at the hand, where the end-effector position determines the position and orientation of the hand with respect to the environment. However, even axial offsets from J_7 (pronosupination) at the hand would be unnoticed during use, as the force-based impedance controller will move multiple joints in order to minimize forces and torques felt on the arm; this includes forces from misalignments. Interestingly, the palmar geometry of the hand HRA includes a convex portion that seats within the concavity of the palm and which tends to center hands of different sizes (including small percentiles) at the center of rotation, even if a gap is present between the lateral aspect of the palm and the base of the adjustable hand HRA.

4.4. Safety Systems

In the interest of maximal safety, redundancy and automation are key aspects of the safety architecture. Multiple systems (human, software, and sensors) continuously observe the machine's state and watch for signs of unwanted characteristics (motion, force, and electrical). While having manual stops is a necessity, the human response time is an order of magnitude slower than automated error detection. For this reason, extra effort has been put into building inherent safety within hardware and software limits. Software limits include both position- and velocity-based limits and can be easily adjusted to reduce the allowable workspace for subject-specific motion limitations. The hardware limits are more difficult to adjust, as changing mechanical plates and inserts requires disassembly and re-assembly, but it remains an option for reducing the mechanical workspace further.

Position Limits—BLUE SABINO's soft stops operate over the last three degrees of joint ROM. Because the soft stops are designed to stop motion prior to contact with the hardstop, under normal movement conditions, the soft stop provides progressive slowing over a three-degree range approaching each hardstop. While this may alter the contribution from joints acting near a system joint limit, we anticipate that this will primarily affect tasks performed close to and far from the body, such as specific hygiene tasks (e.g., brushing the teeth, washing the neck) and specific reaching tasks, when objects are placed near the borders of the user's workspace. Since most tasks can be evaluated in different parts of the workspace and bimanual tasks take place in the center where left- and right-arm workspaces overlap, the impacts on natural movement in ADL tasks can be minimized or eliminated, particularly for tasks performed by individuals with impaired (i.e., reduced) workspaces.

Velocity Limits—BLUE SABINO's velocity is continuously monitored by changes in motor-encoder position. The velocity command from the controller is capped by a saturation threshold, and the threshold value can be configured based on individual user capabilities or level of comfort with the exoskeleton. If the velocity threshold is set too low, the naturalness of free motion will be decreased. To maintain naturalness, the system should permit velocities in the expected ADL range of 100–200 deg/s depending on the joint.

Force Limits—The levels of interaction force and torque permitted between the user and exoskeleton are monitored via force sensors in the fingers and via force-torque (F/T) sensors in the arm. Similar to velocity thresholds, this force level is restricted by saturation thresholds that can be configured to the individual. At their maximal levels, these thresholds are limited to the safe operational ranges of each axis of the sensor, ensuring that accurate interaction forces are constantly monitored. Below this level, increasingly restrictive thresholds can be applied. In system testing so far, the limits imposed by the F/T sensor operational ranges are sufficiently well-suited for the range of human–machine interaction forces and torques encountered, such that we have not needed to limit the F/T thresholds further.

One layer of safety that is not fully addressed by the safety systems reported above is the potential for contact between the user and the exoskeleton outside of the HRA locations. With the use of high-precision responsive F/T sensors and a high-bandwidth low-impedance controller, any force or torque on the F/T sensors will result in a movement of the exoskeleton away from the applied load. It is important, therefore, that nothing in the environment contacts the exoskeleton except through the measurable interfaces of the F/T sensors. Due to the large workspace of the shoulder and the interrelation between J_3 and J_4, it is possible for the arm to rest directly against the body and even apply pressure on the body. This situation is safe if the physical contact is between the user arm and user torso, as contact with the inner surface of the arm will apply an opposing load on the F/T sensor and stop exoskeleton motion. However, if contact is permitted between a non-sensorized portion of the exoskeleton and the user, no F/T command will be generated to slow or reverse exoskeleton motion. In the BLUE SABINO design, the main ways this can occur are as follows: (1) a free hand (not secured to the orthosis) is inadvertently used to apply loads to the exoskeleton F/T sensor, or (2) the user is in a neutral or supinated forearm

pose and brings the hand too close to the lap in a seated position. In the latter case, the wrist flexion-extension motor at J_8 can contact the legs. For an able-bodied user with full sensory function, this is easily detected and avoided. The safety for impaired users with potential motor and sensory losses is not as clear.

To improve safety in collision avoidance between the exoskeleton and all users, a boundary should be added to the software similar to the soft stops approaching the system's mechanical hardstops. This boundary should surround the known locations of the user, such as the torso and upper thighs, and can be customized to the anthropometrics of each user to maintain the maximal free workspace of the arm and hand.

4.5. Admittance/Impedance Control

In the 1 Hz sine-wave tests, the RMS velocity error increases with command state frequency but remains under 8 deg/s for all joints over the tested range. The PD tuning used achieves higher-fidelity position-state tracking than velocity-state tracking. This is a consequence of the relatively large proportional gains selected to leverage the high positional accuracy of the motor encoders. However, in future work, the effect of improved velocity-state tracking should be investigated since velocity-state accuracy is known to correspond well with force-tracking performance in admittance control. Additionally, inertia compensation might improve overall performance since the velocity-state tracking degrades with increased frequency.

Comparing the tracking performance of the individual joints, J_1 exhibits the highest overall position-tracking error (Figure 30), but the magnitude ratio and phase lag are in line with the other joints. The elevated position-state error likely reflects the base joint's relatively high gravity and inertial load. Increasing the proportional gain or the gravity compensation for J_1 could improve its positional accuracy; however, the control torque for J_1 (Figure 32) indicates that the requested torque already exceeds the continuous torque rating frequently. Therefore, the performance of J_1 could likely be improved by the inclusion of a gravity balance mechanism, as proposed in [106,107]. Figure 28 shows that joints J_3 and J_5 exhibit a relatively high velocity-tracking error, especially when the command signal changes sign, crossing through zero velocity, where nonlinear friction effects are significant. These joints show elevated velocity-error variance over the entire frequency range (Figure 31). Interestingly, the time-series response and error (Figure 28) are remarkably consistent between repetitions of the sine-wave input. These results suggest that stiction on these joints is impacting performance. The state-tracking error appears to build up due to joints sticking at low speeds; then, when friction is broken, structural excitation occurs (Figure 28). Therefore, the performance of these joints might be further improved by supplying additional nonlinear friction compensation, or by increasing the value of their derivative gains.

Overall, the tracking performance is accurate, and state tracking exhibits reasonably low variance. While further tuning could potentially improve state-tracking performance, these results establish a benchmark of BLUE SABINO's performance and demonstrate that the proposed tuning is sufficiently performant for the development of admittance force control.

4.6. Biosignal Acquisition

Through the simultaneous collection of biosignals and robot kinematics and kinetics, we were able to obtain and visualize a number of expected patterns in the data. Figures 34 and 35 nicely illustrate the temporal relationships between measures of the experiment where shoulder interaction torque is registered first, which then drives velocity, and eventually induces displacement. The EMG activation of the shoulder is seen about 100 ms before the onset of force generation in the HMA. Table 12 shows that EMG correlates with movement speed [112], and EEG features (beta and low-beta power) correlate with the amount of shoulder interaction loading which may be similar to the previously reported relationship between EEG and force observed in fingers [113].

We were also able to observe expected power changes in the mu (μ) and low-beta (Lβ) bands from the EEG signal over the contralateral (left) sensorimotor area. Beta and μ oscillations are known to decrease with movement—a phenomenon referred to as event-related desynchronization (ERD) or power suppression. After movement stops, these oscillations remerge—a process known as event-related synchronization (ERS) [99]. For the biosignal validation experiment, the μ and Lβ power over time display the expected patterns of desynchronization and synchronization (Figures 34 and 35). These patterns coincide with kinematic features and EMG activation in shoulder muscles. Trends are observable for the periods of active movement (both in reaching and coming back to the starting location). Moreover, Lβ power topographical maps reveal a prominent decrease in power over the left hemisphere (blue in Figure 35), specifically over sensorimotor areas [100,114].

While μ and Lβ ERS responses are present, they are less prominent than expected due to the task design. The relatively short inter-trial intervals caused movement offsets and the preparation for the next movement to overlap. Therefore, longer wait periods in the task are needed to ensure enough time after movement to fully discern ERS in both frequency bands [114].

Noise was successfully mitigated using the same pipeline previously used in experiments without the robot [97]. This confirms that if the correct impedance levels are ensured during participant's setup, the EEG signal is not particularly susceptible to noise from the motors and other hardware of the exoskeleton.

Muscle group activation, derived from EMG, was consistent across all the repetitions of the experiment. These activations also highlight the muscles used for each of the gestures in our task. The deltoid and trapezius muscles were primarily used in the outward-reaching motion, while the deltoid and pectoralis major were most active in coming back to the home position. This is seen in Figure 34, where muscle group activations coincide with kinematic patterns. From the plot, a reduction of pectoralis major activation below baseline is also seen during the outward movement, highlighting its lack of involvement in producing the movement but also the importance of its activity suppression to avoid hindering the movement generated by its antagonist muscle, the trapezius.

Another meaningful result can be seen in EMG activation remaining high while the human–robot interaction torque falls, indicating high force transparency during movement while the user primarily supports his or her own weight and inertia. High force transparency, also called low impedance, is one of the most difficult modes to achieve in exoskeletons and is also one of the most important factors in allowing individuals to move freely and unrestricted. This mode is the basis from which all other control modes of the exoskeleton are built (e.g., assistive, resistive, and others).

The results of our biosignal experiment confirm our system's ability to simultaneously and synchronously record and quantify multi-domain information related to movement. The results show the validity of the features, as they align with the literature and prior expectations. However, it is important to replicate the tests on a larger sample size and expand to tasks with different movements using the forearms and hands in unimanual and bimanual tasks, both of which are implementable with BLUE SABINO. Here, shoulder movements were performed, as these large actuators are more likely to affect the signals, especially the EEG, with electromagnetic noise from motors and cables lying closest to the EEG sensors.

5. Conclusions

In this paper, we have introduced the design and validation of a new robotic instrument for the bilateral assessment of arm and hand function. While our initial focus in its development has been to support future investigations of the underlying sources of function and impairment after neurological injury, the resulting instrument can have utility in a wide variety of applications in multidisciplinary fields, combining engineering, neurorehabilitation, neurophysiology, neuropsychology, and computer science. At the nexus

of neurorehabilitation and neurophysiology, for example, applications may include the analysis of movement primitives and the characterization of impairment and recovery mechanisms. In the overlap between engineering and neurorehabilitation, the system provides opportunities in brain-machine interfaces and neuroprosthetics, as well as in the investigation of optimal training methods, with the ability to compare different approaches on the same device. Other applications may include virtual reality training, psychometric studies, and baselining normative human motor and sensory function. In the short term, using BLUE SABINO, we hope to investigate healthy, impaired, and enhanced human function in the arm and hand, particularly as it contributes to activities of daily living and other aspects of healthy lifestyles. Our long-term goal is to improve the understanding of underlying impairments and quantitatively investigate therapeutic approaches to the neurological recovery of function.

Author Contributions: Conceptualization, E.T.W. and J.C.P.; Data curation, C.K.B. and S.R.P.; Formal analysis, C.K.B. and S.R.P.; Funding acquisition, J.C.P.; Investigation, C.K.B., S.R.P. and R.M.; Methodology, C.K.B. and J.C.P.; Project administration, J.C.P.; Resources, E.T.W. and J.C.P.; Software, C.K.B., S.R.P. and R.M.; Supervision, E.T.W. and J.C.P.; Validation, C.K.B., S.R.P. and R.M.; Visualization, C.K.B., S.R.P. and J.C.P.; Writing—original draft, C.K.B., S.R.P., R.M. and J.C.P.; Writing—review and editing, C.K.B., S.R.P., E.T.W. and J.C.P. All authors have read and agreed to the published version of the manuscript.

Funding: This research was funded by National Science Foundation (NSF) award 1532239; Eunice Kennedy Shriver National Institute of Child Health and Human Development (NICHD) of the National Institutes of Health (NIH) award K12 HD073945; National Institutes of Health (NIH) award P41 EB018783, the Dean and Cindy Haagenson Endowed Professorship in Mechanical Engineering, the University of Idaho, and the Stratton Veterans Affairs Medical Center.

Data Availability Statement: Data are contained within the article.

Acknowledgments: The authors would like to thank Harmonic Drive LLC for providing educational discounts on actuation components and for their technical support during system integration. The authors also want to thank Jacob Rosen for his contributions to early solid models for the arm, and for leading the development of the OTHER hand with Peter Ferguson, Jianwei Sun, and Ji Ma at the UCLA Bionics Lab.

Conflicts of Interest: The authors declare no conflicts of interest. The funders had no role in the design of the study; in the collection, analyses, or interpretation of data; in the writing of the manuscript; or in the decision to publish the results.

Appendix A. Parallel Mechanism Design for Axial Rotation about the Arm

The parallel mechanisms of the upper and lower arm are similar to a classical four-bar (Figure A1A), except that both input and output links each have a third joint that forms a triangle with the first two joints, such that the additional joints can be attached to a fifth link in parallel with the intermediate link (Figure A1B). Both the intermediate and fifth link are then extended beyond the connection to the output link to allow a sixth link to be driven in the same way as the output link, but at a further distance from the input without needing a bearing at its center (Figure A1C). In this way, a 180-degree rotation of a motor, located beside the arm, can induce an equivalent rotation about a remote center (RC) aligned with the long axis of the arm (Figure A2A).

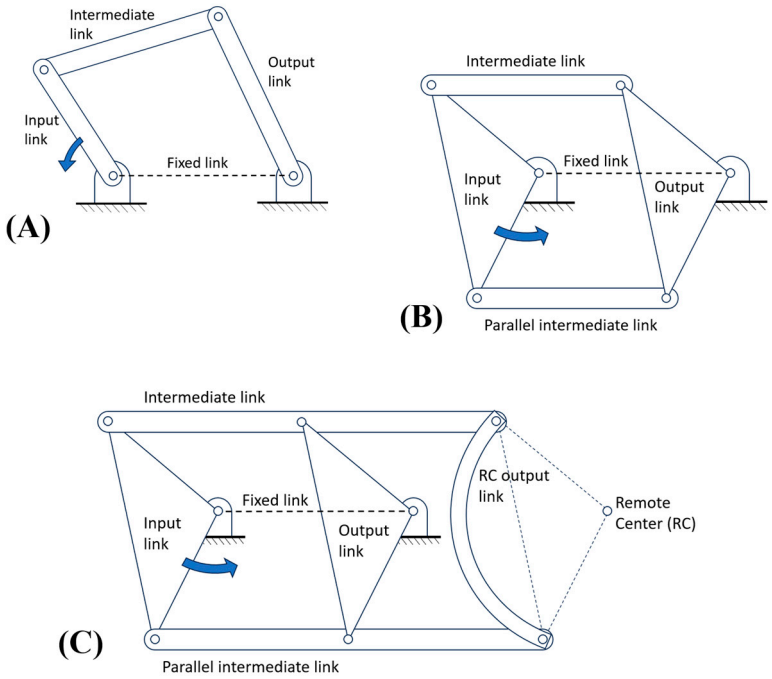

Figure A1. A triple-pivot four-par mechanism is similar to a standard four-bar mechanism (**A**), with two intermediate links operated in parallel (**B**), and with both intermediate links extended beyond the output link pivot to a remote center (RC) output link (**C**).

Variations of this mechanism have been used in two previous exoskeletons—one for the internal–external rotation of the shoulder [71] and the other for the pronosupination of the forearm [17]. Although novel in its application to exoskeletons, the same mechanism was used decades earlier to apply full-round edges to the cutting surfaces of grinding wheels ([70], pg. 93). In the Limpact design [71], the long and slender linkages' geometry produced an overly flexible assembly. In the BLUE SABINO design, the stiffness of the assembly has been significantly increased. The link cross-sectional dimensions are widened and machined with hollow cavities to improve strength-to-weight ratios further. Deep-groove ball bearings are used to keep friction low while allowing moderate support against both axial and radial loading.

All ball bearings have some degree of axial and radial play (i.e., looseness between balls and bearing raceways). In a serial chain, the combined play of many bearings can result in significant end-effector displacement, limiting control accuracy and bandwidth. For these reasons, a dual preloaded bearing shoulder-bolt design was used to minimize play (Figure A2B).

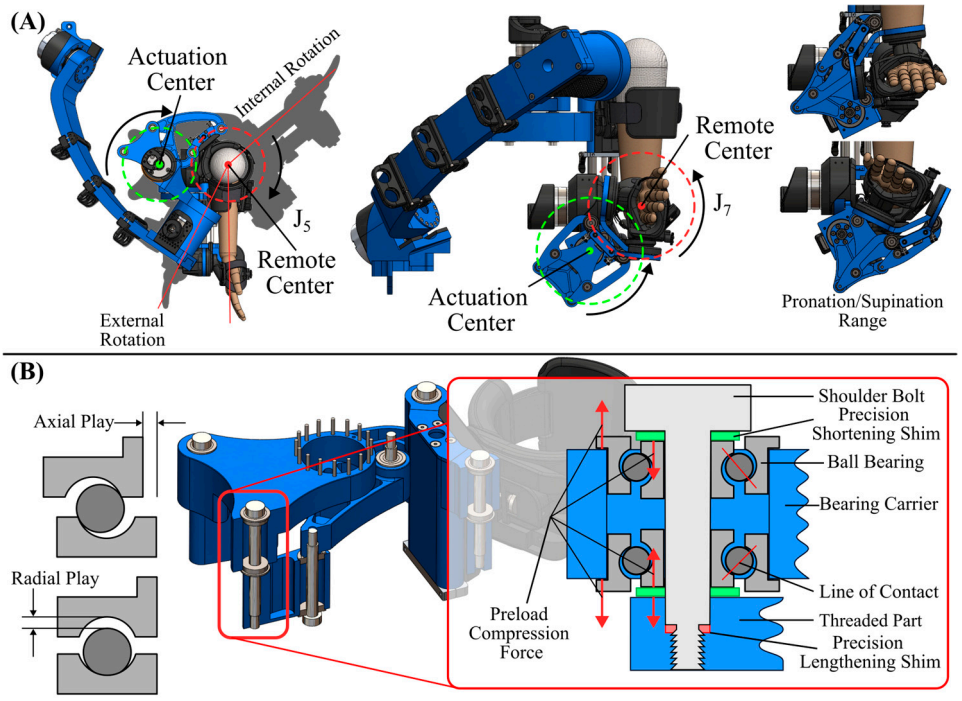

Figure A2. Remote-center mechanisms. (**A**) Remote-center mechanisms at the upper arm and forearm allow the placement of actuators for internal/external rotation and pronation/supination away from the anatomical centers of rotation. (**B**) The mechanisms use ball bearing pairs that are spaced apart to reduce angular play resulting from each bearing experiencing radial play in opposite directions. Precision shims ensure a snug fit at each bearing interface. The shims and compression preload applied by the precision shoulder bolts reduce both axial and radial play.

Appendix B. Friction Modeling and Compensation of Harmonic Drive Motors

Using Copley Control's CME2 driver control software, the XE2 motor drivers were set to velocity-control mode. A minimum threshold torque value to overcome Coulomb and viscous friction was established for each motor as the minimum positive constant velocity command that produces consistently low acceleration. This value indicated the minimum torque needed to compensate for drive inertia.

To capture the complete relationship between friction torque and drive velocity, a range of velocity commands between −4 and 4 rad/s was applied to each actuator for ~30 s each. Velocities in this range were sampled strategically to achieve enough density of samples in the low-speed range to capture Stribeck effects. The resulting measured velocity and applied torques were recorded for each velocity. The steady-state torque required to maintain constant velocity was estimated as the average recorded torque at each sample velocity. These mean torque values are plotted against command velocity to create friction–torque/–velocity maps (Figure A3).

Several mathematical models have been fit to the friction–velocity maps using MATLAB's FMINCON optimization function [77]. The cost function used was

$$C = \sum_{i=1}^{N} |\tau_{meas} - \hat{\tau}_f|, \tag{A1}$$

where N is the number of sampled velocities, τ_{meas} is the average control torque measured from the motor driver and $\hat{\tau}_f$ is the estimated torque computed from the mathematical model. The mathematical model best describing the friction of the motors is

$$\hat{\tau}_f = c_1 \left(\frac{1}{1 + e^{-c_2 \dot{\theta}}} - 0.5 \right) + c_3 \left(\frac{1}{1 + e^{-c_4 \dot{\theta}}} - 0.5 \right) \tag{A2}$$

where c_i are the coefficients, $i = [1, \cdots, 4]$, found via optimization, and $\dot{\theta}$ is the motor's velocity. The coefficients fit using FMINCON are presented in Table A1. Coefficients c_1 and c_2 control the amplitude and slope of a slow-velocity component, respectively, whereas coefficients c_3 and c_4 determine the amplitude and slope of the high-velocity component. In other words, the first two coefficients capture Coulomb friction effects while the second two model viscous friction. While this model does not capture the impact of Stribeck friction, this is considered an acceptable tradeoff since Stribeck effects are observed to be low magnitude and the sigmoid functions offer advantageous properties, namely they are smooth, continuously differentiable, bounded, and monotonically increasing.

When the optimized fit parameters from FMINCON were applied to compensate for friction in control, high-frequency vibration at a low motion speed occurred. This effect is particularly noticeable if the gain on friction compensation approaches one (i.e., total model compensation). Notably, the steep slope of the coulombic friction term, c_2, was determined to be the progenitor of this issue. At low speeds, noise in the velocity signals measured by encoders is multiplied by relatively high friction compensation values, and chatter, i.e., feedback amplification of encoder noise, can occur. While setting a lower gain on the entire friction model (~0.4–0.6) does prevent chatter, it also has the unfortunate effect of reducing viscous friction compensation. We resolve this issue by using a modified set of coefficients with c_2 intentionally reduced to improve noise rejection. These relaxed parameters (also recoded in Table A1) enhanced overall performance at the cost of some loss of Coulombic compensation. They successfully reduce Coulombic chatter without the reduction of viscous compensation (Figure A4).

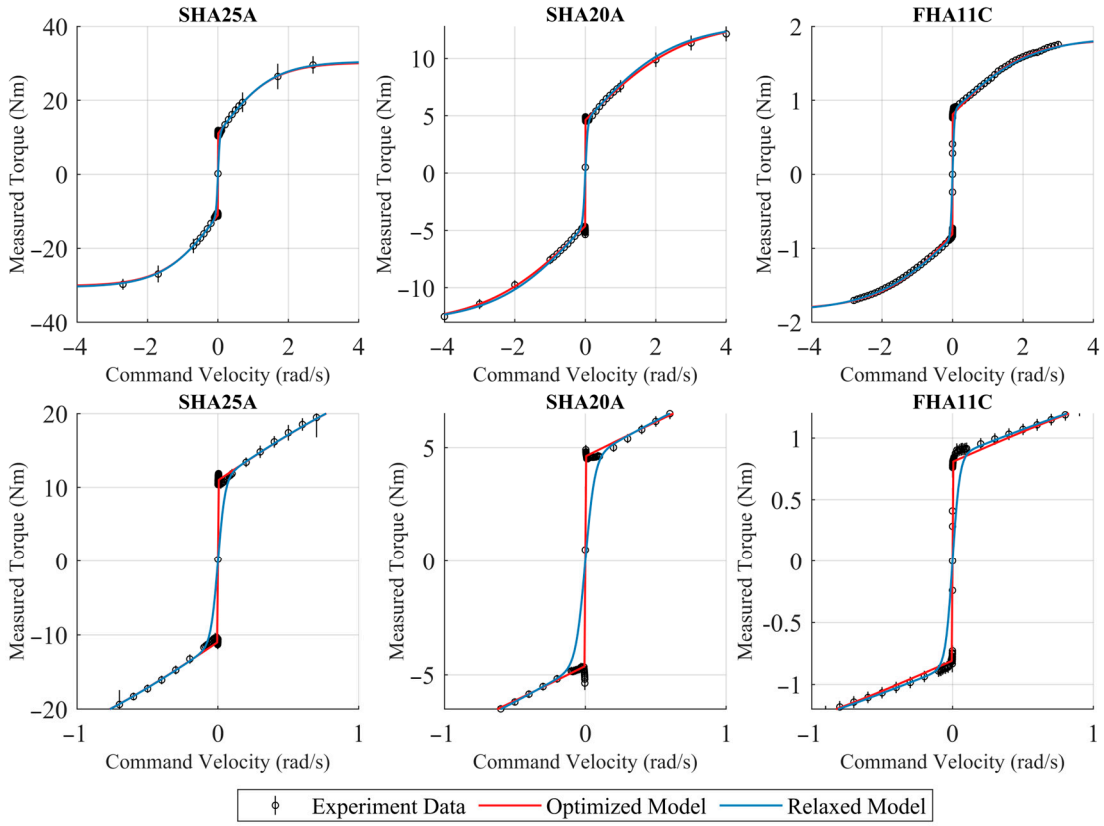

Figure A3. Experimental mean and standard deviation measurements vs. optimal-fit and relaxed-Coulombic-fit models show the torque required to overcome friction in each system motor. The sigmoid model of Equation (18) with parameters fit using FMINCON optimization best fits the experimentally measured torque–velocity profiles. However, the relaxed model reduces activation in the low-velocity region, improving chatter rejection.

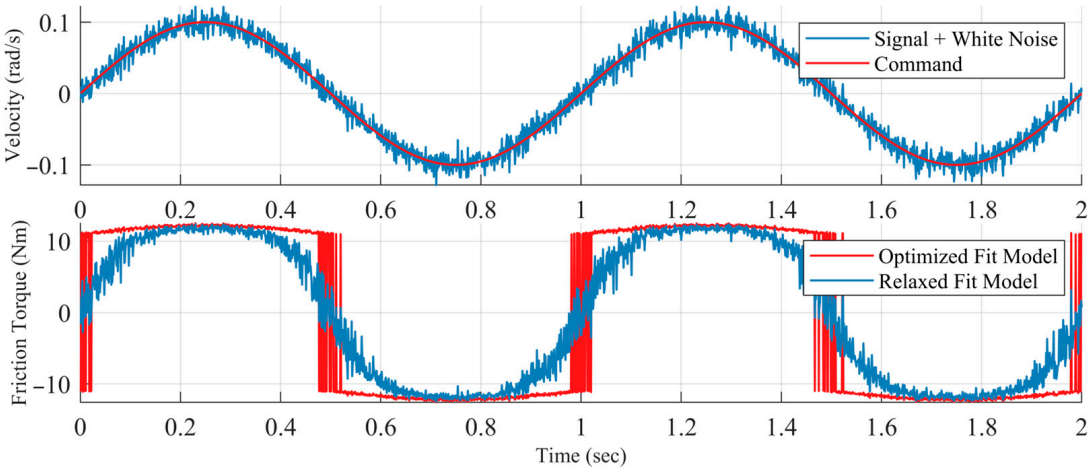

Figure A4. The effect of the friction model using relaxed-fit vs. optimal-fit friction parameters is illustrated. Friction torque compensation for a white noise-corrupted 1 Hz velocity signal is computed using the proposed sigmoid friction model with both sets of parameters. The relaxed-fit model effectively reduces the effect of discontinuous chatter as velocity passes through 0.

Table A1. The coefficient values used with Equation (18) to estimate friction-based torque for each motor type are listed.

Motor	FMINCON Best Fit				Relaxed Coulombic Friction			
	c_1 (Nm)	c_2 (s/rad)	c_3 (Nm)	c_4 (s/rad)	c_1 (Nm)	c_2 (s/rad)	c_3 (Nm)	c_4 (s/rad)
SHA25-81	21.92	75,646.25	38.53	1.32	22	40	39	1.3
SHA20-51	9.23	1924.76	17.24	0.71	9	30	17	0.8
FHA11-50	1.63	4450.5	2.05	0.95	1.6	40	2	0.9

Appendix C. Biosignal Acquisition Signal Quality Factors

Several factors are known to affect the quality of measured biosignals, such as high impedance between the electrode–skin interface, proximity to electromagnetic noise-emitting devices (e.g., motors, power cords, lighting), movement artifacts introduced with the motion of the biosignal acquisition electrodes or cables, and unwanted crosstalk. While these can affect signals in both EEG and EMG measurement, EEG is particularly susceptible to noise as the signal size is about three orders of magnitude smaller than that of EMG.

Electrode–Skin Impedance—The quality of biosignals is enhanced by maintaining a low contact impedance at the interface between the electrode and skin, usually facilitated by applying a conductive gel between the two. Other aspects of interface preparation for EEG may include ensuring the hair and scalp are recently washed, the absence of hair products, parting the hair to facilitate more direct contact with the scalp, and the proper sizing of the cap to ensure even pressure against the electrodes. For EMG, interface preparation to lower impedance includes roughening the skin with a high-grit sandpaper, oil removal with alcohol wipes, and properly drying the skin prior to the application of electrode adhesives.

Environmental Noise—Nearby sources of electromagnetic noise, such as 60 Hz noise from line power and lighting, can be picked up by sensitive biosignal equipment. This makes the selection and preparation of the environment an important consideration. Although some noise is picked up directly at the sensor, additional noise is gathered along the length of the cable on the way to the amplifier. Active electrodes that convert analog biosignals to digital prior to transmission to the amplifier are better able to protect the raw signal from additional noise, such as motor windings and electrical power.

Movement Artifacts—Unwanted artifacts can occur in both EEG and EMG. The movement of an electrode changes the population of signals that lie within the electrode's area of focus. The movement of cables changes the electromagnetic field in which the cables reside and can impart forces on the electrode that affect the electrode–skin interface pressure, which in turn affects impedance. Movement artifacts can be mitigated through low-impedance interfaces, the use of active electrodes, shielded cables, and proper sensor and cable securement, as well as by following simple, repeatable tasks that minimize variation between repeated measures. The removal of remaining artifacts can be achieved by pre-processing strategies such as independent component analyses (ICA).

Crosstalk and Volume Conduction—All surface electrodes are akin to a microphone listening to sounds from within a conical volume below the skin. As a result, each electrode will pick up activity from multiple sources (e.g., neighboring EEG, eye blinks, jaw muscle contractions); this is known as "crosstalk" in EMG and "volume conduction" in EEG. However, by measuring with a sufficiently large array of redundant sensors, applying ICA, and knowing each electrode's relative location in the array, some of the independent signals can be reconstructed from the overall dataset.

References

1. Cirstea, M.C.; Ptito, A.; Levin, M.F. Arm reaching improvements with short-term practice depend on the severity of the motor deficit in stroke. *Exp. Brain Res.* **2003**, *152*, 476–488. [CrossRef] [PubMed]
2. Dewald, J.P.; Pope, P.S.; Given, J.D.; Buchanan, T.S.; Rymer, W.Z. Abnormal muscle coactivation patterns during isometric torque generation at the elbow and shoulder in hemiparetic subjects. *Brain* **1995**, *118*, 495–510. [CrossRef] [PubMed]
3. Beer, R.F.; Ellis, M.D.; Holubar, B.G.; Dewald, J. Impact of gravity loading on post-stroke reaching and its relationship to weakness. *Muscle Nerve* **2007**, *36*, 242–250. [CrossRef] [PubMed]
4. Lum, P.S.; Burgar, C.G.; Shor, P.C.; Majmundar, M.; Van der Loos, M. Robot-assisted movement training compared with conventional therapy techniques for the rehabilitation of upper-limb motor function after stroke. *Arch. Phys. Med. Rehabil.* **2002**, *83*, 952–959. [CrossRef]
5. Reinkensmeyer, D.J.; Kahn, L.E.; Averbuch, M.; McKenna-Cole, A.; Schmit, B.D.; Rymer, W.Z. Understanding and treating arm movement impairment after chronic brain injury: Progress with the ARM guide. *J. Rehabil. Res. Dev.* **2000**, *37*, 653–662.
6. Sommerfeld, D.K.; Eek, E.U.B.; Svensson, A.K.; Holmqvist, L.W.; von Arbin, M.H. Spasticity after stroke its occurrence and association with motor impairments and activity Limitations. *Stroke* **2004**, *35*, 134–139. [CrossRef]
7. Gowland, C.; Basmajian, J.V.; Plews, N.; Burcea, I. Agonist and antagonist activity during voluntary upper-limb movement in patients with stroke. *Phys. Ther.* **1992**, *72*, 624–633. [CrossRef]
8. Maura, R.M.; Rueda Parra, S.; Stevens, R.E.; Weeks, D.L.; Wolbrecht, E.T.; Perry, J.C. Literature review of stroke assessment for upper-extremity physical function via EEG, EMG, kinematic, and kinetic measurements and their reliability. *J. NeuroEng. Rehabil.* **2023**, *20*, 21. [CrossRef]
9. Sullivan, K.J.; Tilson, J.K.; Cen, S.Y.; Rose, D.K.; Hershberg, J.; Correa, A.; Gallichio, J.; McLeod, M.; Moore, C.; Wu, S.S.; et al. Fugl-Meyer assessment of sensorimotor function after stroke: Standardized training procedure for clinical practice and clinical trials. *Stroke* **2011**, *42*, 427–432. [CrossRef]
10. Molteni, F.; Gasperini, G.; Cannaviello, G.; Guanziroli, E. Exoskeleton and end-effector robots for upper and lower limbs rehabilitation: Narrative review. *PMR* **2018**, *10*, S174–S188. [CrossRef]
11. Nef, T.; Guidali, M.; Klamroth-Marganska, V.; Riener, R. ARMin-exoskeleton robot for stroke rehabilitation. In *World Congress on Medical Physics and Biomedical Engineering, 7–12 September 2009, Munich, Germany: Vol. 25/9 Neuroengineering, Neural Systems, Rehabilitation and Prosthetics*; Springer: Berlin/Heidelberg, Germany, 2009; pp. 127–130.
12. Lee, S.H.; Park, G.; Cho, D.Y.; Kim, H.Y.; Lee, J.-Y.; Kim, S.; Park, S.-B.; Shin, J.-H. Comparisons between end-effector and exoskeleton rehabilitation robots regarding upper extremity function among chronic stroke patients with moderate-to-severe upper limb impairment. *Sci. Rep.* **2020**, *10*, 1806. [CrossRef] [PubMed]
13. Moggio, L.; de Sire, A.; Marotta, N.; Demeco, A.; Ammendolia, A. Exoskeleton *versus* end-effector robot-assisted therapy for finger-hand motor recovery in stroke survivors: Systematic review and meta-analysis. *Top. Stroke Rehabil.* **2022**, *29*, 539–550. [CrossRef] [PubMed]
14. Schiele, A.; Visentin, G. The ESA human arm exoskeleton for space robotics telepresence. In Proceedings of the 7th International Symposium on Artificial Intelligence, Robotics and Automation in Space, Nara, Japan, 19–23 May 2003; pp. 19–23.
15. Marcheschi, S.; Salsedo, F.; Fontana, M.; Bergamasco, M. Body Extender: Whole body exoskeleton for human power augmentation. In Proceedings of the 2011 IEEE International Conference on Robotics and Automation, Shanghai, China, 9–13 May 2011; pp. 611–616.
16. Zimmermann, Y.; Song, J.; Deguelle, C.; Läderach, J.; Zhou, L.; Hutter, M.; Riener, R.; Wolf, P. Human–Robot Attachment System for Exoskeletons: Design and Performance Analysis. *IEEE Trans. Robot.* **2023**, *39*, 3087–3105. [CrossRef]

17. Kim, B.; Deshpande, A.D. An upper-body rehabilitation exoskeleton Harmony with an anatomical shoulder mechanism: Design, modeling, control, and performance evaluation. *Int. J. Robot. Res.* **2017**, *36*, 414–435. [CrossRef]
18. Mosher, R.S. Handyman to hardiman. *SAE Trans.* **1968**, *76*, 588–597.
19. Kazerooni, H. Human-robot interaction via the transfer of power and information signals. *IEEE Trans. Syst. Man Cybern.* **1990**, *20*, 450–463. [CrossRef]
20. Khalid, S.; Alnajjar, F.; Gochoo, M.; Renawi, A.; Shimoda, S. Robotic assistive and rehabilitation devices leading to motor recovery in upper limb: A systematic review. *Disabil. Rehabil. Assist. Technol.* **2023**, *18*, 658–672. [CrossRef]
21. Jayaraman, A.; Marinov, B.; Singh, Y.; Burt, S.; Rymer, W.Z. Current evidence for use of robotic exoskeletons in rehabilitation. In *Wearable Robotics*; Academic Press: Cambridge, MA, USA, 2020; pp. 301–310.
22. Lee, B.O.; Saragih, I.D.; Batubara, S.O. Robotic arm use for upper limb rehabilitation after stroke: A systematic review and meta-analysis. *Kaohsiung J. Med. Sci.* **2023**, *39*, 435–445. [CrossRef]
23. Carnevale, A.; Longo, U.G.; Schena, E.; Massaroni, C.; Presti, D.L.; Berton, A.; Candela, V.; Denaro, V. Wearable systems for shoulder kinematics assessment: A systematic review. *BMC Musculoskelet. Disord.* **2019**, *20*, 546. [CrossRef]
24. Huamanchahua, D.; Castañeda-Vásquez, C.; Vásquez-Espinoza, A.; Muñoz-Zevallos, A. Robotic Devices Types Exoskeletons for Elbow Rehabilitation: A Technological Review. In Proceedings of the 2021 IEEE 12th Annual Ubiquitous Computing, Electronics & Mobile Communication Conference (UEMCON), New York, NY, USA, 1–4 December 2021; pp. 791–796.
25. Hussain, S.; Jamwal, P.K.; Van Vliet, P.; Ghayesh, M.H. State-of-the-art robotic devices for wrist rehabilitation: Design and control aspects. *IEEE Trans. Hum. Mach. Syst.* **2020**, *50*, 361–372. [CrossRef]
26. Du Plessis, T.; Djouani, K.; Oosthuizen, C. A review of active hand exoskeletons for rehabilitation and assistance. *Robotics* **2021**, *10*, 40. [CrossRef]
27. Tran, P.; Jeong, S.; Herrin, K.R.; Desai, J.P. Hand exoskeleton systems, clinical rehabilitation practices, and future prospects. *IEEE Trans. Med. Robot. Bionics* **2021**, *3*, 606–622. [CrossRef]
28. Gull, M.A.; Bai, S.; Bak, T. A review on design of upper limb exoskeletons. *Robotics* **2020**, *9*, 16. [CrossRef]
29. Islam, M.R.; Brahmi, B.; Ahmed, T.; Assad-Uz-Zaman, M.; Rahman, M.H. Exoskeletons in upper limb rehabilitation: A review to find key challenges to improve functionality. In *Control Theory in Biomedical Engineering*; Academic Press: Cambridge, MA, USA, 2020; pp. 235–265.
30. Shen, Y.; Ferguson, P.W.; Rosen, J. Upper limb exoskeleton systems—Overview. In *Wearable Robotics*; Academic Press: Cambridge, MA, USA, 2020; pp. 1–22.
31. Cornejo, J.; Huamanchahua, D.; Huaman-Vizconde, S.; Terrazas-Rodas, D.; Sierra-Huertas, J.; Janampa-Espinoza, A.; Gonzales, J.; Cardona, M. Mechatronic exoskeleton systems for supporting the biomechanics of shoulder-elbow-wrist: An innovative review. In Proceedings of the 2021 IEEE International IOT, Electronics and Mechatronics Conference (IEMTRONICS), Toronto, ON, Canada, 21–24 April 2021; pp. 1–9.
32. Gupta, A.; Singh, A.; Verma, V.; Mondal, A.K.; Gupta, M.K. Developments and clinical evaluations of robotic exoskeleton technology for human upper-limb rehabilitation. *Adv. Robot.* **2020**, *34*, 1023–1040. [CrossRef]
33. Qassim, H.M.; Wan Hasan, W.Z. A review on upper limb rehabilitation robots. *Appl. Sci.* **2020**, *10*, 6976. [CrossRef]
34. Narayan, J.; Kalita, B.; Dwivedy, S.K. Development of robot-based upper limb devices for rehabilitation purposes: A systematic review. *Augment. Hum. Res.* **2021**, *6*, 4. [CrossRef]
35. Barbosa, I.M.; Alves, P.R.; Silveira, Z.D.C. Upper limbs' assistive devices for stroke rehabilitation: A systematic review on design engineering solutions. *J. Braz. Soc. Mech. Sci. Eng.* **2021**, *43*, 236. [CrossRef]
36. Noronha, B.; Accoto, D. Exoskeletal devices for hand assistance and rehabilitation: A comprehensive analysis of state-of-the-art technologies. *IEEE Trans. Med. Robot. Bionics* **2021**, *3*, 525–538. [CrossRef]
37. Sirawattanakul, S.; Sanngoen, W. Review of upper limb exoskeleton for rehabilitation assistive application. *Int. J. Mech. Eng. Robot. Res.* **2020**, *9*, 752–758. [CrossRef]
38. Bao, G.; Pan, L.; Fang, H.; Wu, X.; Yu, H.; Cai, S.; Yu, B.; Wan, Y. Academic review and perspectives on robotic exoskeletons. *IEEE Trans. Neural Syst. Rehabil. Eng.* **2019**, *27*, 2294–2304. [CrossRef]
39. Nam, H.S.; Seo, H.G.; Leigh, J.H.; Kim, Y.J.; Kim, S.; Bang, M.S. External robotic arm vs. upper limb exoskeleton: What do potential users need? *Appl. Sci.* **2019**, *9*, 2471. [CrossRef]
40. Bhujel, S.; Hasan, S.K. A comparative study of end-effector and exoskeleton type rehabilitation robots in human upper extremity rehabilitation. *Hum. Intell. Syst. Integr.* **2023**, *5*, 11–42. [CrossRef]
41. Bauer, G.; Pan, Y.J. Review of control methods for upper limb telerehabilitation with robotic exoskeletons. *IEEE Access* **2020**, *8*, 203382–203397. [CrossRef]
42. Nguiadem, C.; Raison, M.; Achiche, S. Motion planning of upper-limb exoskeleton robots: A review. *Appl. Sci.* **2020**, *10*, 7626. [CrossRef]
43. Nazari, F.; Mohajer, N.; Nahavandi, D.; Khosravi, A.; Nahavandi, S. Applied Exoskeleton Technology: A Comprehensive Review of Physical and Cognitive Human–Robot Interaction. *IEEE Trans. Cogn. Dev. Syst.* **2023**, *15*, 1102–1122. [CrossRef]
44. Mohebbi, A. Human-robot interaction in rehabilitation and assistance: A review. *Curr. Robot. Rep.* **2020**, *1*, 131–144. [CrossRef]
45. Massardi, S.; Rodriguez-Cianca, D.; Pinto-Fernandez, D.; Moreno, J.C.; Lancini, M.; Torricelli, D. Characterization and evaluation of human–exoskeleton interaction dynamics: A review. *Sensors* **2022**, *22*, 3993. [CrossRef]

46. Briouza, S.; Gritli, H.; Khraief, N.; Belghith, S.; Singh, D. A brief overview on machine learning in rehabilitation of the human arm via an exoskeleton robot. In Proceedings of the 2021 International Conference on Data Analytics for Business and Industry (ICDABI), Sakheer, Bahrain, 25–26 October 2021; pp. 129–134.
47. Vélez-Guerrero, M.A.; Callejas-Cuervo, M.; Mazzoleni, S. Artificial intelligence-based wearable robotic exoskeletons for upper limb rehabilitation: A review. *Sensors* **2021**, *21*, 2146. [CrossRef]
48. Shen, Y.; Ferguson, P.W.; Ma, J.; Rosen, J.; Tong, R. Upper limb wearable exoskeleton systems for rehabilitation: State of the art review and a case study of the EXO-UL8—Dual-arm exoskeleton system. In *Wearable Technology in Medicine and Health Care*; Academic Press: Cambridge, MA, USA, 2018; pp. 71–90.
49. Nef, T.; Klamroth-Marganska, V.; Keller, U.; Riener, R. Three-Dimensional Multi-Degree-of-Freedom Arm Therapy Robot (ARMin). In *Neurorehabilitation Technology*; Reinkensmeyer, D.J., Marchal-Crespo, L., Dietz, V., Eds.; Springer: Cham, Switzerland, 2022. [CrossRef]
50. Zimmermann, Y.; Sommerhalder, M.; Wolf, P.; Riener, R.; Hutter, M. ANYexo 2.0: A Fully Actuated Upper-Limb Exoskeleton for Manipulation and Joint-Oriented Training in All Stages of Rehabilitation. *IEEE Trans. Robot.* **2023**, *39*, 2131–2150. [CrossRef]
51. Rosen, J.; Perry, J.C.; Manning, N.; Burns, S.; Hannaford, B. The human arm kinematics and dynamics during daily activities-toward a 7 DOF upper limb powered exoskeleton. In Proceedings of the ICAR'05. Proceedings., 12th International Conference on Advanced Robotics, Seattle, WA, USA, 18–20 July 2005; pp. 532–539.
52. Gomez-Rodriguez, M.; Peters, J.; Hill, J.; Schölkopf, B.; Gharabaghi, A.; Grosse-Wentrup, M. Closing the sensorimotor loop: Haptic feedback facilitates decoding of motor imagery. *J. Neural Eng.* **2011**, *8*, 036005. [CrossRef]
53. Blank, A.A.; French, J.A.; Pehlivan, A.U.; O'Malley, M.K. Current trends in robot-assisted upper-limb stroke rehabilitation: Promoting patient engagement in therapy. *Curr. Phys. Med. Rehabil. Rep.* **2014**, *2*, 184–195. [CrossRef]
54. Ramos-Murguialday, A.; Broetz, D.; Rea, M.; Läer, L.; Yilmaz, Ö.; Brasil, F.L.; Liberati, G.; Curado, M.R.; Garcia-Cossio, E.; Vyziotis, A.; et al. Brain–machine interface in chronic stroke rehabilitation: A controlled study. *Ann. Neurol.* **2013**, *74*, 100–108. [CrossRef]
55. Gancet, J.; Ilzkovitz, M.; Motard, E.; Nevatia, Y.; Letier, P.; de Weerdt, D.; Cheron, G.; Hoellinger, T.; Seetharaman, K.; Petieau, M.; et al. MINDWALKER: Going one step further with assistive lower limbs exoskeleton for SCI condition subjects. In Proceedings of the B2012 4th IEEE RAS & EMBS International Conference on Biomedical Robotics and Biomechatronics (BioRob), Rome, Italy, 24–27 June 2012; pp. 1794–1800.
56. Veneman, J.F.; Kruidhof, R.; Hekman, E.E.; Ekkelenkamp, R.; Van Asseldonk, E.H.; Van Der Kooij, H. Design and evaluation of the LOPES exoskeleton robot for interactive gait rehabilitation. *IEEE Trans. Neural Syst. Rehabil. Eng.* **2007**, *15*, 379–386. [CrossRef]
57. Rohrer, B.; Fasoli, S.; Krebs, H.I.; Hughes, R.; Volpe, B.; Frontera, W.R.; Stein, J.; Hogan, N. Movement smoothness changes during stroke recovery. *J. Neurosci.* **2002**, *22*, 8297–8304. [CrossRef]
58. Krebs, H.I.; Aisen, M.L.; Volpe, B.T.; Hogan, N. Quantization of continuous arm movements in humans with brain injury. *Proc. Natl. Acad. Sci. USA* **1999**, *96*, 4645–4649. [CrossRef]
59. Perry, J.C.; Rosen, J.; Burns, S. Upper-limb powered exoskeleton design. *IEEE/ASME Trans. Mechatron.* **2007**, *12*, 408–417. [CrossRef]
60. Brunnstrom, S. Motor testing procedures in hemiplegia: Based on sequential recovery stages. *Phys. Ther.* **1966**, *46*, 357–375. [CrossRef]
61. Perry, J.C.; Maura, R.; Bitikofer, C.K.; Wolbrecht, E.T. Blue Sabino: Development of a bilateral exoskeleton instrument for comprehensive upper-extremity neuromuscular assessment. In Proceedings of the Converging Clinical and Engineering Research on Neurorehabilitation III: Proceedings of the 4th International Conference on NeuroRehabilitation (ICNR2018), Pisa, Italy, 16–20 October 2018; Springer International Publishing: Berlin/Heidelberg, Germany, 2019; pp. 493–497.
62. Perry, J.C.; Rosen, J. Isotropy of an Upper Limb Exoskeleton and the Kinematics and Dynamics of the Human Arm. *Appl. Bionics Biomech. I* **2009**, *6*, 175–191. [CrossRef]
63. Tilley, A.R. *The Measure of Man and Woman: Human Factors in Design*; John Wiley & Sons: Hoboken, NJ, USA, 2001.
64. Nasa Man-Systems Integration Standards, Volume I, Section 3 Antrhopometry and Biomechanics. Available online: https://msis.jsc.nasa.gov/sections/section03.htm (accessed on 18 August 2024).
65. Ludewig, P.M.; Phadke, V.; Braman, J.P.; Hassett, D.R.; Cieminski, C.J.; LaPrade, R.F. Motion of the shoulder complex during multiplanar humeral elevation. *J. Bone Jt. Surg. Am.* **2009**, *91*, 378–389. [CrossRef]
66. Ludewig, P.M.; Behrens, S.A.; Meyer, S.M.; Spoden, S.M.; Wilson, L.A. Three-dimensional clavicular motion during arm elevation: Reliability descriptive, data. *J. Orthop. Sports Phys. Ther.* **2004**, *34*, 140–149. [CrossRef]
67. Perry, J.C.; Bitikofer, C.K.; Hill, P.W.; Trimble, S.T.; Wolbrecht, E.T. PRISM: Development of a 2-DOF Dual-Four-Bar Exoskeleton Shoulder Mechanism to Support Elevation, Depression, Protraction, and Retraction. In *Wearable Robotics*; Academic Press: Cambridge, MA, USA, 2020; pp. 105–132.
68. Robertson, J.V.; Roche, N.; Roby-Brami, A. Influence of the side of brain damage on postural upper-limb control including the scapula in stroke patients. *Exp. Brain Res.* **2012**, *218*, 141–155. [CrossRef] [PubMed]
69. Roby-Brami, A.; Feydy, A.; Combeaud, M.; Biryukova, E.V.; Bussel, B.; Levin, M.F. Motor compensation and recovery for reaching in stroke patients. *Acta Neurol. Scand.* **2003**, *107*, 369–381. [CrossRef]
70. Sclater, N.; Chironis, N.P. *Mechanisms and Mechanical Devices Sourcebook*; Mcgraw-Hill: New York, NY, USA, 2001; Volume 3.
71. Otten, A.; Voort, C.; Stienen, A.; Aarts, R.; van Asseldonk, E.; van der Kooij, H. LIMPACT: A Hydraulically Powered Self-Aligning Upper Limb Exoskeleton. *IEEEASME Trans. Mechatron* **2015**, *20*, 2285–2298. [CrossRef]

72. Perry, J.C.; Brower, J.R.; Carne, R.H.; Bogert, M.A. 3D Scanning of the Forearm for Orthosis and HMI Applications. *Front. Robot. AI* **2021**, *8*, 576783. [CrossRef] [PubMed]
73. Murray, R.M.; Li, Z.; Sastry, S.S. *A Mathematical Introduction to Robotic Manipulation*; CRC Press: Boca Raton, FL, USA, 2017.
74. Spong, M.W. *Robot Modeling and controlRobot Modeling and Control*; John Wiley & Sons: Hoboken, NJ, USA, 2006.
75. Bitikofer, C.K. Design and Control of an Upper-Limb Exoskeleton (BLUE SABINO) for Stroke Rehabilitation and Assessment. Ph.D. Dissertation, University of Idaho, Moscow, ID, USA, 2023.
76. Stevens, R.; Maura, R.; Wolbrecht, E.; Perry, J. Scalability and Function of Lithium Thionyl Chloride Batteries for Encoders in High-Degree-of-Freedom Robotic Systems. *Bull. Am. Phys. Soc.* **2019**, *64*, 9.
77. The MathWorks Inc. *MATLAB. Version: 9.6 (R2019a)*; The MathWorks Inc.: Natick, MA, USA, 2019. Available online: https://www.mathworks.com (accessed on 1 July 2022).
78. Wolbrecht, E.T.; Chan, V.; Reinkensmeyer, D.J.; Bobrow, J.E. Optimizing Compliant, Model-Based Robotic Assistance to Promote Neurorehabilitation. *IEEE Trans. Neural Syst. Rehabil. Eng.* **2008**, *16*, 286–297. [CrossRef] [PubMed]
79. Perrusquía, A.; Yu, W.; Soria, A.; Lozano, R. Stable admittance control without inverse kinematics. *IFAC-PapersOnLine* **2017**, *50*, 15835–15840. [CrossRef]
80. Maura, R. Development of a Safe Force-Based Controller to Obtain Reliable Stroke Metrics from an Exoskeleton. Ph.D. Thesis, University of Idaho, Moscow, ID, USA, 2023.
81. Topini, A.; Sansom, W.; Secciani, N.; Bartalucci, L.; Ridolfi, A.; Allotta, B. Variable Admittance Control of a Hand Exoskeleton for Virtual Reality-Based Rehabilitation Tasks. *Front. Neurorobotics* **2022**, *15*, 789743. [CrossRef]
82. Yu, W.; Rosen, J.; Li, X. PID admittance control for an upper limb exoskeleton. In Proceedings of the 2011 American Control Conference, San Francisco, CA, USA, 29 June–1 July 2011; pp. 1124–1129. [CrossRef]
83. Bae, J.; Kim, K.; Huh, J.; Hong, D. Variable Admittance Control With Virtual Stiffness Guidance for Human–Robot Collaboration. *IEEE Access* **2020**, *8*, 117335–117346. [CrossRef]
84. Aguirre-Ollinger, G.; Nagarajan, U.; Goswami, A. An admittance shaping controller for exoskeleton assistance of the lower extremities. *Auton. Robot.* **2016**, *40*, 701–728. [CrossRef]
85. Bitikofer, C.K.; Wolbrecht, E.T.; Maura, R.M.; Perry, J.C. Comparison of Admittance Control Dynamic Models for Transparent Free-Motion Human-Robot Interaction. In Proceedings of the 2023 International Conference on Rehabilitation Robotics (ICORR), Singapore, 24–28 September 2023; pp. 1–6.
86. Keemink, A.Q.; van der Kooij, H.; Stienen, A.H. Admittance control for physical human–robot interaction. *Int. J. Robot. Res.* **2018**, *37*, 1421–1444. [CrossRef]
87. Slotine, J.-J.E.; Li, W. *Applied Nonlinear Control*; Prentice Hall: Englewood Cliffs, NJ, USA, 1991.
88. Gandhi, P.S.; Ghorbel, F.H.; Dabney, J. Modeling, identification, and compensation of friction in harmonic drives. In Proceedings of the 41st IEEE Conference on Decision and Control, Las Vegas, NV, USA, 10–13 December 2002; pp. 160–166. [CrossRef]
89. Hauschild, J.P.; Heppler, G.; McPhee, J.J. Friction Compensation of Harmonic Drive Actuators. In *Proceedings of the 6th International Conference on Dynamics and Control of Systems and Structures in Space, Liguria, Italy, 2004*; Cranfield Univ. Press: Cranfield, UK, 2004; pp. 683–692. Available online: https://uwaterloo.ca/motion-research-group/publications/friction-compensation-harmonic-drive-actuators (accessed on 20 June 2024).
90. Malik, A.S.; Amin, H.U. *Designing EEG Experiments for Studying the Brain*, 1st ed.; Academic Press: Cambridge, MA, USA, 2017.
91. Cohen, M.X. *Analyzing Neural Time Series Data: Theory and Practice*; MIT Press: Cambridge, MA, USA, 2014.
92. Buzsáki, G. *Rhythms of the Brain*; Oxford University Press: Oxford, UK, 2006. [CrossRef]
93. Cohen, M.X. *Cycles in Mind: How Brain Rhythms Control Perception and Action*; Sinc (x) Press, E-Book: Bucharest, Romania, 2015.
94. McGill Physiology Virtual Lab. EEG Signal Acquisition. Biomedical Signals Acquisition. Available online: https://www.medicine.mcgill.ca/physio/vlab/biomed_signals/eeg_n.htm (accessed on 20 June 2024).
95. Schalk, G.; Mcfarland, D.J.; Hinterberger, T.; Birbaumer, N.; Wolpaw, J.R. BCI2000: A General-Purpose Brain-Computer Interface (BCI) System. *IEEE Trans. Biomed. Eng.* **2004**, *51*, 1034–1043. [CrossRef] [PubMed]
96. Hill, N.J.; Mooney, S.W.J.; Prusky, G.T. audiomath: A neuroscientist's sound toolkit. *Heliyon Internet* **2021**, *7*, e06236. [CrossRef] [PubMed]
97. Rueda Parra, S.; Perry, J.C.; Wolbrecht, E.T.; Gupta, D. Neural correlates of bilateral proprioception and adaptation with training. *PLoS ONE* **2024**, *19*, e0299873. [CrossRef]
98. Pfurtscheller, G.; Lopes da Silva, F.H. Event-related EEG/MEG synchronization and desynchronization: Basic principles. *Clin Neurophysiol.* **1999**, *110*, 1842–1857. [CrossRef] [PubMed]
99. Kilavik, B.E.; Zaepffel, M.; Brovelli, A.; MacKay, W.A.; Riehle, A. The ups and downs of beta oscillations in sensorimotor cortex. *Exp. Neurol.* **2013**, *245*, 15–26. [CrossRef]
100. Barone, J.; Rossiter, H.E. Understanding the role of sensorimotor beta oscillations. *Front. Syst. Neurosci.* **2021**, *15*, 655886. [CrossRef]
101. Clancy, E.A.; Bouchard, S.; Rancourt, D. Estimation and application of EMG amplitude during dynamic contractions. *IEEE Eng. Med. Biol. Mag.* **2001**, *20*, 47–54. [CrossRef]
102. Ferguson, P.W.; Dimapasoc, B.; Rosen, J. Optimal Kinematic Design of the Link Lengths of a Hand Exoskeleton. In *Wearable Robotics*; Academic Press: Cambridge, MA, USA, 2020; pp. 193–206.

103. Rettig, O.; Krautwurst, B.; Maier, M.W.; Wolf, S.I. Definition of anatomical zero positions for assessing shoulder pose with 3D motion capture during bilateral abduction of the arms. *BMC Musculoskelet. Disord.* **2015**, *16*, 383. [CrossRef]
104. Hallaceli, H.; Günal, I. Normal range of scapular elevation and depression in healthy subjects. *Arch. Orthop. Trauma Surg.* **2002**, *122*, 99–101.
105. Taylor, C.L. *The Biomechanics of Control in Upper-Extremity Prostheses*; National Academy of Sciences: Washington, DC, USA, 1955.
106. Bitikofer, C.K.; Wolbrecht, E.T.; Perry, J.C. Mapping ADL Motion Capture Data to BLUE SABINO Exoskeleton Kinematics and Dynamics. In Proceedings of the 2018 40th Annual International Conference of the IEEE Engineering in Medicine and Biology Society (EMBC), Honolulu, HI, USA, 18–21 July 2018; pp. 4914–4919. [CrossRef]
107. Hill, P.W.; Wolbrecht, E.T.; Perry, J.C. Gravity Compensation of an Exoskeleton Joint Using Constant-Force Springs. In Proceedings of the 2019 IEEE 16th International Conference on Rehabilitation Robotics (ICORR), Toronto, ON, Canada, 24–28 June 2019; pp. 311–316. [CrossRef]
108. Taghirad, H.D.; Belanger, P.R. An experimental study on modeling and identification of harmonic drive systems. In Proceedings of the 35th IEEE Conference on Decision and Control, Kobe, Japan, 13 December 1996; pp. 4725–4730. [CrossRef]
109. Tuttle, T.D.; Seering, W.P. A nonlinear model of a harmonic drive gear transmission. *IEEE Trans. Robot. Autom.* **1996**, *12*, 368–374. [CrossRef]
110. Lu, Y.-S.; Lin, S.-M. Disturbance-observer-based adaptive feedforward cancellation of torque ripples in harmonic drive systems. *Electr. Eng.* **2007**, *90*, 95–106. [CrossRef]
111. Liu, J.; Sheng, Y.; Liu, H. Corticomuscular coherence and its applications: A review. *Front. Hum. Neurosci.* **2019**, *13*, 100. [CrossRef] [PubMed]
112. Suzuki, M.; Shiller, D.M.; Gribble, P.L.; Ostry, D.J. Relationship between cocontraction, movement kinematics and phasic muscle activity in single-joint arm movement. *Exp. Brain Res.* **2001**, *140*, 171–181. [CrossRef]
113. Stančák, A.; Riml, A.; Pfurtscheller, G. The effects of external load on movement-related changes of the sensorimotor EEG rhythms. *Electroencephalogr. Clin. Neurophysiol.* **1997**, *102*, 495–504. [CrossRef]
114. Pfurtscheller, G.; Neuper, C.; Pichler-Zalaudek, K.; Edlinger, G.; Lopes da Silva, F.H. Do brain oscillations of different frequencies indicate interaction between cortical areas in humans? *Neurosci. Lett.* **2000**, *286*, 66–68. [CrossRef] [PubMed]